

박 사 학 위 논 문

Doctoral Thesis

전기방사 나노섬유를 포함한  
3차원 인공지지체 개발 및  
조직재생으로의 적용

Development of Three-Dimensional Scaffolds  
containing Electrospun Nanofibers  
and their Applications to Tissue Regeneration

KAIST  
한국과학기술원

박 석 희 (朴 奭 熙 Park, Suk-Hee)

기계항공시스템학부 기계공학전공

School of Mechanical, Aerospace and Systems Engineering,  
Division of Mechanical Engineering

KAIST

2011

# 전기방사 나노섬유를 포함한 3차원 인공지지체 개발 및 조직재생으로의 적용

Development of Three-Dimensional Scaffolds  
containing Electrospun Nanofibers  
and their Applications to Tissue Regeneration

# Development of Three-Dimensional Scaffolds containing Electrospun Nanofibers and their Applications to Tissue Regeneration

Advisor: Professor **Dong-Yol Yang**

by

**Suk-Hee Park**

School of Mechanical, Aerospace and Systems Engineering,  
Division of Mechanical Engineering  
KAIST

A thesis submitted to the faculty of the KAIST in partial  
fulfillment of the requirements for the degree of Doctor of  
Philosophy in the School of Mechanical, Aerospace and  
Systems Engineering, Division of Mechanical Engineering

Daejeon, Korea

2010. 11. 24.

Approved by

---

Professor Dong-Yol Yang

# 전기방사 나노섬유를 포함한 3차원 인공지지체 개발 및 조직 재생으로의 적용

박 석 희

위 논문은 한국과학기술원 박사학위논문으로 학위논문심사위원회에서 심사 통과하였음.



2010 년 11 월 24 일

심사위원장 양 동 열 (인)

심사위원 박 태 관 (인)

심사위원 이 승 섭 (인)

심사위원 신 현 정 (인)

심사위원 박 인 규 (인)



---

**DME**  
20047213

박 석 희. Park, Suk Hee. Development of Three-Dimensional Scaffolds containing Electrospun Nanofibers and their Applications to Tissue Regeneration. 전기방사 나노섬유를 포함한 3차원 인공지지체 개발 및 조직재생으로의 적용. School of Mechanical, Aerospace and Systems Engineering, Division of Mechanical Engineering. 2011. 163 p. Advisor Prof. Yang, Dong-Yol. Text in English

## Abstract

In recent years, several studies have attempted to produce scaffolds with various structural properties using micro-fabrication techniques based on Rapid Prototyping (RP) methods. The first step in this research is the fabrication of bio-applicable three-dimensional (3D) structures to tissue engineering scaffolds. The developed process, namely direct polymer melt deposition (DPMD) process, employs a micropositioning system equipped with a pressure-activated micro syringe and heating module for extruding and depositing the polymer melts. Through this process, highly-controllable regular 3D structures can be successfully manufactured. Under various process conditions including temperature, pneumatic pressure and moving velocity of a nozzle, the controllability of the developed 3D structures was verified. The resultant scaffold can satisfy the requirements of structural properties such as macroscopic external shapes, internal architectures, porosity and pore size. For the practical and bio-functional applications to tissue engineering, surface modification with bioactive agents was performed so that the limited properties for cell adhesion due to smooth surface and hydrophobicity of the developed scaffold can be overcome.

On the other hand, some researchers have recognized the importance of nano-structured architecture in view of biological applications; thus, they have aimed to produce functionalized scaffolds that can mimic the nanofibrous structure of the natural extracellular matrix (ECM) and tried to fabricate various nano- and micro- scaled structures to enhance cell activation. Meanwhile, the current interest in the electrospinning methods has been concentrated on other forms of nanofibers, especially uniaxially oriented arrays of nanofibers, in order to expand their tissue engineering applications. For the fabrication of nanostructured scaffolds, the general

---

electrospinning method and the proposed fiber alignment technique are employed. Especially, as the inclined gap method and the repetitive transfer of nanofibers are introduced, the uniaxially aligned fiber array can be quantitatively controlled with its density. As well as the controllability, the proposed alignment technique provides favourable properties such as enhanced orientation and regular distribution.

For a synergistic advantage from the both techniques, a nano- and micro- hybrid process incorporating DPMD and electrospinning process was developed. It can be successfully applied to produce highly functionalized three-dimensional scaffolds with an open porous network, a controllable shape, and a controllable nanofiber architecture. The main advantage of this hybrid scaffold over the other scaffolds is its three-dimensional characteristics simulated as a 3D fibrous extracellular environment. These technical results were achieved by alternative layer-by-layer deposition of random or aligned nanofibers and microfibers using electrospinning and DPMD process. Specifically, the RP method was used in conjunction with the functional and controllable electrospinning process in an effort to realize a 3D fashioned ECM-like structure. To verify the validity of the developed scaffolds from the viewpoint of tissue engineering application, various types of cell lines were seeded and cultured within these scaffolds. Cell viability, morphology, and differentiation in the scaffolds were determined as a function of time. The results imply that the proposed hybrid scaffold provides more preferable 3D biomimetic structure and many potential applications for the regeneration of various tissues.

---

# CONTENTS

<b>ABSTRACT</b>	<b>i</b>
<b>CONTENTS</b>	<b>iii</b>
<b>LIST OF TABLES</b>	<b>vi</b>
<b>LIST OF FIGURES</b>	<b>vii</b>
<b>1. INTRODUCTION</b>	<b>1</b>
1.1 Overview of tissue engineering	1
1.2 Scaffold-based approaches	4
1.2.1 Conventional methods	4
1.2.2 Solid freeform fabrication methods	7
1.2.3 Electrospinning methods	10
1.3 Objective and scope of the study	16
<b>2. DIRECT POLYMER MELT DEPOSITION (DPMD) PROCESS</b>	<b>21</b>
2.1 Introductory remarks	21
2.2 Polycaprolactone (PCL) and material property	23
2.3 DPMD apparatus	25
2.3.1 Procedure of the DPMD process	25
2.3.2 Apparatus of the DPMD process	27
2.4 Scaffold fabrication by DPMD process	29
2.4.1 Relationship among process parameters	29
2.4.2 Microfiber deposition test	31
2.4.3 Design and fabrication of 3D scaffolds	35
2.5 Scaffold design and applications	37
2.5.1 3D framework for adipose tissue formation	37

---

2.5.2 3D scaffold coated with functional materials .....	41
2.5.3 Controlled membrane for surgical application .....	45

### 3. CONTROLLED ELECTROSPUN NANOFIBERS

#### FOR CONSTITUENTS OF 3D SCAFFOLD.....51

3.1 Introductory remarks .....	51
3.2 Fundamentals of electrospinning process .....	53
3.2.1 Electrospinning apparatus .....	53
3.2.2 Polymer solution parameters .....	55
3.2.3 Processing conditions .....	59
3.3 Principles of electrospinning for aligned nanofibers .....	62
3.4 Inclined gap method .....	65
3.4.1 Electrospinning setup and collector design .....	65
3.4.2 Effect of inclined gap on fiber suspension.....	67
3.5 Requirements for stable collection .....	71

### 4. CHARACTERIZATION OF ELECTROSPUN NANOFIBER AND

#### EFFECTS OF CELL GUIDANCE .....75

4.1 Introductory remarks .....	75
4.2 Characteristics of fiber array .....	77
4.2.1 Property of fiber alignment .....	77
4.2.2 Density of aligned fiber array .....	81
4.3 Effects of controlled nanofiber array on cell guidance .....	84
4.3.1 Experimental conditions .....	84
4.3.2 Fabrication of the controlled nanofiber array .....	85
4.3.3 Effects of nanofibrous scaffold on cell guidance .....	89

### 5. DUAL-SCALE HIERARCHICAL SCAFFOLDS

#### BY THERMAL FUSION PROCESS.....95

5.1 Introductory remarks .....	95
--------------------------------	----

---

5.2 Thermal fusion of microstructure with nanofibers .....	96
5.2.1 Concept of thermal fusion .....	96
5.2.2 Numerical analysis of the fusion process .....	99
5.3 3D integration by thermal fusion process.....	105
5.3.1 Experimental results of thermal fusion .....	105
5.3.2 3D integration with random and aligned nanofibers .....	106
5.3.3 Individualization of nanofiber scaffolds .....	108
 <b>6. APPLICATIONS FOR 3D TISSUE FORMATION .....</b>	<b>109</b>
6.1 Introductory remarks .....	109
6.2 3D scaffolds containing random fiber mesh .....	109
6.2.1 3D scaffold fabrications .....	109
6.2.2 Effect of nanofibrous surface modification .....	113
6.2.3 Cell proliferation in 3D scaffolds .....	117
6.3 3D scaffolds containing aligned fiber array .....	120
6.3.1 3D scaffold fabrications .....	120
6.3.2 Effect of aligned nanofiber scaffold .....	123
6.4 Multilayer assembly of cell/fiber structures .....	127
6.4.1 Layer-by-Layer for 3D tissue formation .....	127
6.4.2 Fabrication of single-layer scaffold .....	129
6.4.3 Cell seeding and layer-by-layer assembly .....	130
6.4.4 Multilayer tissue formation .....	134
 <b>7. CONCLUSIONS .....</b>	<b>139</b>
 <b>SUMMARY (in Korean) .....</b>	<b>145</b>
<b>REFERENCES .....</b>	<b>147</b>
<b>ACKNOWLEDGEMENTS (in Korean) .....</b>	<b>156</b>
<b>CURRICULUM VITAE .....</b>	<b>158</b>
<b>PUBLICATIONS .....</b>	<b>159</b>

---

---

## LIST OF TABLES

**Table 1-1.** Biocompatible polymers for tissue engineering scaffolds.

**Table 1-2.** Conventional processing techniques for tissue engineering scaffolds.

**Table 1-3.** Biodegradable polymers that are used to develop electrospun nanofibers.

**Table 1-4.** Several electrospinning setups to obtain oriented fiber arrays.

**Table 2-1.** Thermal and mechanical properties of respective synthetic biodegradable polymers.

**Table 2-2.** Specifications of the DPMD apparatus.

**Table 2-3.** Calculated shear rate and measured viscosity of PCL melts.

**Table 3-1.** Specifications of electrospinning apparatus.

**Table 3-2.** The condition of polymer concentration between uniform and beaded nanofibers.

**Table 3-3.** Electrical conductivity of solvents.

**Table 3-4.** Electrospinning conditions for the successful suspension.

**Table 5-1.** Material properties of PCL for thermal analysis.

---

## LIST OF FIGURES

**Figure 1-1.** Key components for tissue engineering scaffold.

**Figure 1-2.** Scaffold produced by conventional freeze drying method.

**Figure 1-3.** Schematics of possible RP systems for scaffold fabrication. (a) Stereolithography system using laser based processing technique and liquid photopolymer, (b) Fused deposition modeling using thin filament of thermoplastic polymer and heated nozzle, (c) 3D printing using fine powder and chemical binder, (d) selective laser sintering using laser exposure and sintering powder.

**Figure 1-4.** Extracellular matrix (ECM).

**Figure 1-5.** Schematic diagram of electrospinning process during which a drop of a polymer solution is ejected from the micro nozzle and spread onto a grounded substrate in the shape of a nanofibrous matrix.

**Figure 2-1.** Chemical structures of Poly( $\epsilon$ -caprolactone).

**Figure 2-2.** Viscosity of molten PCL as a function of shear rate, for four temperatures.

**Figure 2-3.** Schematic diagram of the DPMD process.

**Figure 2-4.** Overall configuration of DPMD apparatus; (a) stainless steel syringe with a micronozzle, (b) syringe heating device, (c) temperature controller, (d) compressed air dispenser, (e) air compressor and booster.

**Figure 2-5.** Relationship of the deposited fiber radius versus velocity of the nozzle and applied air pressure.

**Figure 2-6.** Relationship between effective sectional area and fiber radius.

**Figure 2-7.** Resultant 3D scaffold fabricated by DPMD process.

**Figure 2-8.** Other types of scaffolds with various porosity.

**Figure 2-9.** Preparation of NF/hMSC composite multicellular spheroids. (a) A schematic diagram illustrating the formation of composite spheroids (b) Stereoscopic image of as-prepared composite spheroids. (C) SEM image of the composite spheroid with overall shape. (d) High-magnification SEM images (e) Surface morphology of the composite spheroid showing nanoporous geometry.

---

**Figure 2-10.** 3D biohybrid assembly with NF/hMSC composite spheroids and microstructured-scaffold. A) Schematic illustration of DPMD process from PCL polymer. B) The architecture of the fabricated scaffold with woodpile-like microfibrinous structure (fiber diameter  $\frac{1}{4}$ 200mm, fiber spacing  $\frac{1}{4}$ 400mm). C) The differentiated composite spheroids were hexagonally packed along the ordered array of void spaces of microfibrinous scaffold and firmly anchored by cellular adhesion process. D,E) 3D hybrid construct was built by successive stacking of spheroids-embedded scaffold units to form a complete 3D cylindrical geometry.

**Figure 2-11.** (a) Illustration of DPMD procedure giving rise to a 3D woodpile-like microfibrinous scaffold. (b-e) SEM images of nanocomposite multilayer-coated scaffold with HApNPs and collagen.

**Figure 2-12.** (a) hMSCs adhesion to bare, 5 bilayers-coated, and 20 bilayerscoated scaffold. (b) Quantification of DNA amounts of hMSCs on TCPS, bare, 5 bilayer-coated, and 20 bilayer-coated scaffold during 21 days of culture in growth medium.

**Figure 2-13.** Two dimensional sheet fabricated by deposition of PCL solution.

**Figure 2-14.** Concept of post surgical anti adhesion barrier.

**Figure 2-15.** Schematic diagram for coating HA gel on the PCL membrane.

**Figure 2-16.** (a) Porous PCL membrane. (b) PCL membrane coated by hydrogel. (c) A part of anti-adhesion membrane. (d) SEM image of the surface of hydrogel coating PCL membrane dried.

**Figure 2-17.** Anti-adhesion test; (a) abdominal operation of experimental rat and insertion of the HA-filled membrane, results of in vivo tests (b) with no treatment and (c) with the anti-adhesion membrane.

**Figure 3-1.** Apparatus of electrospinning process. (a) Vertical controller (distance from needle to collector), (b) collector for nanofiber alignment, (c) typical collector (aluminum plate), (d) microsyringe pump, (e) metal needle, (f) high voltage (DC) power supply

**Figure 3-2.** Process parameters of typical electrospinning.

**Figure 3-3.** Effective voltage range for nanofiber formation; (a) bead formation at less than 9 kV, (b) fibers with beads at 9 to 16 kV, (c) fibrous mats at more than 16 kV.

**Figure 3-4.** The electrospun nanofibers at spinning distance of (a) 80 mm and (b) 160 mm.

**Figure 3-5.** A rotating cylinder collector to obtain aligned nanofibers.

**Figure 3-6.** (a) Schematic illustration of the electrospinning process using rotating disk collector.



---

Double-cone envelope of the jet is shown. (b) a flash photograph of a nanofiber that is attracted to the edge of the disk.

**Figure 3-7.** Use of parallel strips as auxiliary electrode to assist in the fiber alignment.

**Figure 3-8.** (a) Schematic illustration of the electrospinning with two parallel collector. (b) Distribution of electric field strength vectors between the needle and the collectors. (c) Electrostatic force exerted on the charged nanofiber.

**Figure 3-9.** Schematic diagram of the used electrospinning setup for the proposed inclined gap method; (a) the setup for electrospinning, and (b) the nanofiber suspended sequentially across the inclined gap.

**Figure 3-10.** Calculated equipotential lines and electric field strength vectors between the needle and the collectors; (a) symmetrical distribution of the electrostatic field in the region around the collectors with planar configuration. (b) asymmetrical distribution of the electrostatic field due to the modified configuration of the collectors.

**Figure 3-11.** Photographs of the collectors with the suspended nanofibers on (a) the planar gap, and (c) the inclined gap. Optical micrographs of parts of the nanofiber arrays on (b) the planar gap, and (d) the inclined gap.

**Figure 3-12.** SEM images of a) the randomly deposited nanofibers on the upper strip, and b) the uniaxially aligned nanofibers between the upper and lower strip edges.

**Figure 3-13.** Photographs of (a) the successful suspension and the inappropriate suspensions due to (b) the low solution concentration (10 wt%, 160 mm distance) and (c) the short spinning distance (50 mm, 18 wt% concentration).

**Figure 4-1.** SEM image for measurement of nanofiber alignment.

**Figure 4-2.** Histogram of distribution of the angle between the longitudinal axis of the each fiber and the expected direction.

**Figure 4-3.** (a,b,c,d,e) SEM images of the aligned nanofiber array electrospun during different spinning times: 10, 20, 30, 40, and 50 sec, respectively (the scale bars are all 100  $\mu\text{m}$ ). (f) Corresponding orientation parameters and values of densities.

**Figure 4-4.** SEM images of the nanofiber arrays transferred repetitively; (a) 1 transfer, (b) 3 transfers, (c) 10 transfers, and (d) 20 transfers. The scale bar on (a) is 20  $\mu\text{m}$ , and the other images are at the same magnification.

**Figure 4-5.** Comparison between results of the inclined and the planar gap collection: Photographs of the fiber arrays suspended on (a) the inclined gap collector and (b)

---

the planar gap collector. Histograms of angle distribution of fiber alignment in the arrays transferred from (c) the inclined gap collector and (d) the planar gap collector. Homogeneous fiber arrays collected from the inclined gap by (e) single transfer and (f) 3 transfers. Inhomogeneous fiber arrays collected from the planar gap by (g) single transfer and (h) 3 transfers. Arrows indicate the inhomogeneous conditions of the fiber distributions. The scale bars are 10 mm (a, b) and 100  $\mu\text{m}$  (e-h), respectively.

**Figure 4-6.** (a) Photograph of nanofibers collected on the upper strip and within the gap space. SEM images of (b) the microscale fibers deposited directly on the upper strip (The scale bar is 5  $\mu\text{m}$ ), and (c) the sub-microscale fiber uniaxially suspended within the gap space (The scale bar is 2  $\mu\text{m}$ ).

**Figure 4-7.** Phase contrast micrographs illustrating the cell alignment effect of different fiber arrays for (a) 1, (b) 3, and (c) 10 transfers. The scale bar on (a) is 100  $\mu\text{m}$ ; the other images are at the same magnification. The arrows indicate the direction of the fiber orientation.

**Figure 4-8.** Immunofluorescent staining images of cell morphologies and quantitative assessments of cell alignments on (a) bare PDMS substrate without fiber (Control), (b) fiber mesh deposited randomly (Random), (c) singly transferred substrate with aligned nanofibers (1 tr), and multiply transferred substrate with (d) 5 (5 trs) and (e) 20 transfers (20 trs). Red and blue correspond to actin and nucleus, respectively. The scale bar on (a) is 50  $\mu\text{m}$ ; the other images are at the same magnification. (f) Elongation factor ( $E_f$ ) of the each scaffold. Data shown as mean  $\pm$  standard deviation ( $n = 30$  in each scaffold, \*\*\*  $p < 0.001$ ).

**Figure 4-8.** Immunofluorescent staining images to visualize the formation of actin stress fiber on the substrate (a, b) with single transfer and (c, d) with 20 transfers. The scale bar on (a) is 30  $\mu\text{m}$ ; the other images are at the same magnification.

**Figure 5-1.** The hybrid scaffold containing microfibers and nanofiber matrices built via a combined process of DPMD and electrospinning.

**Figure 5-2.** Principle of thermally-fused assembly between micro-extrudate and nanofiber mat.

**Figure 5-3.** Schematics of thermal field during plotting a molten polymer.

**Figure 5-4.** Cross-section of the nanofiber mat transferred repeatedly up to 40 transfers.

**Figure 5-5.** Three steps of the thermal fusion procedures; (a) Microfiber in a molten state is laid on the nanofiber mat having initially the room temperature. (b) Fused region is

---

generated and penetrated into the nanofiber mat. (c) Fused assembly including microfiber and nanofiber mat is solidified as process time elapses.

**Figure 5-6.** Penetration of thermal fusion region in different process temperatures.

**Figure 5-7.** Thermally fused region at the bottom of nanofiber mats in the different process temperatures including (a) 60°C, (b) 70°C, (c) 80°C, and (d) 100°C.

**Figure 5-8.** (a) Delamination caused by the low process temperature of 60°C, (b) stable fusion at the process temperature of 100°C.

**Figure 5-9.** Transfer methods of electrospun nanofibers with (a) random and (b) aligned configurations.

**Figure 5-10.** 3D integrated scaffolds with insertion of electrospun nanofibers; (a, b) random nanofiber mat, (c, d) aligned nanofiber array.

**Figure 5-11.** Individual framed nanofiber scaffolds with aligned nanofiber array. (a,b) Closed type, (c,d) open type.

**Figure 6-1.** (a) Photograph of the overall 3D woodpile structure with dimensions of 9 mm x 9 mm x 3.5 mm, (b) the hybrid basic unit layer composed of microfibers and the electrospun nanofibers matrix, (c, d) magnified images of (b).

**Figure 6-2.** Schematic diagrams and photographs of three types of the hybrid scaffolds used in the cell culture experiments: (a) Type I has no nanofiber matrix and only a PCL scaffold as a control specimen. PCL scaffolds combined with (b) a one layer PCL/collagen nanofiber matrix (Type II) and (c) a three-layer PCL/collagen nanofiber matrices (Type III).

**Figure 6-3.** Microfiber prepared for the pre-testing experiment: (a) a photograph of microfibers with lengths of ca. 10 mm and diameters of ca. 0.4 mm, (b) a schematic diagram of three different types of microfibers, only microfiber-only, surface-modified microfibers with PCL nanofibers and the PCL/collagen blend nanofibers, (c) SEM image of a microfiber coated with the PCL/collagen nanofibers, (d) magnified image of the PCL/collagen nanofibers deposited on the surface of a microfiber.

**Figure 6-4.** Cell proliferation pretest of bovine chondrocytes on different microfibers: microfiber-only, surface-modified microfibers with PCL nanofibers and the PCL/collagen blend nanofibers.

**Figure 6-5.** Cell proliferation assessment for a 10-day culture period on three types of final

---

scaffolds.

**Figure 6-6.** SEM images of chondrocytes and scaffold interaction after three days in the culture:

(a) at the junction of two microfibers (arrows indicate attached chondrocytes) and (b) spread cell on the surface in a Type I scaffold, (c) the border of a microfiber (left) and a nanofiber matrix (right), and (d) chondrocytes layered on the nanofiber matrix in a Type III scaffold.

**Figure 6-7.** Repetitive process of DPMD and transfer of aligned nanofiber arrays and configuration of 3D scaffolds containing aligned nanofiber mats.

**Figure 6-8.** SEM image of 3D scaffold containing aligned nanofibers.

**Figure 6-9.** Preparation of various scaffolds in order to evaluate the 3D integration with aligned nanofibers.

**Figure 6-10.** Adhesion property of Human mesenchymal stem cell into the various scaffolds.  
[Cell number differential = (cell number at initial seeding – cell number after 4 hr incubation) / cell number at initial seeding]

**Figure 6-11.** Proliferation property of Human mesenchymal stem cell into the various scaffolds.

**Figure 6-12.** Immunostaining results of hMSC actin fibers.

**Figure 6-13.** A schematic illustration of the L-b-L cell assembly while electrospinning.

**Figure 6-14.** Package of the transferred nanofiber mats using DPMD process, and the resultant individual nanofiber scaffolds.

**Figure 6-15.** Schematics of cell seeding onto single-layer scaffold and layer-by-layer integration using collagen gel and polymer solution. (a) Preparation of unit scaffolds. (b) Cell seeding. (c) Assembly of cell/fiber construct using polymer solution and collagen gel. (d) Multi-layer integration.

**Figure 6-16.** Cells adhered on surface of aligned nanofiber scaffold in five hours after cell seeding.

**Figure 6-17.** Application of collagen gel to the cell/fiber scaffolds.

**Figure 6-18.** Confocal microscopic images of multilayer cell/fiber constructs of 1, 2, and 4 layer integration. Red, green, and blue are electrospun nanofiber, actin, and nucleus, respectively.

**Figure 6-19.** Light microscopic images of cross sections of multilayered cell/fiber constructs. (a) 4 layer integration of cell/fiber constructs and (b) single layer cell/fiber construct which have the same number of nanofibers as the case of (a).

**Figure 6-20.** Myotube assembly on the aligned PCL nanofiber scaffold. Immunofluorescence

---

staining of skeletal MHC was performed to show the myotubes at 7 days after the application of differentiation media.

**Figure 6-21.** Immunofluorescence staining of anti-MHC showing a striated myotube on aligned nanofiber scaffold.



---

## CHAPTER I

### INTRODUCTION

#### 1.1 Overview of tissue engineering

Tissue engineering was born of the necessity to treat the defect or loss of an organ or tissue in health care. The need to replace or repair damaged bone, cartilage, skin, muscle and even nervous tissue is deriving multi-disciplinary technologies of biology, material sciences, and engineering. Currently, practical approaches for tissue replacement largely depend on autografts, allografts, or metallic devices. Although these methods are effective for clinical applications, there are some limitations including shortage of donors, ability to maintain the organ's proper functionality, and potential immune rejection problem. In order to overcome these limitations, the strategies for creating new tissue have been focused in the tissue engineering field.

One of the effective strategies is cellular therapy that involves injection or transplantation of cells. For example, one such cell-based procedure is autologous chondrocyte transplantation (ACT) for cartilage repair that involves isolation of chondrocytes from the patient, proliferation of the cells in vitro, and transplantation of the cells back into the patient body [1, 2]. Furthermore, in the past decade, the cell therapy has advanced considerably using stem cells, which are undifferentiated cells with the capacity for unlimited or prolonged self-renewal and the ability to give rise to differentiated cells. However, if the loss of tissue is a large volume or requires a physical and mechanical support, the infusion of the cells alone would have a limitation.

As well as the cell-based therapy, the application of cell-scaffold composite also has achieved some noteworthy results in tissue regeneration strategies. Whereas cell therapy uses cells alone, the scaffold-based method employs a three or two dimensional matrix on or within which cells are cultured. The cells seeded in the scaffold can proliferate and migrate, produce extracellular matrix (ECM), and form a functional tissue with a desired shape along the scaffold geometry. The scaffold also has many advantages in that it provides structural support during tissue formation and allows incorporation with biological and mechanical factors to enhance tissue regeneration.

Therefore, many researchers have given much attention to fabricate and apply the 3D scaffolds to the tissue engineering field. According to development of various biomaterials with biodegradability and biocompatibility, the importance of 3D scaffold application has been emphasized. Although it is not yet clear what defines a so-called 'ideal scaffold', recent advancement in micro/nano fabrication technologies has played a key role in the scaffold-based approach. Typically, the scaffold fabrication should satisfy at least a set of minimum biochemical and physical requirements as follows [3] (Figure 1-1).

- Mechanical integrity to tissues by acting as a support for neo-tissue growth.
- Guidance for biological response through the promotion of the dynamic interaction with surrounding tissues.
- A space for host cell survival, enhancing the transport of nutrients and metabolites through.
- Maximization of biological and/or pharmaceutical response.
- Adequate biocompatibility/biodegradability, with degradation kinetics suitable to match neo-tissue formation, thus minimizing toxicity in terms of both tissue and systemic response.
- Manufacturing feasibility.

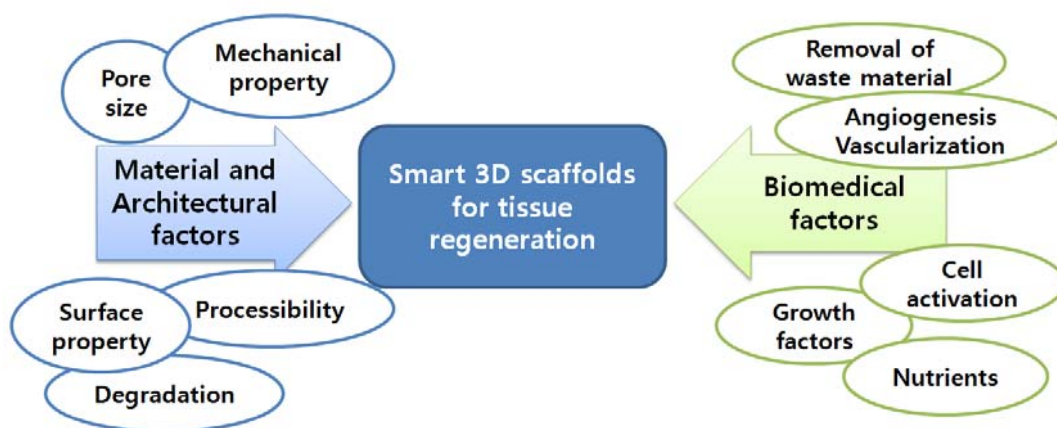


Figure 1-1. Key components for tissue engineering scaffold.

In these regards, the selection of the scaffold material is a crucial factor from the viewpoints of both the fabrication and the cell interaction. Table 1-1 lists the several options of the available polymers. The naturally-derived polymers such as collagen and hyaluronic acid hydrogel, despite of their poor mechanical property, have been useful for regeneration of soft tissues in that they do not induce a host immune response and encourage the cellular functions [4]. In order to widen their tissue engineering applications, many efforts are under way by incorporating with other synthetic materials for a mechanical support.

The synthetic organic polymers provide not only the desirable mechanical property but also biodegradability which is very advantageous for the applications such as medical sutures, drug delivery devices, scaffolds, vascular grafts and stents, artificial skin, orthopedic implants, and others. It is generally easy to be processed into porous structures as the scaffolds. The synthetic polymers can be chosen and tailored for a specific application based on their physical and chemical properties.



Material	
Natural organic materials	Collagens
	Hyaluronic acid and derivatives
Synthetic organic materials	Poly(glycolic acid) (PGA)
	Poly(lactic acid) (PLA)
	Poly(lactic-co-glycolic acid) (PLGA)
	Poly( $\epsilon$ -caprolactone) (PCL)
Inorganic materials	PEG and copolymers
	Hydroxyapatite (HAP)
	$\beta$ -tricalcium phosphate (TCP)

Table 1-1. Biocompatible polymers for tissue engineering scaffolds.

Using these biomaterials, several fabrication techniques have been tried to create the bio-activated scaffolds with 3D geometry and pore network. To date, potential fabrication methods include solid freeform fabrication methods, electrospinning, conventional methods such as solvent casting, fiber bonding, phase separation, particulate leaching and gas foaming. Recent advancements in scaffold fabrication are further discussed in this chapter.

## 1.2 Scaffold-based approaches

### 1.2.1 Conventional methods

The realization of a porous structure is regarded as a central goal of scaffold fabrication and various techniques have been developed accomplish this aim as listed in Table 1-2. Though the listed techniques have some limitations for controllability of geometry and full interconnectivity,

they are still used in various ways due to the relative ease of processing the scaffolds.

Process	Advantages	Disadvantages
Fiber bonding	Easy process High porosity High surface area to volume ratio	High processing temperature for non-amorphous polymer Limit range of polymers Lack of mechanical strength Problems with residual solvent Lack of control over micro-architecture
Phase separation	Allows incorporation of bioactive agents Highly porous structures	Lack of control over micro-architecture Problems with residual solvent Limited range of pore sizes
Solvent casting and particulate leaching	Highly porous structures Large range of pore sizes Independent control of porosity and pore size Crystallinity can be tailored	Limited membrane thickness Lack of mechanical strength Problems with residual solvent Residual porogens
Membrane lamination	Macro shape control Independent control of porosity and pore size	Lack of mechanical strength Problems with residual solvent Tedious and time-consuming Limited interconnected pores
Melt moulding	Independent control of porosity and pore size Macro shape control	High processing temperature for non-amorphous polymer Residual porogens
Polymer/ceramic fiber composite-foam	Good compressive strength Independent control of porosity and pore size	Problems with residual solvent Residual porogens
High-pressure processing	Organic solvent free Allows incorporation of bioactive agents	Nonporous external surface Closed pore structure
High-pressure processing and particulate leaching	Organic solvent free Allows incorporation of bioactive agents Highly porous structures Large range of pore sizes Independent control of porosity and pore size	Limited interconnected pores Lack of mechanical strength Residual porogens
Freeze drying	Highly porous structures High pore interconnectivity	Limited to small pore sizes
Hydrocarbon templating	No thickness limitation Independent control of porosity and pore size	Problems with residual solvent Residual porogens

Table 1-2. Conventional processing techniques for tissue engineering scaffolds [5].

Fiber bonding method is one of the earliest techniques to produce porous scaffolds with interconnected pores. The method employs two different mechanisms to attach fibers each other. One thing is firstly developed by Mikos et al [6]. After PGA fibers are immersed in a PLLA solution, the composite of PGA fibers embedded in PLLA is obtained by solvent evaporation. When the composite is heated to above the melting point of both polymers, the PLLA is molten

out and the PGA fibers is welded at the cross-points. The other method for bonding PGA fibers is atomization of PLLA solution [7]. When the PLLA solution is sprayed onto the PGA fibers, the fibers are coated with the solution and bonded each other as the solvent evaporates.

Solvent casting or particulate leaching create the porous structures by use of a water-soluble porogen such as salt particle [8]. After PLLA or PLGA polymer dissolved in chloroform or methylene chloride is cast with the porogen, the polymer/salt composite is obtained as the solvent evaporates. Then, the composite is leached in water to remove the salt particle. The resultant scaffold provides a favorable condition in that the porosity can be controlled by the size or amount of the added salt.

Gas foaming method has an advantage of solvent-free process [9]. The organic solvent used in the normal processes can be harmful to cells and tissues. The technique employs gas as a porogen. In the first step, solid discs of PGA, PLLA or PLGA is processed using compression molding. The discs are placed in a chamber and exposed to CO<sub>2</sub> gas of high pressure for several days. When the pressure is rapidly decreased down to atmospheric pressure, the highly porous structure can be obtained.

Freeze drying is based on the concepts of thermodynamic mechanism rather than use of the porogen [10]. PLGA solution is mixed with distilled water to form an emulsion. As casted and quenched by liquid nitrogen, the mixture of PLGA and water is freeze-dried. Through this method, scaffolds with high porosities (up to 95%) and small pore sizes (13-35  $\mu\text{m}$ ) can be obtained.

Although these techniques are able to form the porous foams with ease, they have several limitations from the viewpoint of controllability. The importance of pore geometry in the ability of cells to adhere, proliferate, and differentiate has been emphasized in the scaffold design and fabrication through the numerous studies. With regard to this point, the above conventional methods have the lack of precise control of scaffold specifications such as pore size, distribution,

---

interconnectivity, and overall shape of the scaffold. The irregularity of the pore network is revealed in Figure 1-2 as an example of conventional scaffold by freeze drying.

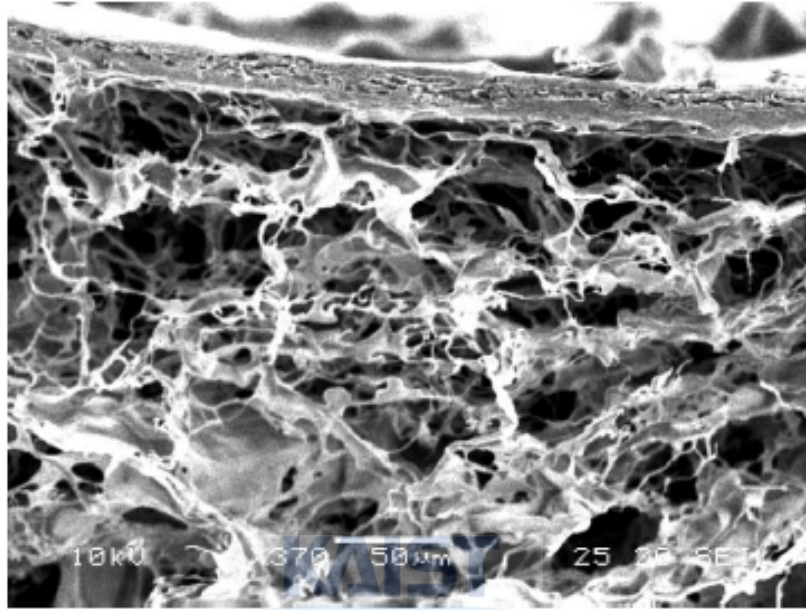


Figure 1-2. Scaffold produced by conventional freeze drying method.

### *1.2.2 Solid freeform fabrication methods*

In recent years, several studies have attempted to produce 3D scaffolds with controllable structural properties based on rapid prototyping (RP) methods or solid freeform fabrication (SFF) methods. RP techniques are a set of fabrication processes that can produce the predefined and precisely controlled constructs in accordance with computer-aided design (CAD) modeling data. As factors influencing the procedures of scaffold-based tissue engineering are very complex and not yet defined in every specific case, RP methods that can provide arbitrary and complex fabrication are regarded as advantageous and effective process for the scaffold fabrication. Basic considerations for 3D scaffold fabrication include pore size, total porosity, pore interconnectivity,

mechanical and surface properties. These are relevant to the critical factors of the scaffold-based approach, such as effective nutrient and oxygen supply, metabolic waste removal, and cellular signaling [11, 12].

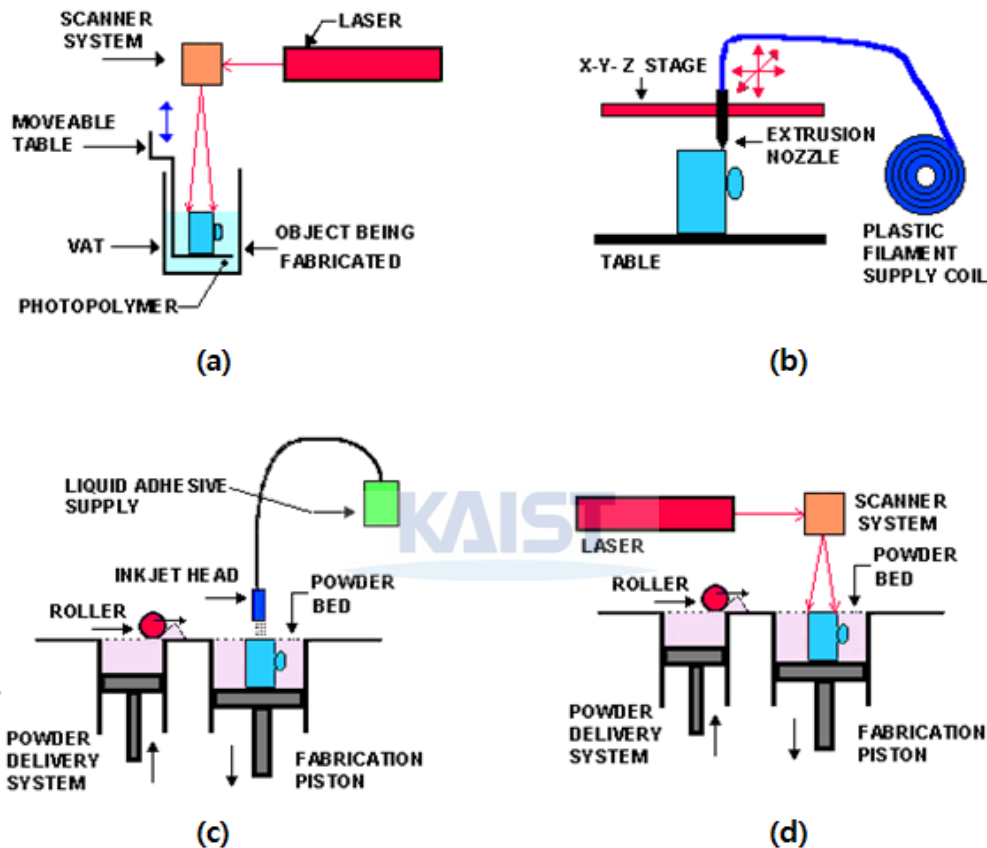


Figure 1-3. Schematics of possible RP systems for scaffold fabrication. (a) Stereolithography system using laser based processing technique and liquid photopolymer, (b) Fused deposition modeling using thin filament of thermoplastic polymer and heated nozzle, (c) 3D printing using fine powder and chemical binder, (d) selective laser sintering using laser exposure and sintering powder [13].

Recent works with scaffolds produced by RP methods can fulfill the basic requirements for

---

3D scaffold applications, while the conventional methods have the uncontrollable variation in the pore size and geometry. Furthermore, the RP techniques allow the reproducible manufacturing of scaffolds along a computer-aided design (CAD) data. The feature of the CAD-based fabrication opens up the possibility for patient-tailored scaffolds based on computer tomography (CT) or magnetic resonance imaging (MRI) data [14, 15]. The RP systems for the scaffold fabrication are categorized by the processing technique as illustrated in Figure 1-3.

Stereolithography (SLA) provides a precise 3D object via light-mediated curing process of liquid photopolymer. Since the apparatus was commercialized by 3D Systems Inc. ([www.3dsystems.com](http://www.3dsystems.com)) in 1988, the process has been recently applied to the tissue engineering field. When the surface of liquid photocurable polymer is exposed to the UV laser with its beam path based on CAD data, the polymerization is initiated along the beam path. As this laser polymerization process is repeated by raising or lowering the object platform, the 3D object can be created in a layer-by-layer manner. The resolution of a typical SLA is dependent on the resolution of the unit layer thickness (up to 1.3  $\mu\text{m}$ ) and laser spot size (80-250  $\mu\text{m}$ ) [16]. For tissue engineering applications, biocompatible photopolymers was developed such as poly(propylene fumarate) [17, 18] and acrylated poly(ethylene glycol) [19, 20], and used as the scaffold materials of stereolithography. Based on recent advances in the precision of the process, micro stereolithography ( $\mu\text{SL}$ ) with micrometer resolution has provided the improved potential for the fabrication of 3D scaffolds [21, 22].

Fused deposition modeling (FDM) process uses the pre-formed polymer filaments and the heated nozzle attached to a moving table in the horizontal stage. While extruded through the nozzle, the liquefied polymer is deposited as a layer shaped along the nozzle movement. Then, the stage is lowered and the following layer is newly deposited. As the lamination process is repeated, the 3D structure can be fabricated. When this method is applied to the scaffold fabrication, the perfectly non-toxic scaffold without the organic solvent can be obtained. The

process has been used to produce the scaffold from various thermoplastic polymers and their composites such as PCL, PEG-PCL-PLA, and PCL/hydroxylapatite (HA) composite [23-25]. Moreover, this extrusion-based process can be applied to different methods by changing its material and extruding mechanism. One such technique, 3D bioplotting, involves the reactive processing of aliphatic polyurethanes based on lysine ethyl ester diisocyanate and isophorone diisocyanate [26].

3D printing (3DP) is a process whereby PLA powders is bonded together using ink-jet printer to spray the surface of powder bed with a binder [27]. The printing process is repeated on top of the previous layer, and 3D object can be obtained. In the typical process, the organic solvents used as binders can be replaced by biocompatible materials. As an example, hydroxyapatite (HA) powder was used to fabricate bone scaffolds employing a binder composed of polyacrylic acid dissolved in a water-glycerol mixture [28].

Similar to 3D printing, selective laser sintering (SLS) also uses powders, which is sintered together by a laser beam along the beam path. As the powder materials, some biodegradable polymers have been used to fabricate scaffolds such as polyetheretherketone, poly (vinyl alcohol), polycaprolactone, and poly (L-Lactic acid) [29-31].

In summary, the recent works with scaffolds fabricated using SFF techniques have provided the controllable scaffold geometry eliminating the variability of structural features such as the pore size and interconnectivity. These techniques are expected as promising technologies for fabrication of the patient-specific and clinically practical scaffolds.

### *1.2.3 Electrospinning methods*

Some researchers have recognized the importance of nanostructured architecture in view of biological applications. Thus, they have aimed to produce functionalized scaffolds that can mimic

---

the nanofibrous structure of the natural extracellular matrix (ECM) and tried to fabricate various nano and microscaled structures to enhance cell activation. ECM is a complex structural entity surrounding and supporting cells that are found within mammalian tissues (Figure 1-4).

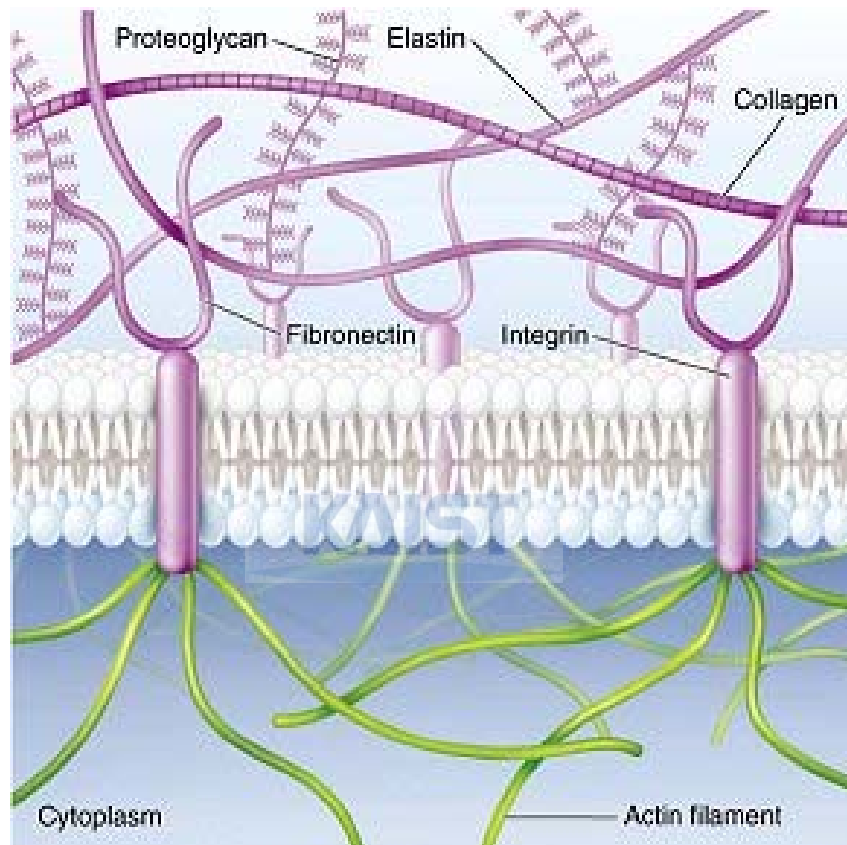


Figure 1-4. Extracellular matrix (ECM) [32].

It is mainly composed of proteoglycan hydrogels resisting compression force and various protein fibrils and fibers providing high tensile strength, such as collagen, elastin, fibronectin and laminin [33]. Since it was stated that a tissue provides a specific function in part through interactions of the cells with the ECM [34], much attention has been given to the fabrication of ECM-mimicking scaffold. Since the early 2000s, the electrospinning process has been held as a



highly promising technology producing nanofibers as thin as several nanometers which can be used as substitutes for the natural ECM structure.

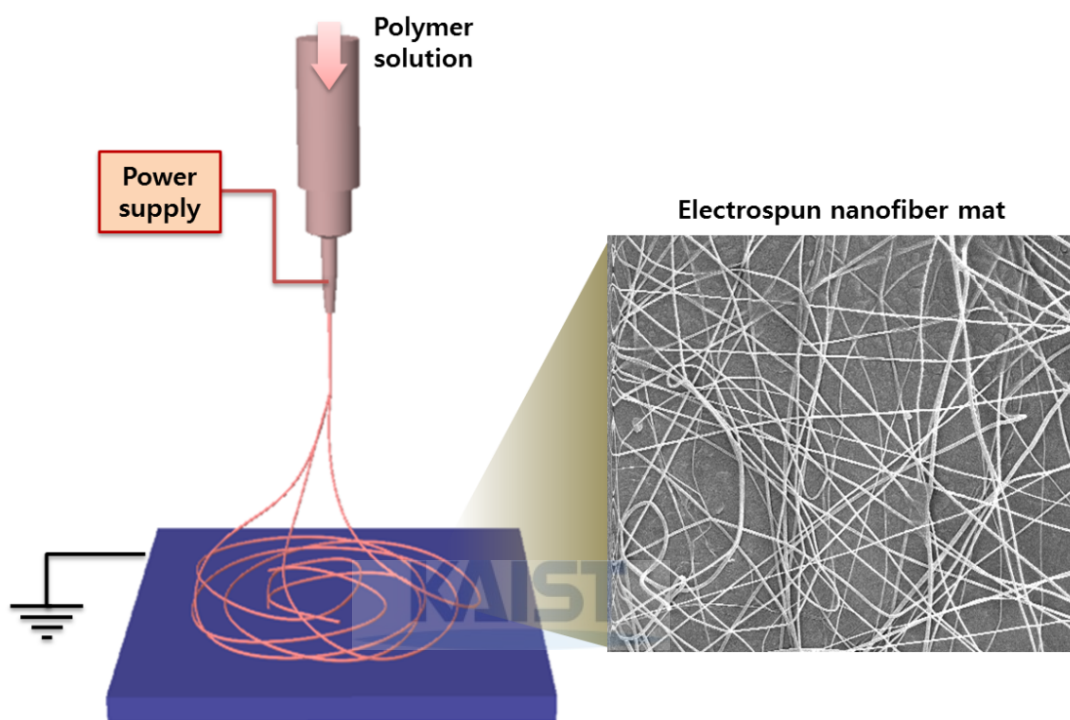


Figure 1-5. Schematic diagram of electrospinning process during which a drop of a polymer solution is ejected from the micro nozzle and spread onto a grounded substrate in the shape of a nanofibrous matrix.

The electrospinning method is different from the aforementioned SFF techniques in that it provides a nanofibrous scaffold. Such a nanoscaled architecture possesses high aspect ratio, high porosity, high surface area, low density, and small pore size so that it mimics the ECM structure. In this process, high direct-current (DC) voltage in the kilovolt range is applied to a polymer solution held in a metal needle. A polymer drop from the needle tip is deformed into a Taylor cone due to the repulsive electrostatic force that overcomes the surface tension of the

polymer solution, and a charged jet of the solution is then ejected from the tip of the Taylor cone. As the jet undergoes a stretching process and moves toward a grounded target (collector), it is accompanied by solvent evaporation, which results in nanofiber mats forming on the collector.

<b>Synthetic polymers</b>	<b>Poly(L-lactide)</b>
	<b>Poly(<math>\epsilon</math>-caprolactone)</b>
	<b>Poly(lactide-co-glycolide)</b>
	<b>Poly(ethylene oxide)</b>
	<b>Poly(vinyl alcohol)</b>
	<b>Poly(ester urethane)urea</b>
<b>Natural-derived polymers</b>	<b>Silk fibroin</b>
	<b>Hyaluronic acid</b>
	<b>Cellulose</b>
	<b>Collagen type I, II, III</b>
	<b>Chitosan</b>
<b>Blends/ combinations</b>	<b>Silk fibroin and poly(ethylene oxide)</b>
	<b>poly(<math>\epsilon</math>-caprolactone) and hyaluronan</b>
	<b>Collagen type I and poly(ethylene oxide)</b>
	<b>Collagen type I and poly(<math>\epsilon</math>-caprolactone)</b>

Table 1-3. Biodegradable polymers that are used to develop electrospun nanofibers.

Additionally, more functions of electrospun nanofibers have been added by some methods including mixing bioactive agents or polymers with the spinning solutions and surface modification of the scaffold [35]. And combinations of synthetic and natural polymers provided

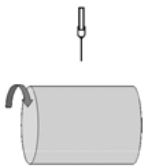
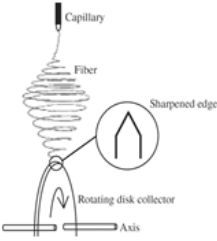
mechanically stronger structure and preferred surfaces for cell attachment. Table 1-3 shows the spinnable materials for the scaffolds including synthetic polymers, natural-derived polymers, and their blends [36].

Numerous studies have been conducted about nano-structured scaffold, which is believed to enhance cellular activity such as cell migration, growth, proliferation, and differentiation. Thus, much potential of the utilization of electrospun nanofibers is implied in tissue engineering applications. Various types of cells have been used with electrospun nanofiber scaffolds including chondrocytes [37], fibroblasts [35, 38], myoblasts [39], smooth muscle cells [40], osteoblasts [41], and etc. So far, the electrospun nanofiber scaffolds have been applied to many different types of tissues such as blood vessel, cartilage, bone, muscle, and nerve.

Because of the inherent characteristic of the electrospinning process, the formed nanofibers are deposited with randomly oriented configuration. Recent electrospinning techniques have focused on uniaxial alignment of nanofibers. The ability to obtain the aligned fiber structures led to the specific applications where cells or tissues should be organized with the oriented configuration. For example, skeletal muscle tissue is composed of bundles of highly oriented muscle fibers and cells [42]. Along the several works, the aligned nanofiber scaffolds are expected to have potential for blood vessels [43], neural tissue [44], muscle tissue [42], and ligament tissue [45]. Moreover, cell adhesion and proliferation are significantly enhanced on the aligned nanofiber scaffolds [43]. Consequently, the fabrication of aligned nanofiber scaffold plays an important role in the specific parts of tissue engineering applications.

Several approaches have been proposed for fabricating aligned nanofibers. Firstly, a rotating mandrel was used as a ground target with controlling the rotation speed of the mandrel [46, 47]. This technique is a simple method to collect the aligned fibers along the circumference of the target mandrel. Instead of the simple mandrel, some researchers tried to improve the orderliness of electrospun fibers employing other rotating objects such as a spaced wire drum

[48]. As it rotated aligned nanofiber sheets were collected on the drum. By aid of convergence of electrostatic fields, A rotatable disk collector which has a knife-edge can be used [49]. As the electrospun jets travel toward the disk, the jets tend to converge onto the knife-edge and are wound along the knife-edge of the rotating disk. While previous mentioned methods are based on employment of a mechanically rotatable collector, the aligned nanofibers can be fabricated purely through a design of an electrostatic field between the needle and the collector [50, 51]. When two pieces of parallel conductive electrodes are placed with a gap, the electric field lines near the electrodes are split into each edge of the parallel electrodes. Thus electrospun jets are stretched and aligned across the gap due to influence of the electrostatic field profile. On the other hand, an alternating-current (AC) high voltage supply can be used for the fiber alignment instead of the typically used direct-current (DC) voltage [52]. The use of AC potential was shown to reduce the chaotic path of the electrospun jets, and minimize accumulation of the residual charges on the jets. Table 1-4 summarizes the aforementioned alignment techniques including their features and limitations.

Schematic diagram	Feature	Limitation
	<b>&lt; Rotating drum &gt;</b> <ul style="list-style-type: none"> <li>- Simple setup</li> <li>- Fabrication covering large area</li> </ul>	<ul style="list-style-type: none"> <li>- Not high order of alignment</li> <li>- Occurrence of Broken fibers due to too high rotating speed</li> </ul>
	<b>&lt; Rotating disk &gt;</b> <ul style="list-style-type: none"> <li>- Simple setup</li> <li>- High order of fiber alignment</li> </ul>	<ul style="list-style-type: none"> <li>- Narrow area of fiber array</li> <li>- Impairment of fiber alignment as the deposited fiber array becomes thicker.</li> </ul>

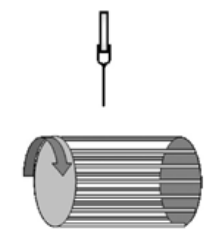
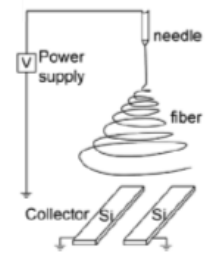
	<p><b>&lt; Rotating wire drum &gt;</b></p> <ul style="list-style-type: none"> <li>- Simple setup</li> <li>- High order of fiber alignment</li> </ul>	<ul style="list-style-type: none"> <li>- Difficulty in obtaining thick layer layer of fibers</li> <li>- Not alignment throughout the whole region</li> </ul>
	<p><b>&lt; Parallel electrodes &gt;</b></p> <ul style="list-style-type: none"> <li>- Simple setup</li> <li>- High order of fiber alignment</li> <li>- Easy transfer of fibers onto another substrate</li> </ul>	<ul style="list-style-type: none"> <li>- Difficulty in obtaining thick layer layer of fibers</li> <li>- Limit in length of aligned fibers</li> </ul>

Table 1-4. Several electrospinning setups to obtain oriented fiber arrays.



## 1.3 Objective and scope of the study

To date, large amount of efforts in scaffold-based tissue engineering have been devoted to fabrication of 3D scaffolds optimized to specific tissue or cell on a case-by-case basis. Potential fabrication methods of such scaffolds have been developed as has been mentioned including the conventional methods, RP processes, electrospinning, and nanolithographic methods. Among them, RP and electrospinning processes are expected to be the most promising. The rapid prototyping methods allow precisely tuning such factors as the pore network and geometry in a CAD/CAM manner. And the electrospinning process allows producing cyto-compatible nanofibrous architectures which mimic the natural ECM environments. Although both techniques have shown favorable outcomes and potential applications in separate fields, the fabrication methods have some limitations when they are applied alone. Typical RP scaffold has relatively

---

large pores and features of several hundred micrometers, which is much larger than the cell scale. Despite of its 3D applicability, the limitation of large scale could be an obstacle to cell attachment and induction of other cellular activities such as migration, proliferation and differentiation. On the other hand, such cellular behaviors can be greatly enhanced by the application of electrospun nanofibers. However, it is considered difficult to obtain 3D macro-scale scaffolds for the practical use. Furthermore, the relatively small pores of the electrospun nanofiber scaffolds compared to the cell size may cause poor conditions including nutrient supply, metabolic waste removal, and cell migration within the scaffolds.

In these regards, the main objective of this thesis is to develop a new conceptual integration process for novel 3D scaffolds mimicking the biophysical environment. The integration process consists of two-step alternating process including direct polymer melt deposition (DPMD) process and electrospinning. The developed scaffold is characterized by a micro/nano dual-scale hierarchical structure in a form of 3D construct incorporating the electrospun nanofibers. This newly integrated scaffold overcomes the limitations caused by application of either RP or electrospinning. As two methods are merged together, the integrated process provides both the 3D applicability and the improved cell activation.

In Chapter II, the characteristics and biomedical applications of the DPMD process are described. In order to implement 3D architecture for the tissue engineering scaffolds, the DPMD apparatus is integrated. The DPMD process employs fine-bore nozzle for micro-extrusion, syringe barrel with heating device, pressure controller with air compressor, and 3D moving micropositioning system. Through extrusion of molten material along a CAD-based nozzle path, the 3D scaffolds can be fabricated considering pore size, porosity, and overall shape. As well as the 3D hybrid scaffold in the following chapter, some applications using the DPMD process alone are addressed in this chapter.

Chapter III describes fabrication of electrospun nanofibers as a constituent of the 3D

hierarchical scaffold. The available electrospun nanofibers for the scaffold are classified by their configuration such as randomly oriented mesh and uniaxially aligned array. The random nanofiber mats are obtained by fundamental electrospinning apparatus under appropriate combination of process parameters. On the other hand, uniaxially electrospun nanofiber arrays are built by introducing a newly designed collector, which is characterized as an inclined gap alignment technique. For this method, adequate process conditions should be derived including solution concentration and spinning distance from needle to collector. As the method allows transfer onto another substrate, the use of the resultant aligned fibers can be diversified.

In Chapter IV, the characteristics of the controlled nanofiber mats and cell guidance phenomena on the nanotopography are described. The uniaxially electrospun nanofiber arrays were constructed with quantitatively controlled density. As a single transfer of the nanofibers collected from the inclined gap provided a well-aligned and regularly-distributed form, the developed nanofiber array could be applied to tissue scaffold by employing multiple transfers. The fiber density within a scaffold could be controlled in proportion to the number of transfers. Diameters of the nanofibers in the scaffold lay in a sub-micrometer range, which means that the fibers were appropriate to utilize as nano-topographic features. In regard to the contact guidance along the aligned direction of the nanofibers, favorable interactions between the fibroblasts and the developed scaffold, especially in a highly dense scaffold with the fiber spacing reduced down to less than cell size, were revealed in observation of cell morphologies.

Chapter V deals with the implementation of dual-scale hierarchical structures by incorporation of electrospinning and the DPMD process. A hybrid process for fabrication of 3D scaffolds which consisted of a microfibrinous woodpile structure fabricated using the DPMD and nanofibrous matrices by an electrospinning method was tried. Insertion of the nanofiber mats between the layers of 3D structure causes different conditions in the thermally self-bonding procedure from the case using DPMD alone. This chapter focuses on the characterization of the

---

thermal fusion process between the nanofiber mat and the deposited microfiber so that it is feasible to fabricate the dual-scale hierarchical scaffold using both electrospinning and the DPMD process.

Chapter VI shows the various applications for 3D-fasioned tissue formation using the developed fabrication methods. The outcome from the developed fabrication method shows more preferable 3D biomimetic structure and many potential applications using various cell lines, such as chondrocyte, mesenchimal stem cell (MSCs), and myoblast. As the random nanofiber meshes composed of collagen and PCL are inserted within the 3D scaffold, the scaffolds can provide a 3D structure to support tissue ingrowth as well as functionality related to surface affinity and an additional surface area for improved chondrocyte attachment and proliferation. Also from not only the random mesh but also the aligned fiber array, the improved cell activation was confirmed by employing MSCs culture experiments. For a prolonged application, a parallel layer-by-layer approach for 3D cell/fiber integration is introduced to enlarge the application of electrospun nanofiber structure to 3D muscle tissue engineering.





---

## CHAPTER II

# DIRECT POLYMER MELT DEPOSITION (DPMD) PROCESS

### 2.1 Introductory remarks

In recent tissue engineering strategies, most researchers have focused on scaffold-based techniques for successful regeneration of tissues or organs by cell adhesion, proliferation and differentiation in three-dimensional porous scaffolds [53]. There are some structural factors that should be considered in constructing the scaffolds besides material issues. Such factors have influence on cell attachment, survival, growth and reorganization as well as on the overall behaviour of tissue regeneration. As for design of scaffolds, the following characteristics should be provided: (i) a three-dimensional macro structure to replace a damaged tissue; (ii) a highly micro-porous structure with pore interconnectivity to support and culture tissue cells within it; (iii) optimal pore size for each application of tissues; (iv) bio-compatible and bio-degradable structure in vivo; (v) large surface area and suitable surface chemistry to improve cell attachment and migration within the structure; (vi) mechanical properties to support the region of implantation [5].

Due to limits of shape controllability and repeatability in the previously-stated conventional approaches, solid freeform fabrication (SFF) based fabrication methods have been introduced to manufacture tissue engineering scaffolds. These SFF based approaches hold considerable

promise as tissue regeneration strategies, especially in terms of morphological controllability. SFF techniques are based on CAD systems so that a precisely controlled outer shape and pore network can be realized. SFF techniques, also known as rapid prototyping (RP) techniques, have some significant advantages including customized design via CAD models, computer-controlled fabrication, anisotropic scaffold microstructures and a diverse range of processing conditions. Currently possible SFF techniques adapted for fabricating tissue engineering scaffolds are Three-dimensional printing (3D-P), Fused deposition modelling (FDM), Selective laser sintering (SLS), and microstereolithography (MSTL). These SFF techniques provide more advanced controllability of the process and the fabricated structure than the conventional methods. However, some SFF techniques, MSTL for instance, have drawbacks such as a narrow range of available materials due to its use of the photopolymerizing process. FDM has difficulty in pre-processing materials necessarily as filaments, as well as a limit on available materials due to use of only filament-shaped precursors. 3DP is also cumbersome in post-processing of removal of internal unbound powder; furthermore, the removal process is not always completed. Residual powder within the scaffolds may cause problems in vivo.

In this chapter, we developed Direct Polymer Melt Deposition (DPMD) process in order to overcome the aforementioned shortcomings via conventional methods and previous SFF methods. This process is a highly versatile instrument for fabrication of various bio-applicable structures in the field of tissue engineering. It also provides universality of available biopolymers by controlling the processing temperature. This chapter is focused on the characterization and applications of the DPMD process and the scaffolds composed of the extruded microfibers. Furthermore, DPMD process can be also utilized for fabricating framework structure of hybrid construction continued in the following chapter.

## 2.2 Polycaprolactone (PCL) and material property

Polycaprolactone (PCL) is a semicrystalline, biodegradable polymer belonging to the aliphatic polyester family (Figure 1). PCL has been shown to degrade by random hydrolytic scission of its ester groups, and under certain circumstances, by enzymatic degradation [54]. The biodegradability and extensive *in vitro* and *in vivo* biocompatibility have allowed PCL to be applied to a number of medical and drug delivery devices. At present, PCL is regarded as a soft and hard-tissue compatible material including resorbable suture, drug delivery system, and recently tissue engineered scaffold.

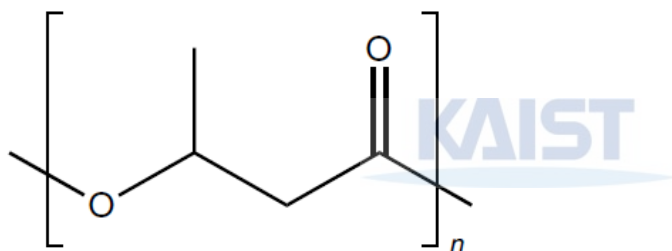


Figure 2-1. Chemical structures of Poly( $\epsilon$ -caprolactone).

Polymer	Weight average molecular weight	Glass transition temp. (°C)	Melting temp. <sup>a</sup> (°C)	Decomposition temp. (°C)	Heat of fusion <sup>a</sup> (Jg <sup>-1</sup> )	Tensile strength (MPa)	Tensile modulus (MPa)	Flexural modulus (MPa)	Elongation at yield (%)	Elongation at break (%)
<b>Poly(<math>\alpha</math>-Hydroxy Ester)</b>										
PLGA	50,000	35	210	254	71	—	—	—	—	—
P(L)LA	50,000	54	170	242	41	28	1,200	1,400	3.7	6
P(L)LA	100,000	58	159	235	20	50	2,700	3,000	2.6	3.3
P(L)LA	300,000	59	178	255	39	48	3,000	3,250	1.8	2
P(D,L)LA	21,000	50	A	255	A	—	—	—	—	—
P(D,L)LA	107,000	51	A	254	A	29	1,900	1,950	4.0	6
P(D,L)LA	550,000	53	A	255	A	35	2,400	2,350	3.5	5
Poly( $\epsilon$ -Caprolactone)	44,000	-62	57	350	34	16	400	500	7.0	80

Table 2-1. Thermal and mechanical properties of respective synthetic biodegradable polymers.

The other aliphatic polyesters include poly(lactide) (PLA), Poly(glycolide) (PGA), and poly(lactide-co-glycolide) (PLGA), and also provide a variety of bio-medical applications. Table 2-1 shows some thermal and mechanical properties of the respective polymers. Among these materials, PCL is an easily extrudable biomaterials due to its favorable property of thermoplastic behavior. Because it has a low glass-transition temperature of  $-62^{\circ}\text{C}$ , a low melting temperature of  $57^{\circ}\text{C}$ , a high decomposition temperature of  $350^{\circ}\text{C}$  [54], the thermoplastic processing such as extrusion, casting, and molding can be easily performed with a wide range of processing temperatures. The variation of viscosity according to shear rate is relatively smaller than that of other polymers such as polystyrene (PS). The wide range of flow shear rate as well as temperature is advantageous in that phase transition of the material is necessary in the fabrication process. Furthermore, due to the low glass-transition temperature below zero, the pliable property of PCL around the room temperature and body temperature provides unique usefulness of PCL structures as well as PCL itself in a variety of biomedical applications.

As the proposed fabrication process is based on polymer extrusion, the viscosity of molten polymer is very important for the precise fabrication. In other words, the significant material property influencing on the polymer flow rate through the nozzle is the viscosity, which is varied with temperature and shear rate condition. To measure the melt viscosity of PCL, Advanced Rheometric Expansion System (Rheometric Scientific, USA) was used. As shown in Figure 2-2, the molten PCL show higher viscosity according to decrease of temperature and shear rate like any other viscoelastic material.

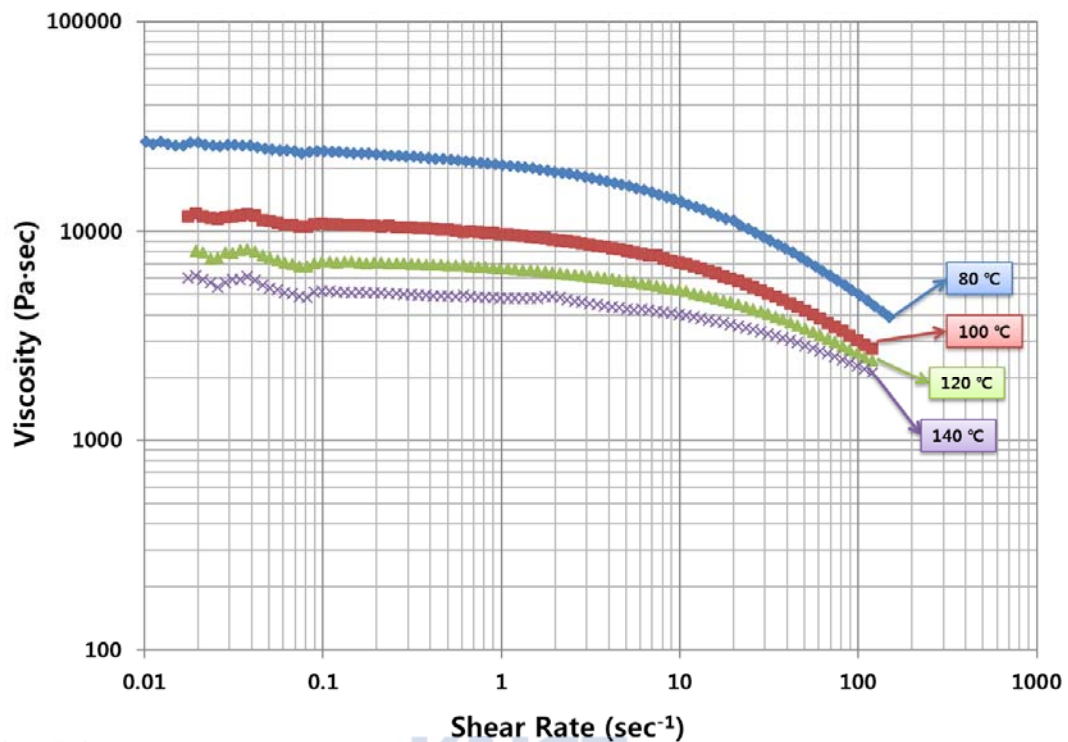


Figure 2-2. Viscosity of molten PCL as a function of shear rate, for four temperatures.

Throughout this study, PCL (440744-250G, Mw 80000, Sigma Aldrich) was employed. The PCL is provided in granule form and Granules of the raw material were fed into a heated syringe and melted as syringe temperature rose over the melting temperature of 60°C.

## 2.3 Direct Polymer Melt Deposition (DPMD) apparatus

### 2.3.1 Procedure of the DPMD process

Figure 2 shows concepts of the microfabrication process using the polymer melt extrusion method. The system for the proposed process consists of three main components: (1) a

stainless steel syringe equipped with micro-nozzle and syringe heating device; (2) an air compressor with pressure-controllable dispenser; (3) a three-dimensional micropositioning system based on CAD/CAM.

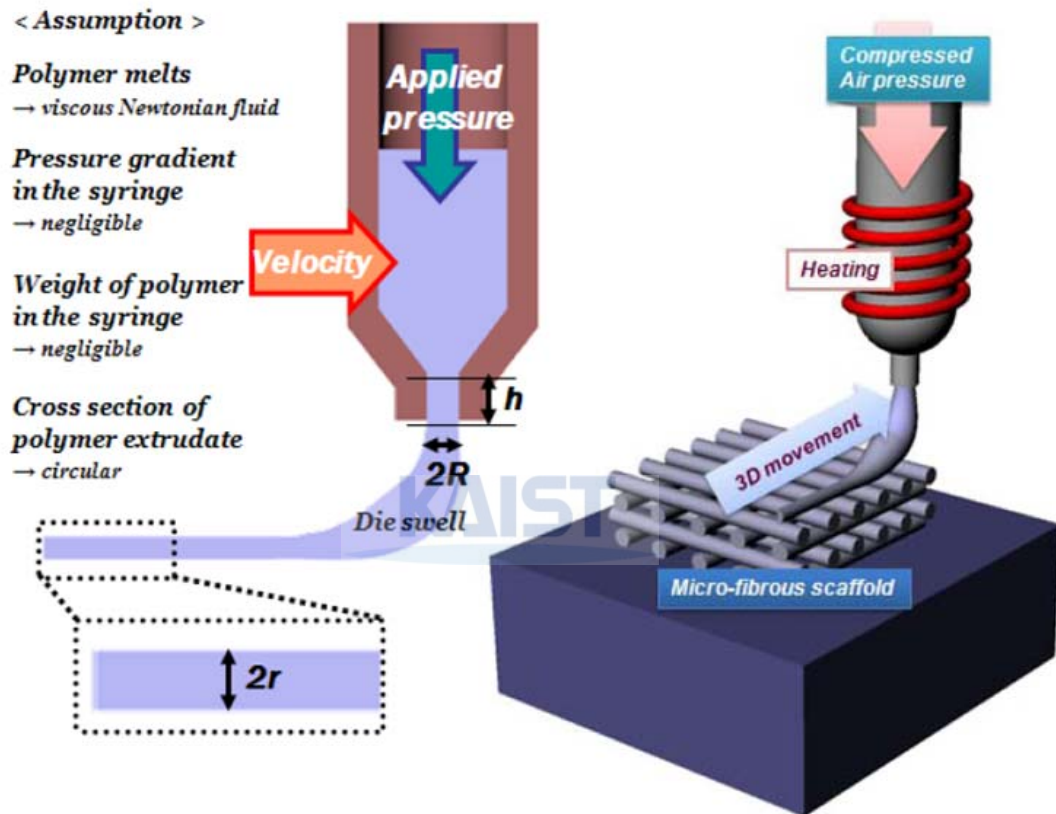


Figure 2-3. Schematic diagram of the DPMD process.

The sequence of 3D integration of micro-extruded structure is briefly as follows. As the heat input of the coiled heater deployed around the syringe and the nozzle can be controlled by temperature controller, the process temperature can be variously selected above melting point. This controllability allows the thermoplastic polymer to be in variable melt viscosity affecting the resultant micro-extrudates. When compressed air is applied to the polymer melts in the syringe,

---

fiber-shaped polymer melts are extruded out through the micronozzle. Three-dimensional movements of the micronozzle according to the tool-path based on the scaffold morphology can fabricate 3D microfibrinous structures while the material is extruded. In this process, principal process parameters that affect the characteristics of the resultant fibrous scaffolds are the diameter of the micronozzle, the temperature of the material process, the pressure of the compressed air and the velocity of the nozzle.

### *2.3.2 Apparatus of the DPMD process*

Figure 2-4 and 2-5 show the apparatus of DPMD process and its specification, respectively. The system of the proposed DPMD process consists of a stainless steel syringe with a micronozzle, a syringe heating device, a compressed air dispenser and a three-dimensionally moving micropositioning system. The heated syringe with micro-nozzle utilizes a stainless steel syringe that has high thermal conductivity. It is possible to change the micro-nozzle to another with a different inner diameter. In the extrusion process, the inner diameter of the micro-nozzle is the principal process parameter that affects the features of the resultant extrudate. Therefore, exchangeable syringes with different micro-nozzles allow the fabrication of various microscaled structures. The micro-nozzles come in a diameter range from 0.2 to 1.2 mm. The temperature of the syringe and the nozzle is also one of the main process parameters, and the syringe module is surrounded with the coil heater generating the heat up to 400°C.

This process employs a pneumatic pressure control system driven by filtered compressed air instead of by a plunger. It applies high pressure into the syringe at up to 1.2 MPa using the air compressor and pressure booster. When compressed air is applied to the polymer melts within the heated syringe, a micro-fibrous extrudate emerges from the nozzle. Then, three-dimensional motion of the nozzle allows deposition and formation of three-dimensional non-random porous



structures. Employing a ball screw, stepping motor and motion guide modules, the three-dimensionally moving micropositioning system has enough accuracy and repeatability to allow control within a few micrometers. As well as the precise positioning control, the velocity of the syringe module can be uniformly controlled in a range from several hundred  $\mu\text{m}/\text{sec}$  to 40 mm/sec. The micropositioning system of the DPMD apparatus is controlled by a PC based control system. The movement control board can be applied to in personal computers of 1 Ghz or more. The objects subjected to control are three stepping motors, nine digital input ports and six digital output ports.

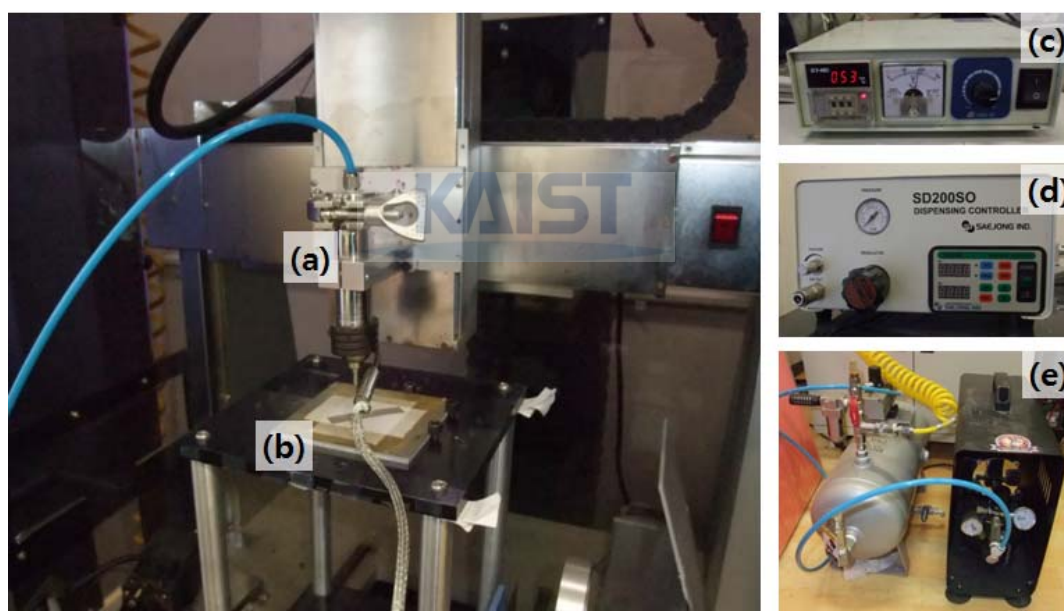


Figure 2-4. Overall configuration of DPMD apparatus; (a) stainless steel syringe with a micronozzle, (b) syringe heating device, (c) temperature controller, (d) compressed air dispenser, (e) air compressor and pressure booster.

---

Range of X, Y, Z axis	X	200 mm
	Y	200 mm
	Z	200 mm
Specifications of Tool	Nozzle diameter	200 ~ 1200 $\mu\text{m}$
	Tool speed	0 ~ 50 mm/s
	Dispensing pressure	0 ~ 6 kg/cm <sup>2</sup>
	Boosting ratio	$\times 0 \sim \times 2$
	Temperature range	RT ~ 400 $^{\circ}\text{C}$

Table 2-2. Specifications of the DPMD apparatus.

## 2.4 Process parameters for DPMD

### 2.4.1 Relationship among process parameters

A flow of fluid through a tube of specific length and diameter can be approximately expressed with the diameter or radius of the tube, the pressure drop between entrance and exit of the tube, the length of the tube, and the viscosity of the fluid [55]. Such a relationship is called Hagen-Poiseuille's law. In order to put an application of the equation into the developed process, several assumptions are needed, as follows.

- Polymer melts are viscous Newtonian fluids.
- Pressure gradient in the syringe is negligible.
- Weight of polymer in the syringe is negligible.
- Cross sections of the polymer extrudate and the deposited fiber are circular

According to Hagen-Poiseuille's equation, the volume rate ( $Q_e$ ) of polymer melt flow ejected from the nozzle can be simplified as:

$$Q_e = \frac{\pi R^4 \Delta P}{8h\eta} \quad (2.1)$$

where  $R, \Delta P, h$  and  $\eta$  are the inner radius of the nozzle, the pressure drop, the length of extrusion path inside the nozzle, and the viscosity of polymer melts, respectively.

On the other hand, the volume rate ( $Q_d$ ) of the deposited extrudate can be approximated as follows:

$$Q_d = \frac{dV}{dt} = \pi r^2 \frac{dl}{dt} = \pi r^2 v \quad (2.2)$$

where  $V, r, l, t$ , and  $v$  are the volume of deposited extrudate, the radius of the deposited fiber, the length of the deposited fiber, time during polymer deposition, and the velocity of polymer deposition (the velocity of the syringe).

We know that the volume of the deposited extrudate is equal to the volume of polymer melt flow ejected from the nozzle; thus, an expression for the radius of the deposited fiber can be obtained by substituting Equation (2.1) into Equation (2.2):

---


$$r = \sqrt{\frac{R^4 P}{8vh\eta}} \quad (2.3)$$

As shown in Equation (2.3), the value of the deposited fiber radius is expected to be in proportion to the square of the radius of the nozzle and the square root of the pressure drop (applied pressure into the syringe), and in inverse proportion to the square root of the velocity of the syringe module.

#### *2.4.2 Microfiber deposition test*

The experiments were performed to analyze the relationship between the aforementioned two main parameters and the geometry of the resultant deposited fiber. The parameters included the moving velocity of the syringe module, and the applied air pressure into the syringe. As for the features of the nozzle, the lengths of extrusion path inside the nozzles are uniform at 1 mm for all nozzles used in this system. The inner diameter of the nozzle connected to the syringe was 200  $\mu\text{m}$ , and the temperature of the coil heater was determined to be 140°C. In order to compare between the experimental and the theoretical results, Equation (2.3) was used to calculate the radius of theoretical product. According to the data of Figure 2-2, the viscosity ( $\mu$ ) of the PCL melt changes depending on the temperature and the shear rate ( $\dot{\gamma}$ ). The shear rate of the molten material can be obtained by Equation (2.4):

$$\dot{\gamma} = \frac{4Q}{\pi R^3} \quad (2.4)$$

Where Q is the practical volume of the extruded fiber. Under the several conditions of the process parameters, the calculated shear rates and the relevant values of results are listed in

Table 2-3.

h	R	v	P	shear rate	$\eta$	calculated r	experimental radius
1	0.2	0.5	750000	15.6	3740	0.283	250
1	0.2	1	750000	17.1	3682	0.201	185
1	0.2	1.5	750000	19.2	3610	0.166	160
1	0.2	2	750000	19.6	3610	0.144	140
1	0.2	0.5	400000	9.5	4030	0.199	195
1	0.2	1	400000	9.8	4030	0.140	140
1	0.2	1.5	400000	11.7	3972	0.115	125
1	0.2	2	400000	12.1	3922	0.100	110

Table 2-2. Calculated shear rate and measured viscosity of PCL melts.

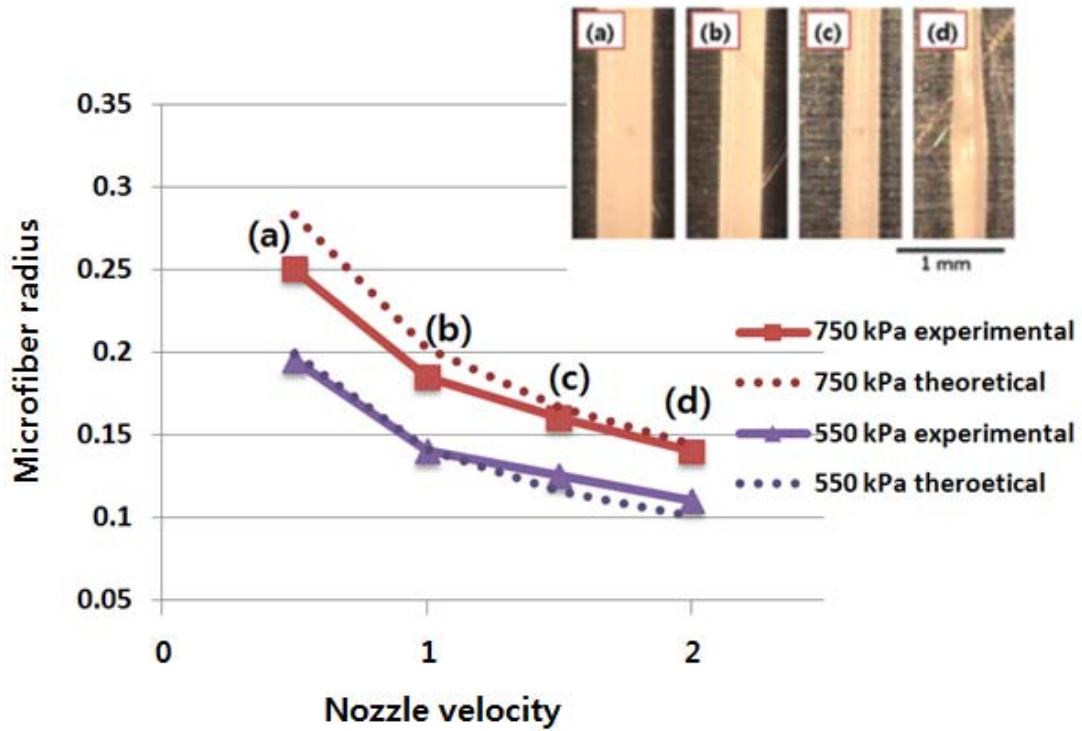


Figure. 2-5. Relationship of the deposited fiber radius versus velocity of the nozzle and applied air pressure.

Figure 2-5 shows the resulting features of the deposited fiber for each experiment. As shown in Figure 2-5, the solidified fiber radius decreases with the increase of velocity and the decrease of pressure, respectively. The variation of the experimental results has a tendency similar to those of the theoretical values.

Therefore, using the relationships between the applied air pressure ( $P$ ), the moving velocity ( $v$ ), and the shear rate ( $\eta$ ) of PCL melt, the effective sectional area ( $\Omega$ ) can be defined as

$$\Omega = \sqrt{\frac{P}{v\eta}} \quad (2.5)$$

From this value, the extruded fiber radius ( $r$ ) can be expressed as

$$r = \sqrt{\frac{R^4 P}{8vh\eta}} = \sqrt{\frac{R^4}{8h}} \cdot \sqrt{\frac{P}{v\eta}} = k \cdot \Omega \quad (2.6)$$

Experiments were carried out with fiber extrusion at various effective extrusion rates. As shown in Figure 2-6, the radius of the extruded fiber is tended to be proportional to the effective sectional area.

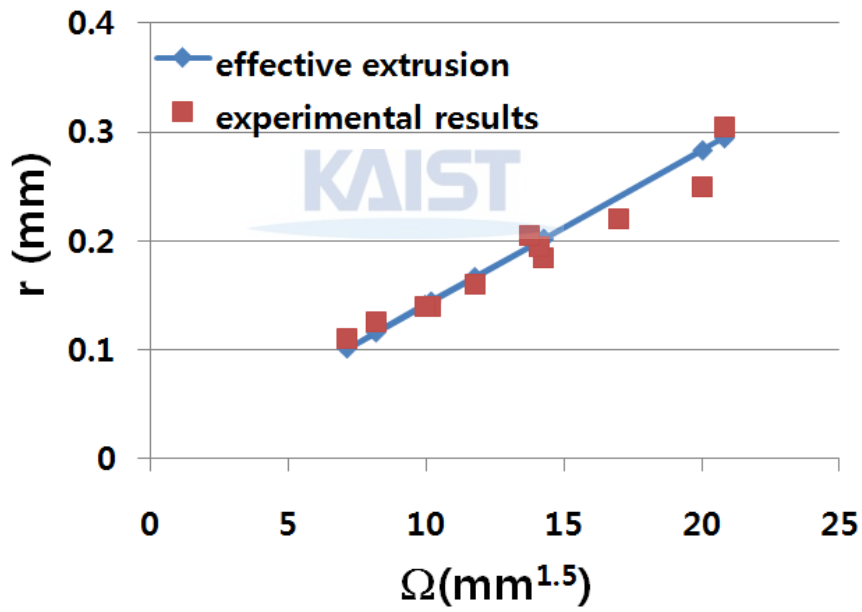


Figure 2-6. Relationship between effective sectional area and fiber radius.

The extruded fibers consist of three-dimensionally integrated scaffold and determine the overall architecture of the scaffold. Therefore the radius of the extruded and deposited fiber is significant factor for the scaffold design. It can influence on overall shape of scaffold, pore

---

morphology, porosity, and mechanical property of scaffold. As given by Equation (2.6), the effective sectional area of the extruded fiber using the process parameters is defined, thereby facilitating the well-defined deposition process and scaffold design.

#### *2.4.3 Design and fabrication of 3D scaffolds*

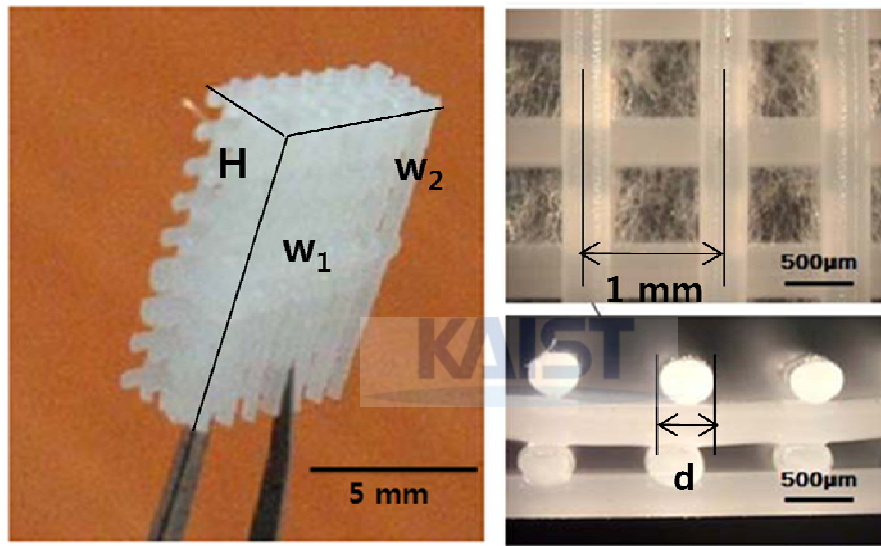
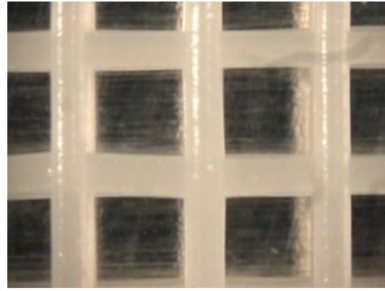


Figure 2-7. Resultant 3D scaffold fabricated by DPMD process.

Figure 2-7 shows morphology of the 3D woodpile-shaped scaffolds composed of micro-scaled fibrous extrudate of which the radius is  $365 \pm 15 \mu\text{m}$ . The inner diameter of the micro-nozzle connected to the syringe was  $400 \mu\text{m}$  and the processing temperature was determined to be  $140 \pm 5 \text{ }^\circ\text{C}$ , The applied air pressure for the dispensing process was determined to be  $0.55 \pm 0.05 \text{ MPa}$ . Velocity of the 3D micropositioning system was  $1.4 \text{ mm/sec}$ . Orthogonal stacking of each fibre array was successfully conducted. Thus, it can be observed from Figure 2-7 that fully-interconnected pores are formed within the porous scaffold and the arrangement and the shapes



of the deposited microfibrils have high degrees of uniformity and consistency. Lastly, control of scaffold morphology is achieved in this process by diversifying the geometry design and process parameters.



- Velocity : 1.0 mm/sec
- Pressure : 400±50 kPa
- $\Omega = 9.96 \text{ mm}^{1.5}$
- $r = 155 \text{ }\mu\text{m}$
- Porosity = 83%



- Velocity : 0.5 mm/sec
  - Pressure : 850±50 kPa
  - $\Omega = 21.19 \text{ mm}^{1.5}$
  - $r = 305 \text{ }\mu\text{m}$
  - porosity = 36%
- 

Figure 2-8. Other types of scaffolds with various porosity.

The theoretical porosity was calculated based on an estimation of the outer volume and the amount of deposited PCL microfibrils. It was assumed that the scaffold was cube-shaped, composed of long, cylindrical microfibrils.

$$(\text{porosity}) = \left(1 - \frac{nV_f}{V_w}\right) \times 100\%. \quad (2.7)$$

---


$$V_w = (\text{the volume of whole scaffold}) = w_1 w_2 H, \quad (2.8)$$

$$V_f = (\text{the volume of a microfiber}) = \frac{\pi l d^2}{4}, \quad (2.9)$$

where  $w_1, w_2, H, l, d$  and  $n$  are the scaffold width, scaffold length, scaffold height, fiber length, fiber diameter and number of fibers in the scaffold, respectively. In the case of 200  $\mu\text{m}$  radius as in Figure 2-7, the theoretical porosity from Equation (2.7) is determined to be approximately 70%. The fabricated scaffolds with various porosities can be obtained by adjusting the horizontal gap and the diameters of the microfibers, as shown in Figure 2-8.

## 2.5 Scaffold design and applications

### 2.5.1 3D framework for adipose tissue formation

Nanofilament(NF)-integrated multicellular spheroids and their integration with 3D microstructure for vascularized adipose tissue formation were developed in prof. Park's laboratory (in KAIST) [56]. The multicellular spheroids comprised of mesenchymal stem cells (MSCs) and synthetic nanofilaments as shown in Figure 2-9. Electrospun poly(L-lactic acid) (PLLA) nanofiber mesh was cut into pieces of nanofilaments by aminolysis fragmentation. The nanofilaments were surface-modified with RGD peptide by EGS coupling reaction and then self-assembled with MSCs in non-adhesive conical-bottom tubes after centrifugation. The formation procedure and the resultant spheroids are shown in Figure 2-9.

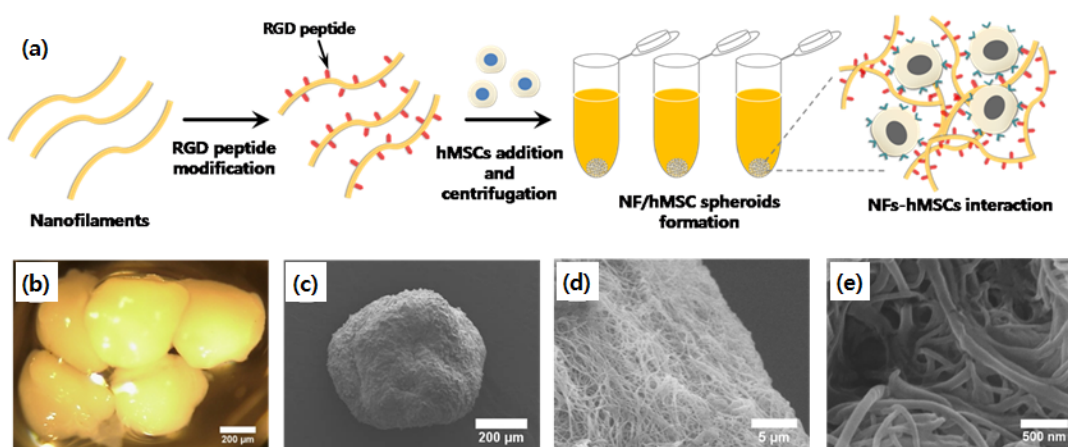


Figure 2-9. Preparation of NF/hMSC composite multicellular spheroids. (a) A schematic diagram illustrating the formation of composite spheroids (b) Stereoscopic image of as-prepared composite spheroids. (c) SEM image of the composite spheroid with overall shape. (d) High-magnification SEM images (e) Surface morphology of the composite spheroid showing nanoporous geometry [56].

With these multicellular spheroids, 3D bio-hybrid construction can be realized by incorporating the spheroids into the micro-structured scaffold fabricated by DPMD process. Figure 2-10 shows the assembly between spheroids and framework scaffold and the subsequent 3D construction through repeatedly interlocking each spheroids-framework hybrid unit by additive layer-by-layer manner.

The polymeric microstructured framework was fabricated the DPMD process described in previously. The process included firstly melting a bio-degradable polymer (polycaprolactone MW 80,000 in this work) in a heated barrel, extruding the molten polymer through a micro-scale nozzle (inner diameter = 400  $\mu\text{m}$ ) by applying compressed air, and finally depositing microfibrinous array and three dimensional solidified structure in a layer-by-layer (LbL) manner. The resultant structure provided the frame architecture of the hybrid construction by employing

3D woodpile-like microfibrillar structure with periodical void spaces. The extruded microfiber with 200  $\mu\text{m}$  diameter was obtained by adjusting the process parameters including applied air pressure (0.4 MPa) and moving velocity of the nozzle (2 mm/sec). The unit framework designed with a 2 bilayers configuration in the form of disc (diameter = 6 mm). And the spacing of the microfibrillar array making up the framework was determined as 400  $\mu\text{m}$  considering the spheroid size (over 400  $\mu\text{m}$ ) for successful placement of the spheroids into the void spaces.

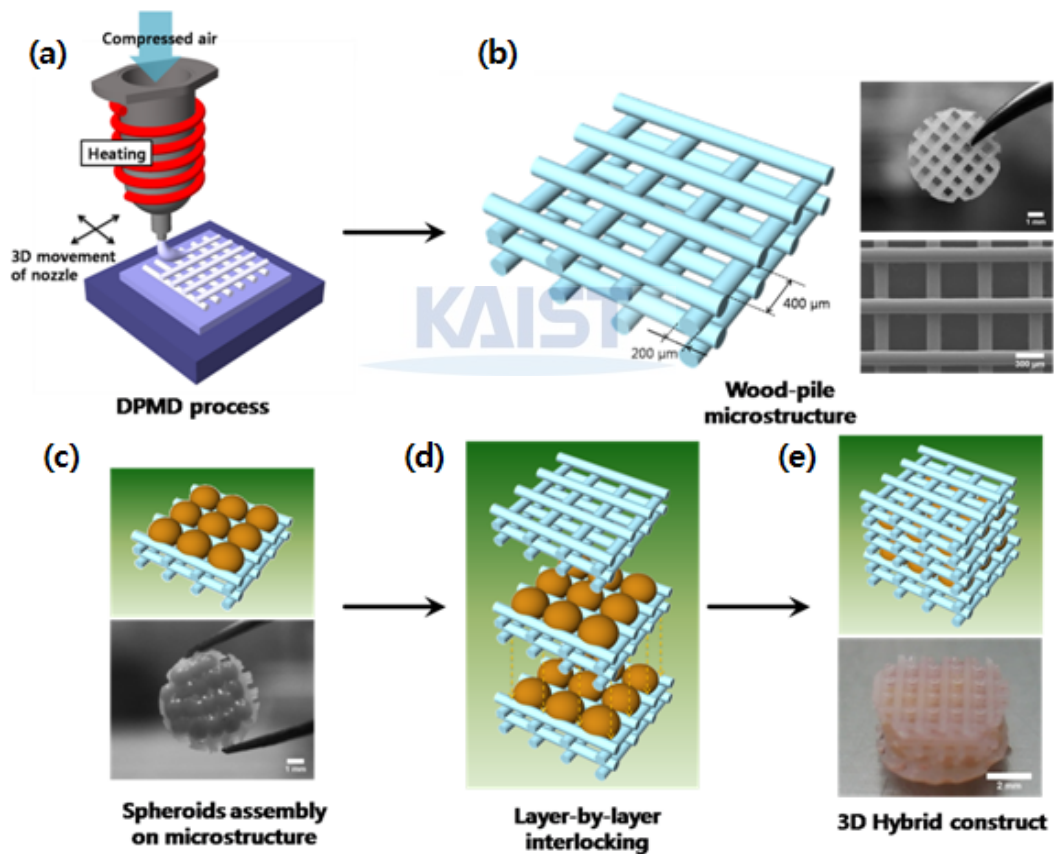


Figure 2-10. 3D biohybrid assembly with NF/hMSC composite spheroids and microstructured-scaffold. (a) Schematic illustration of DPMD process from PCL polymer. (b) The architecture of the fabricated scaffold with woodpile-like microfibrillar structure (fiber diameter  $\approx$  200  $\mu\text{m}$ , fiber spacing  $\approx$  400  $\mu\text{m}$ ). (c) The differentiated composite spheroids were

hexagonally packed along the ordered array of void spaces of microfibrinous scaffold and firmly anchored by cellular adhesion process. (d,e) 3D hybrid construct was built by successive stacking of spheroids-embedded scaffold units to form a complete 3D cylindrical geometry [56].

After aligning the spheroids along with periodical void spaces, further incubation for 30 min was performed to confirm the secure anchor of the spheroids by cellular adhesion process. And then these unit spheroids/framework hybrid layers were vertically interlocked to form terminal 3D shape by additive layer-by-layer fashion. These stacked hybrid constructs were further incubated for 1 h for every unit layers to attach to the adjacent layers by self-adhesion to form a complete 3D biohybrid constructs.

This fabrication strategy permits the hierarchical assembly through the cellular adhesion allowing the connection of the nanostructure and microstructure. In addition, due to the non-vascularized nature of the assembled spheroids, the blood vessel formation is crucially needed for overcoming aforementioned limitations of the current graft procedures. Thus, the microfabricated framework was allowed to deliver angiogenic growth factor for vascularized adipose tissue formation.

The woodpile-shaped frameworks were designed from the basis of the NF/hMSC spheroid diameter to conform to periodic gaps in the microfibrinous layer. Along a three-axis motion-controlled micropositioning system, the molten PCL polymer was dispensed through the micronozzle coupled to a stainless steel syringe surrounded with coiled heater [Figure 6(a)]. With this controllability of the CAD/CAM based process, the configuration of the framework such as fiber diameter, fiber spacing and void shape could go with the spheroid size or shape.

---

### *2.5.2 3D scaffold coated with functional materials*

As aforementioned in this chapter, 3D microstructured scaffolds with precisely defined architectures can be fabricated by the DPMD process, and thereby can have many promising features for tissue engineering applications, such as controllable porosity, desirable mechanical strength, and adjustable shape fitting to a tissue defect site. For the DPMD process, PCL was employed as scaffold materials. However, the surface of PCL structure has a limited property for cell adhesion due to its hydrophobicity. Thus surface modification with bioactive agents is additionally required.

Layer-by-layer (LbL) polyelectrolyte multilayer assembly is an attractive and facile surface modification approach, which generates a thin surface film from a few nano- to several micrometers in thickness with a precise control. It comprises of alternating deposition of polyanions and polycations on the basis of electrostatic force between two oppositely charged species, resulting in a self-assembled multilayer on the surface. Due to the versatility with regard to the introduction of any functional molecules into the multilayer, a wide variety of therapeutic components could be incorporated and released in a controlled manner. While the LbL assembly was often implemented onto the planar substrate due to a easy fabrication process, the challenge remains to assemble the multilayer on more complex three dimensional (3D) structures.

Hydroxyapatite (Hap) is a naturally occurring crystalline calcium phosphate ( $\text{Ca}_{10}(\text{PO}_4)_6(\text{OH})_2$ ) and is clinically used as an excellent substitute for mineralized hard tissue due to the similar composition to the mineral components of human bone and enamel. HAp itself or in the form of a bioactive coating on biomedical implant devices has been proven to offer better osteoconductivity, leading to ultimate osteointegration. Collagen is a major organic component constituting natural bone, and has been also used to create favorable extracellular milieu for

bone regeneration. The multicomponent scaffolds containing HAp and collagen would be highly desirable for bone tissue engineering due to the composite nature of bone matrix. For example, the apatite/collagen composite coating on a poly(L-lactic acid) (PLLA) porous scaffold was proven to improve osteoblast-like cell adhesion and osteoblastic activity. In addition, the composite of hydroxyapatite and collagen conjugated with hyaluronic acid exhibited good mechanical performance with excellent biocompatibility, ideal for bone tissue engineering materials.

Herein, the PCL-microstructured scaffold was fabricated by the DPMD process, and coated with hydroxyapatite/collagen nanocomposite in a layer-by-layer manner. Figure 2-10 shows the PCL scaffold and SEM images of its surface coated with nanocomposite materials. The scaffold was designed as the fiber diameter of 200  $\mu\text{m}$  and the fiber spacing of 400  $\mu\text{m}$ .

In order to verify the cyto-compatibility of the surface-modified scaffold, Human mesenchymal stem cells (hMSCs, Lonza, MD) were cultured within the modified scaffolds. The prepared specimens were three types including the bare scaffold without surface modification and the scaffolds coated with 5th and 20th bilayer deposition of HApNPs and collagen. The hMSCs suspension with culture medium (0.2 ml,  $2 \times 10^5$  cells) was loaded on both sides of the scaffolds. Four hours after seeding, cellular adhesion was investigated using CCK-8 assay kit (CCK-8, Dojindo laboratories, Kumamoto, Japan). And To assess hMSCs proliferation, total DNA content ( $n = 5$ ) was measured by using Hoechst 33258 (Sigma, St. Louis, MO), a fluorescent dye for staining double-stranded DNA. The examined time points were 3, 7, 12, 21 days after cell seeding.

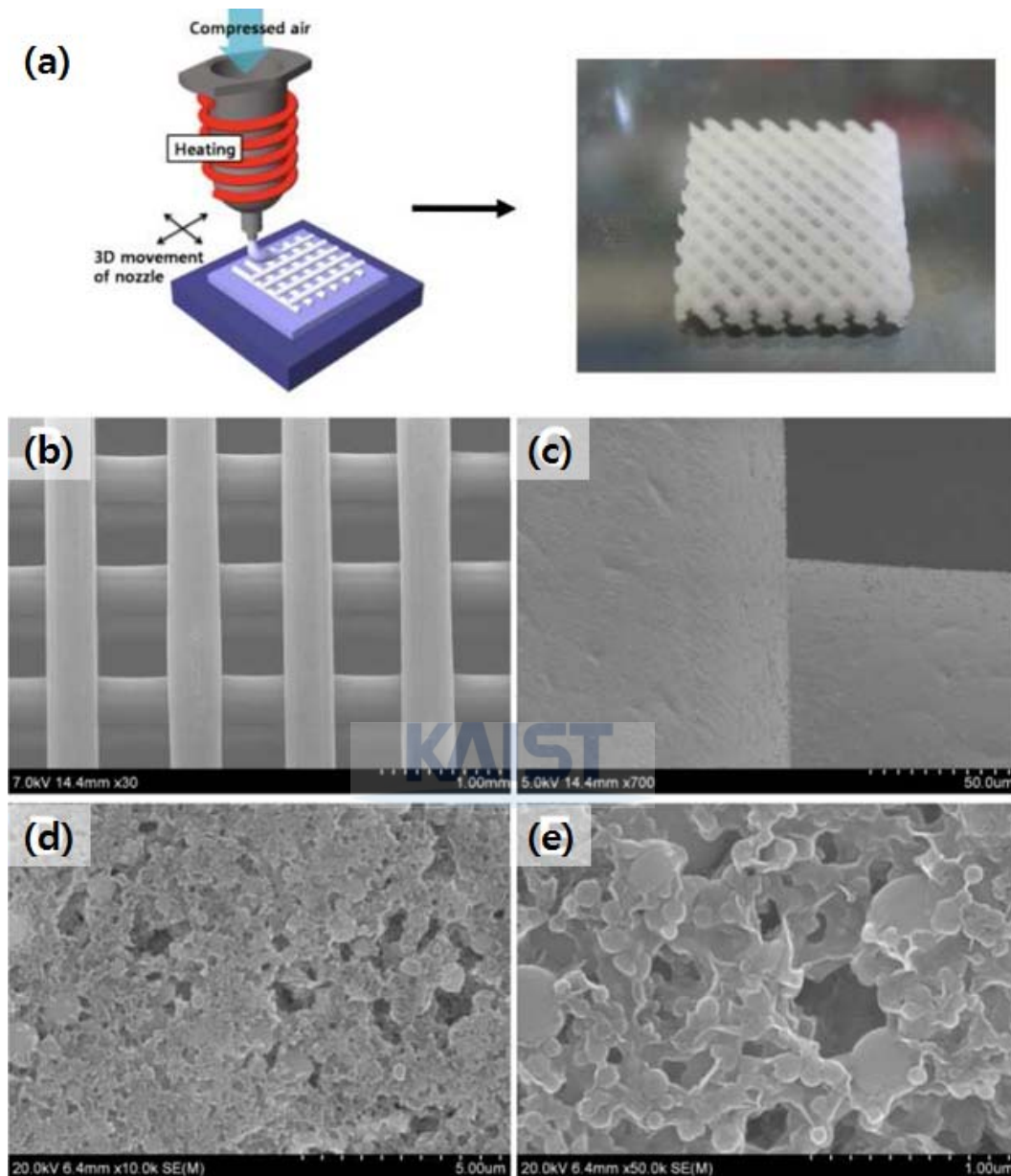


Figure 2-11. (a) Illustration of DPMD procedure giving rise to a 3D woodpile-like microfibrous scaffold. (b-e) SEM images of nanocomposite multilayer-coated scaffold with HApNPs and collagen.



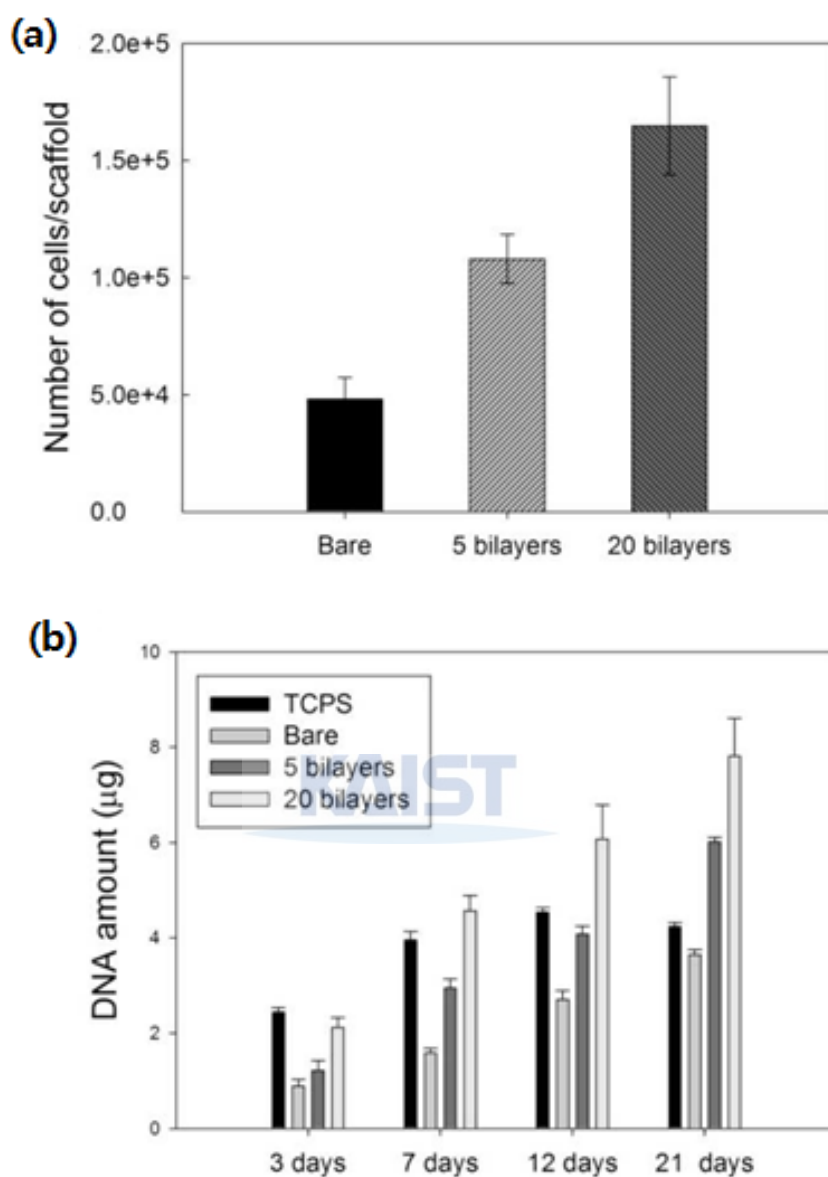


Figure 2-12. (a) hMSCs adhesion to bare, 5 bilayers-coated, and 20 bilayerscoated scaffold. (b) Quantification of DNA amounts of hMSCs on TCPS, bare, 5 bilayer-coated, and 20 bilayer-coated scaffold during 21 days of culture in growth medium.

As shown in Figure 2-12(a), the adhesion of hMSCs onto the scaffold coated with 20 nanocomposite multilayer was greatly enhanced as compared to bare scaffold (~230% increase).

---

In addition, cellular adhesion was significantly enhanced with the number of deposited layers. For assessment of hMSCs proliferation, DNA amount was quantified as a function of incubation period. As expected, the presence of surface multilayer played an important role in favoring the cellular growth in the scaffold.

#### *2.5.4 Controlled membrane for surgical application*

As the DPMD process employs the simple pressure-assisted dispenser as a fundamental mechanism of the process, a wide range of polymeric materials can be used including polymer solution dissolved in volatile solvent. When the polymer solution was deposited onto the substrate with chemical resistance such as stainless steel, glass, and Teflon-coated substrate, it solidified for a few seconds as accompanied by solvent evaporation. In other words, while the DPMD process produces the solid structure through solidification below melting point, the modified dispensing process makes it by the solvent evaporation. When the polymer solution was used in the dispensing process, the thinner thickness of the deposited layer can be attained by taking a higher velocity of nozzle movement and a lower applied pressure of compressed air. The process parameters including the velocity of 5 mm/sec and the pressure of 0.1 MPa provided the sheet-like thickness dimension of approximately 50  $\mu\text{m}$ . Figure 2-13 show the deposited membrane with PCL solution (20 wt% in methylene chloride). As seen in the figures, the resultant structure has a pliability due to its thin thickness (50~60  $\mu\text{m}$ ) and the rubbery property of PCL material. The pliable and flexible sheet-like structure can be applied in biomedical field requiring two-dimensional membrane.



Figure 2-13. Two dimensional sheet fabricated by deposition of PCL solution.

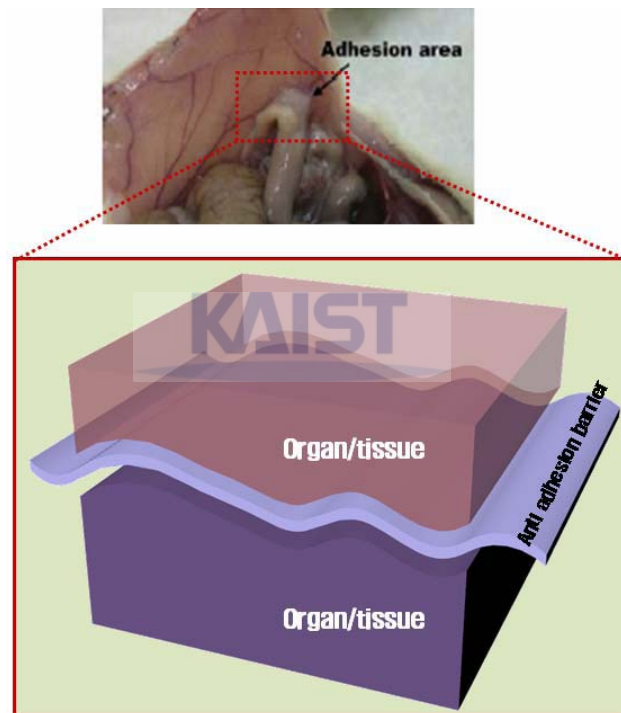


Figure 2-14. Concept of post surgical anti adhesion barrier.

One of the possible applications is post surgical anti-adhesion membrane. Tissue adhesions occur after surgical treatment, most frequently of peritoneum and pelvis. Though the adhesion is a physiologically important part of wound healing, undesirable adhesions after surgical treatment often derive harmful effect, functional obstruction, and re-operative surgery [57]. In order to

reduce postsurgical adhesion formation, the use of physical barriers has been attempted. The concept of anti-adhesion barrier is illustrated in Figure 2-14.

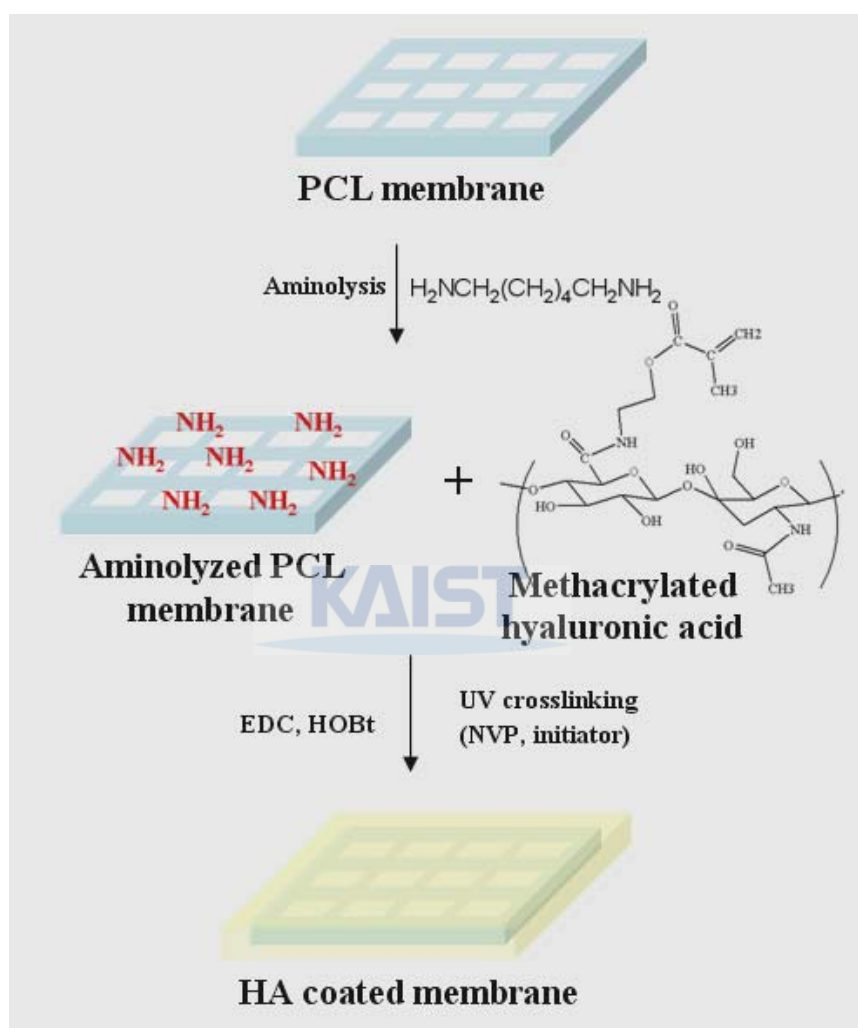


Figure 2-15. Schematic diagram for coating HA gel on the PCL membrane.

Various natural and synthetic polymer films, membranes, and nonwoven fabrics have been developed as non-absorbable or absorbable physical barrier materials. In this research, the aforementioned PCL sheet was used as a basal structure of the anti adhesion membrane, and

incorporation of hydrogel in the membrane was additionally performed. In order to assure the structural pliability, the basal membrane was designed as a void-including structure. Because the voids in the membrane can cause impairment of physical anti-adhesion, filling the void space with other soft materials was required. Hyaluronic acid (HA), which has been popularly used for biomedical applications because of its various biological functions, was employed for the filling materials. The filling process with HA hydrogel is illustrated in Figure 2-15. After aminolysis of PCL membrane for facile immobilization of HA, the PCL membrane was immersed into solution with methacrylated HA, and crosslinked under UV exposure of 365 nm wave length for 30 minutes.

The resultant structure immobilized with HA hydrogel is shown in Figure 2-16. The filled hydrogel in the structure can have also the function of buffer between organs or tissues because of its water-holding property under in-vivo situation.

Rat peritoneum was selected to investigate the tissue anti-adhesion potential of HA-filled PCL membrane because the peritoneum is the one of most frequently occurring tissue adhesion sites after surgical treatment. For this, the membrane was implanted between cecum and peritoneum with wall defects of the rat. The other rat was received no membrane between them. Sprague-Dawley rats weighing 200-300 g were used in this experiment. The animals were cared according to the Korean Food and Drug Administration guidelines for the care. Surgery was performed under general anesthesia (an intramuscular injection of ketamine hydrochloride and xylazine hydrochloride). The rats were sacrificed after 7 days postsurgery. As shown in Figure 2-17, the application of the membrane to the defects showed less adhesion than that of no treatment. From this experimental result, the developed membrane may be a good candidate as a tissue adhesion as a tissue adhesion barrier membrane owing to its efficient tissue anti-adhesion potential as well as the flexibility and biodegradability.

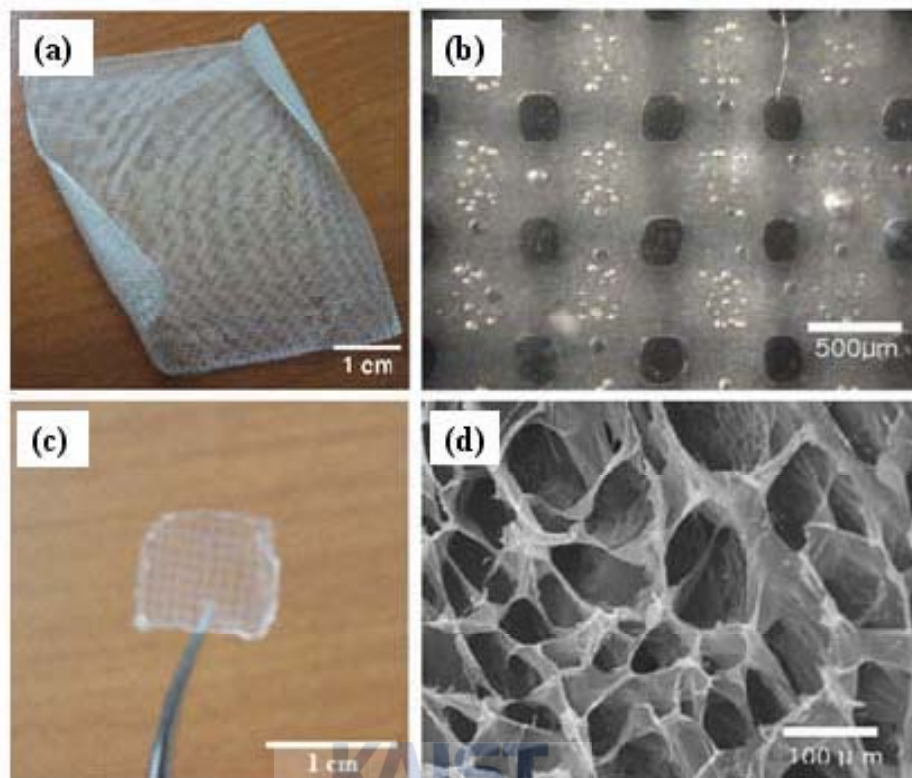


Figure 2-16. (a) Porous PCL membrane. (b) PCL membrane coated by hydrogel. (c) A part of anti-adhesion membrane. (d) SEM image of the surface of hydrogel coating PCL membrane dried.

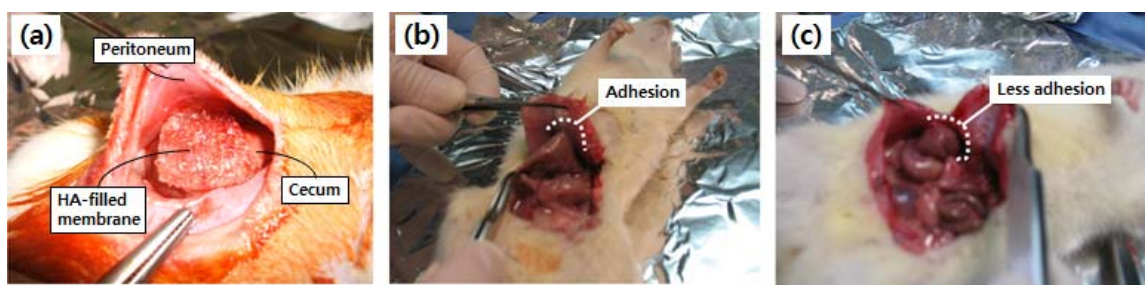


Figure 2-17. Anti-adhesion test; (a) abdominal operation of experimental rat and insertion of the HA-filled membrane, results of in vivo tests (b) with no treatment and (c) with the anti-adhesion membrane.



---

## CHAPTER III

# CONTROLLED ELECTROSPUN NANOFIBERS FOR CONSTITUENTS OF 3D SCAFFOLD

### 3.1 Introductory remarks

Electrospinning is a simple and versatile process that can produce nanofibers in diameters ranging from micrometers to nanometers. This technique uses electrostatic force from a high voltage, where the most typical form of as-spun fibers is a randomly configured non-woven mat [58-60]. As for being biocompatible materials, these nanofibrous mats have a wide range of tissue engineering applications. In order to conduct the electrospinning. The polymer should be in a liquid form dissolved in an organic solvent. Thus the properties of the polymer solution are crucial factors for the electrospinning process and the formation of nanofiber. The solutions should have appropriate conditions of viscosity, electrical properties, surface tension, and rate of solvent evaporation. As well as the properties of polymer solution, other important parameters affect the electrospinning process including the supplied voltage, the feedrate of solution, the collector type, the needle diameter, and the spinning from needle tip to collecting target. Under a favorable combination of the above properties and parameters, the morphology of the electrospun fiber is determined.

Meanwhile, the current interest in the electrospinning methods has been concentrated on other forms of nanofibers, especially uniaxially oriented arrays of nanofibers, in order to expand



their applications.

There have been several proposals on how to fabricate the aligned nanofibers from various angles. There have been two kinds of techniques where well-aligned and highly ordered architectures could be realized. One method has the rotating object used as collector [46-49]. For this method, a cylindrical mandrel [46, 47], a thin disk with a sharp edge [49], and a spaced wire drum[48] were used as the rotating grounded collectors. The nanofibers from the sharp edge of the disk in these methods were reported as providing better alignment than the other methods. However, it was not easy to collect a wide area of aligned nanofiber arrays due to the geometrical limitation of the disk collector. On the other hand, the techniques of the other methods can fabricate the aligned nanofibers by using static and separated conductive electrodes, which is known as the gap method [50, 51, 61, 62]. When the two pieces of parallel electrodes are placed with a gap, the electric field lines adjacent to the electrodes are split into each edge of the electrodes. Thus, electrospun jets are stretched and aligned across the gap by the electrostatic field profile and the repulsive force caused by the residual charge of the nanofibers [50].

The purpose of this chapter was to improve the alignment quality of the electrospinning nanofibers at the base of the gap methods. A simple reconfiguration was used between the separate electrodes. Compared to the planar configuration of the electrodes in the previous gap methods, the suggested collector that was used included an inclined gap determined by the placement of a horizontal and a vertical conductive strip with their mutual height difference. Due to the height difference, a suspension of the electrospun nanofiber occurred in turn at the edge of the lower strip after it occurred at the upper strip. Thus, continuous and well-aligned fiber arrays could be fabricated. It was caused by more space and time for self-alignment as well as by more effective stretching force during the sequential suspension. We herein used the nanofiber alignment technique, i.e., an inclined gap method, employing polycaprolactone (PCL)

---

which has been widely used in the tissue engineering field.

## **3.2 Fundamentals of electrospinning process**

### *3.2.1 Electrospinning apparatus*

In electrospinning, a high direct-current (DC) voltage in the kilovolt range is applied to a polymer solution held in a metal needle. A polymer drop from the needle tip is deformed into a Taylor cone due to the repulsive electrostatic force that overcomes the surface tension of the polymer solution, and a charged jet of the solution is then ejected from the tip of the Taylor cone. As the jet undergoes a stretching process and moves toward a grounded target (collector), it is accompanied by solvent evaporation, which results in nanofiber mats forming on the collector. The setup for electrospinning process is shown in Figure 3-1.

The electrospinning setup basically consists of a syringe needle connected to a high-voltage (up to 30 kV) direct current power supply, a syringe pump, and a grounded collector. The polymer solution is supplied to the needle tip in order to form a hemispherical droplet by the syringe pump. Constant volume flow rate of the polymer solution is precisely controlled by the syringe pump. The syringe is loaded on the syringe pump, and is led to the needle through PE tubing line. The separation between the needle and the syringe (with syringe pump) allow control of needle position. Thus, the needle module including needle and needle adapter can be placed at various positions from the target collector.

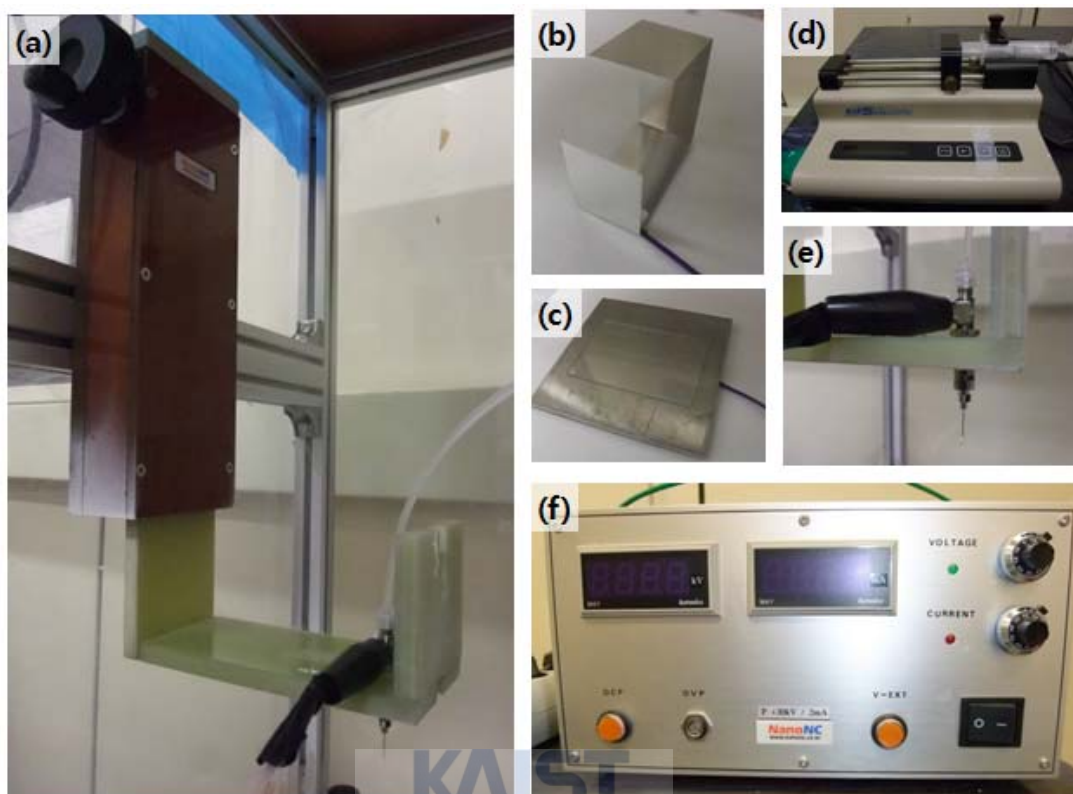


Figure 3-1. Apparatus of electrospinning process. (a) Vertical controller (distance from needle to collector), (b) collector for nanofiber alignment, (c) typical collector (aluminum plate), (d) microsyringe pump, (e) metal needle, (f) high voltage (DC) power supply

The high voltage electrode is used to conduct the charge to the polymer solution, and is connected to the needle. The high voltage is generated from the DC voltage power supply (0-30 kV). Collector electrodes come in many shapes, sizes, and geometries but are commonly some form of flat metallic sheet for randomly configured nanofiber mats. For aligned nanofibers, the other form of electrode configuration can be designed as following chapter. The electrode is connected to ground, hence carrying the opposite charge to the high voltage electrode. The ranges for the experimental operating parameters are shown in Table 3-1.

---

<b>Vertical controller (distance from substrate)</b>	<b>50 ~ 300 mm</b>
<b>Collector for NF alignment</b>	<b>Aluminum sheet (0.2t)</b>
<b>Typical collector</b>	<b>Aluminum plate</b>
<b>Syringe pump</b>	<b>syringe size : 10 <math>\mu\text{l}</math>~60ml flow rate : 0.1 <math>\mu\text{l}/\text{h}</math>~426 ml/h</b>
<b>Metal needle (inner diameter)</b>	<b>0.18 ~ 2.27 mm</b>
<b>Power supply (applied voltage)</b>	<b>0 ~ 30 kV</b>

Table 3-1. Specifications of electrospinning apparatus.

### *3.2.2 Polymer solution parameters*

The properties of the polymer solution have the most significant influence in the electrospinning process and the resultant fiber morphology. The process parameters as well as solution property for the electrospun nanofiber are shown in Figure 3-2.

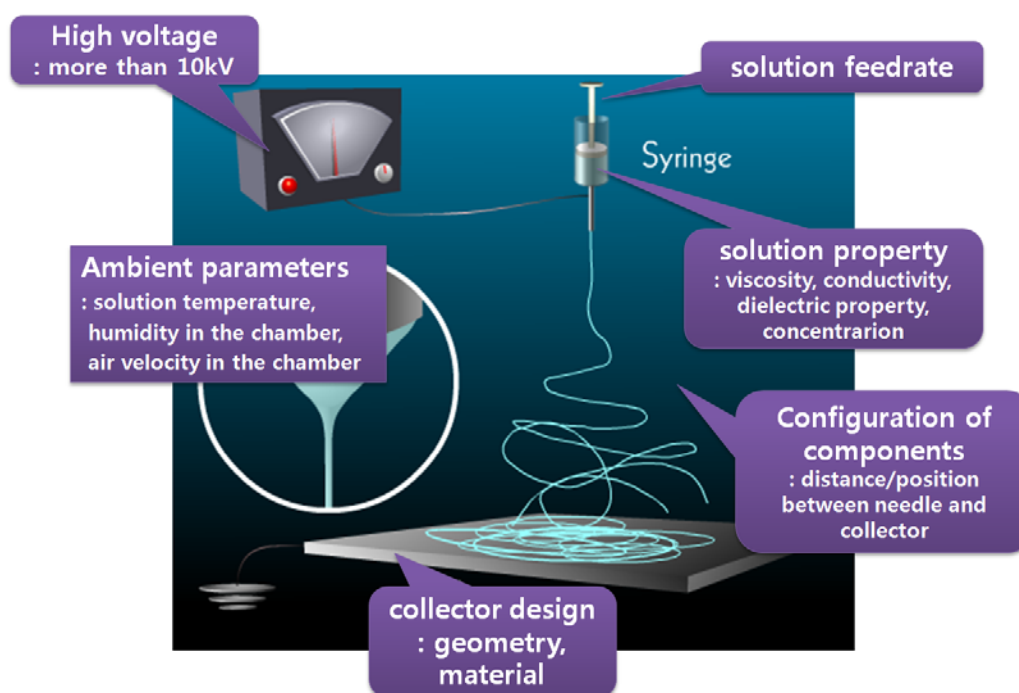


Figure 3-2. Process parameters of typical electrospinning.

One of the conditions necessary for electrospinning to occur where fibers are formed is that the solution must consists of polymer of sufficient molecular weight and the solution must be of sufficient viscosity. Under electrostatic field generated between needle and collector, as-spun jets are stretched as they travel from the needle to the collector. If they don't have the solution properties of sufficient molecular weight and viscosity, the electrically driven jets are broken up rather than maintaining a continuous solution jet during the stretching. Thus, at a lower viscosity, it is common to obtain beads or bumpy fibers on the collector. Table 3-2 shows the effects of spinning conditions on the formation of bead or uniform fiber in several cases of synthetic polymers [63].

Polymer	Molecular Weight	Solvent	Condition of Polymer concentration	Other spinning parameters
Poly( $\epsilon$ -caprolactone), PCL	80,000	Dichloromethane(MC)/ Dimethylformamide(DMF)	Uniform fibers : 13 wt% Beaded fibers : 10 wt%	-
Poly(ethylene oxide), PEO	900,000	Water	Uniform fibers : 3.8 – 4.3 wt% Beaded fibers : 1 - 3 wt%	Voltage : 15 kV Distance : 21.5 cm
Poly(D,L-lactic acid), PDLA	-	Dimethylformamide(DMF)	Uniform fibers : 35 wt% Beaded fibers : 20 - 30 wt%	Voltage : 20 kV Distance : 15 cm Feed Rate : 1.2 ml/h
Poly(vinyl chloride), PVC	-	THF/DMF (50/50)	Uniform fibers : 15 wt% Beaded fibers : 10 - 13 wt%	Voltage : 15 kV Distance : 10 cm
Polystyrene, PS	140,000	THF/DMF (50/50)	Uniform fibers : 15 wt% Beaded fibers : 7 - 13 wt%	Voltage : 15 kV Distance : 12 cm

Table 3-2. The condition of polymer concentration between uniform and beaded nanofibers [63].

As mentioned above, nanofiber formation is based on stretching of the solution caused by repulsion of the charges at its surface. Thus the conductivity of the polymer solution is crucial factor of the electrospinning process. The increase of solution conductivity allows more charges to be carried onto the solution jets. As each solvent has a specific solubility and conductivity for different polymers of electrospinning materials, optimal combination of the solvents is necessary. Table 3-3 shows the conductivity of some solvents commonly used in electrospinning [63].

Solvent	Conductivity (mS/m)
1,2-Dichloroethane	0.034
Acetone	0.0202
Butanol	0.0036
Dichloromethane/ Dimethylformamide (40/60)	0.505
Dichloromethane/ Dimethylformamide (75/25)	0.273
Dimethylformamide	1.090
Distilled water	0.447
Ethanol	0.0554
Methanol	0.1207

Table 3-3. Electrical conductivity of solvents [63].

If a solvent of a higher electrical conductivity is added to polymer solution, the electrospinnability of the solution can be improved. In the case of PCL solution, when dimethylformamide (DMF) is added to the PCL solution dissolved in methylenechloride (MC), the problem of bead or bumpy fiber formation can be reduced. However, the solubility and volatility of solvent should be considered together. As low solubility or volatility can bring about the beads even though high conductivity, the adjustment of the ratio of solvent mixture is necessary. As is widely used, DMF addition of 20 to 30 % of total solvent volume is optimum value for PCL nanofiber formation [64]. The ratio of MC/DMF (80/20) is determined and used identically in this

---

research.

### *3.2.3 Processing conditions*

The aforementioned solution parameters influence the morphology of electrospun fiber in combination with the other process parameters, such as applied voltage and spinning distance from needle to collecting target.

A principle factor in electrospinning process is the application of a high voltage to the solution. Typically, the high voltage of more than 6 kV can induce the formation of Taylor cone from polymer solution drop, and initiates the electrospinning process [65]. After formation of the jet from Taylor cone, the columbic repulsive force in the jet will then stretch the viscoelastic solution. Generally, if the applied voltage is higher, the greater amount of charges included in the jet cause the fiber formation to accelerate faster and more volume of solution is drawn from the solution drop fed through the needle. While this, the insufficient charges caused by the application of low voltage could have a tendency of the bead formation in the electrospinning process. Thus, the effective range of applied voltage in each case of the polymer solution should be determined before conducting the electrospinning process.

In this research, the electrospinning was performed using not only homogeneous PCL material but also PCL/collagen mixture. As is well known, the natural polymer such as collagen can provide the improved bio-functional properties of cell-scaffold interaction [66]. For the electrospinning of PCL/collagen mixture, polycaprolactone (PCL, average, MW ca. 80,000) and 1,1,1,3,3,3-hexafluoro-2-propanol (HFIP, 99+%) were supplied by Aldrich (Milwaukee, WI), and Collagen type I (from calf skin) was purchased from Sigma (St. Louis, MO). The polymer solution for the electrospinning was prepared by dissolving PCL/collagen (6/4 weight ratio) blend in HFIP at a concentration of 10 wt%. With this polymer solution, the effective voltage range for the



spinning of beadless fiber is determined varying the applied voltage. As shown in Figure 3-3, when the applied voltage was increased, the problem of the bead formation could be reduced. 22-gauge needle on the syringe pump at an infusion speed of 10  $\mu\text{m}/\text{min}$  was used for the experiment, and the grounded collector was placed 10 cm from the needle tip.

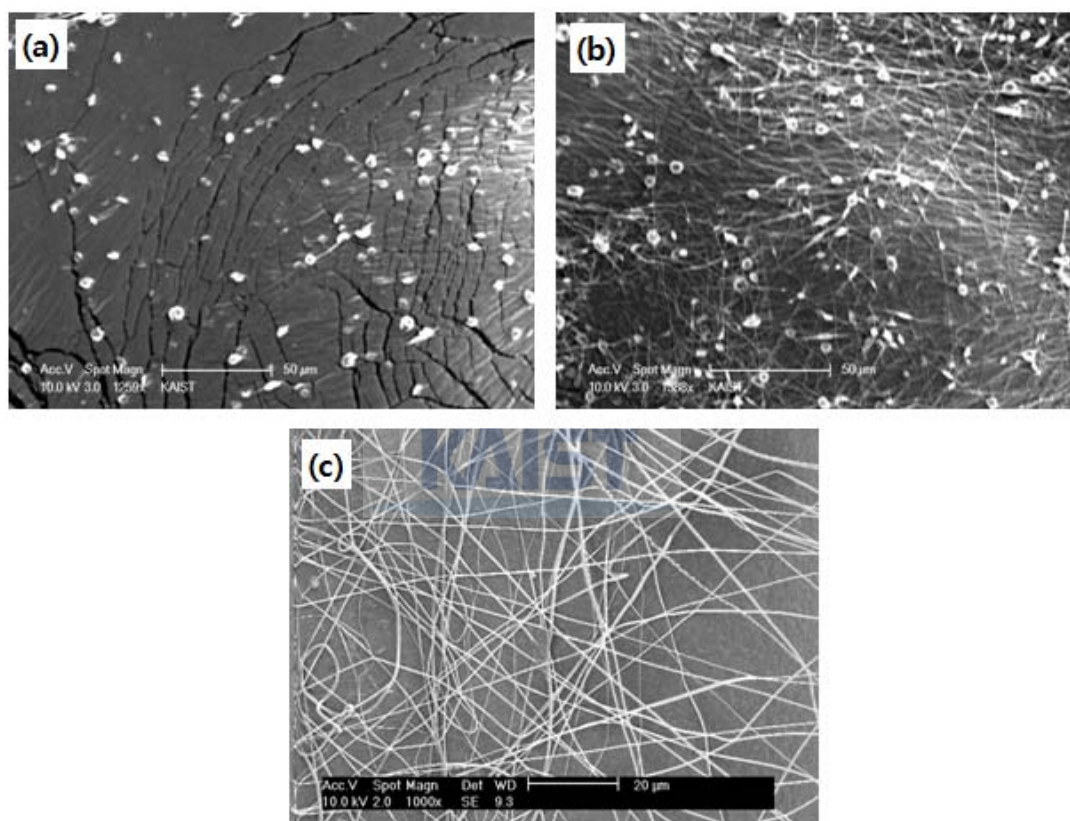


Figure 3-3. Effective voltage range for nanofiber formation; (a) bead formation at less than 9 kV, (b) fibers with beads at 9 to 16 kV, (c) fibrous mats at more than 16 kV.

The flight time of as-spun jet until landing onto collector is also a significant factor in the electrospinning process. Varying the distance from the needle tip to the collector has a direct correlation with the flight time. For the formation of independent fibers, the flight of jet should

---

be sustained for a period of time to evaporate most of the solvents in the jet solution. When the spinning distance is reduced, the jets have a shorter time to travel before it reaches the collecting target. Furthermore, the shorter spinning distance causes the increase of electric field strength, which accelerates the jets onto the collector. As a result, the excess of residual solvents in the solution jets causes the fibers to merge where they contact each other. Figure 3-4 (a) shows the interconnected network from the merged fibers at shorter spinning distance, while as-spun fibers are individually deposited even though they are in proximity [Figure 3-4 (b)].

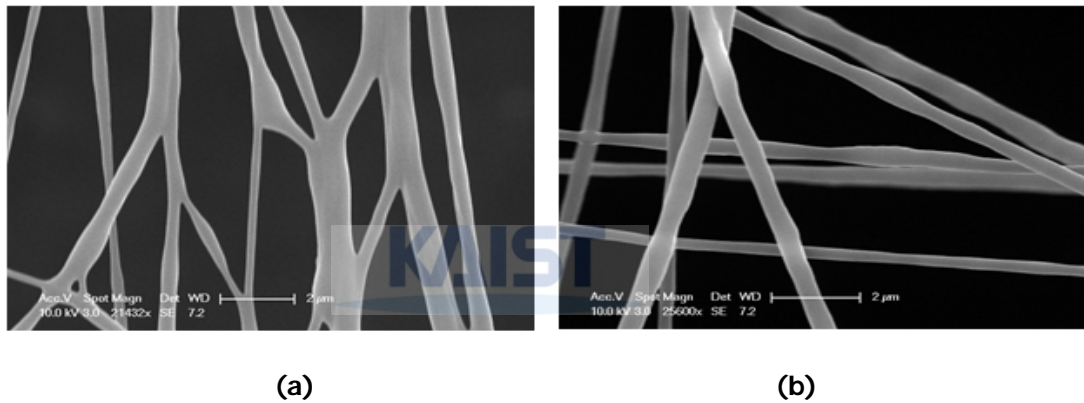


Figure 3-4. The electrospun nanofibers at spinning distance of (a) 80 mm and (b) 160 mm.

As well as the applied voltage and the spinning distance, several process parameters affect the electrospinning process. For a given voltage and distance, the feedrate of material solution and the diameter of needle should be adjusted in combination. If they are not in favorable condition, Taylor cone from the needle is in unstable state during the process of jet formation.

On the other hand, ambient parameters such as surrounding temperature and humidity also have an effect on the electrospun fiber morphology. Since the humidity and temperature of the environment may determine the rate of evaporation of the solvent in the solution jet, the other

process parameters such as the applied voltage and the spinning distance are needed to be changed considering the ambient conditions. For example at a higher humidity, the longer spinning distance is recommended for the beadless fiber formation, because the volatile solvent in the solution jet may dry more slowly.

### 3.3 Principles of electrospinning for aligned nanofibers

The most fundamental way of getting uniaxially oriented fibers is through the use of a rotating collector. It is a simple and mechanical method of winding the electrospun fibers around the circumference of the rotating object. During the fibers are formed from the as-spun jets, the collector is rotated at a very high speed up to thousands of rpm. One possible geometry of the collector is cylindrical mandrel (Figure 3-5). Using the mandrel as the rotating collector, it was successful to obtain the aligned PGA and type I collagen nanofibers at the rotating speed of 1000 rpm and 4500 rpm, respectively [46, 47]. Although the rotating mandrel technique provides obvious alignment of the fibers, only partial alignment is achieved.

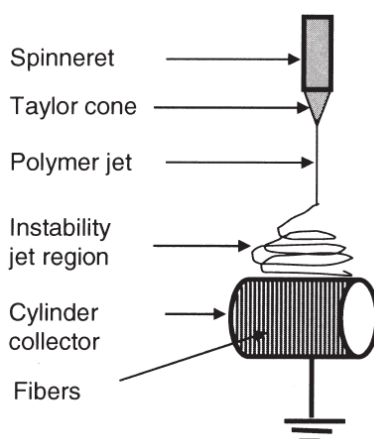


Figure 3-5. A rotating cylinder collector to obtain aligned nanofibers [67].

---

Instead of rotating mandrel, a thin disk with sharp edge can be used as the rotating collector [49]. The electric field lines are converged onto the sharp edge so that an inverted envelope cone of the traveling jets formed and most of the as-spun fibers are attached to the edge (Figure 3-6). However, this method has a disadvantage in that the electrospun nanofibers can only be obtained on a narrow region due to the edge geometry. It may be a problem for applications which need large area of the aligned fiber mats.

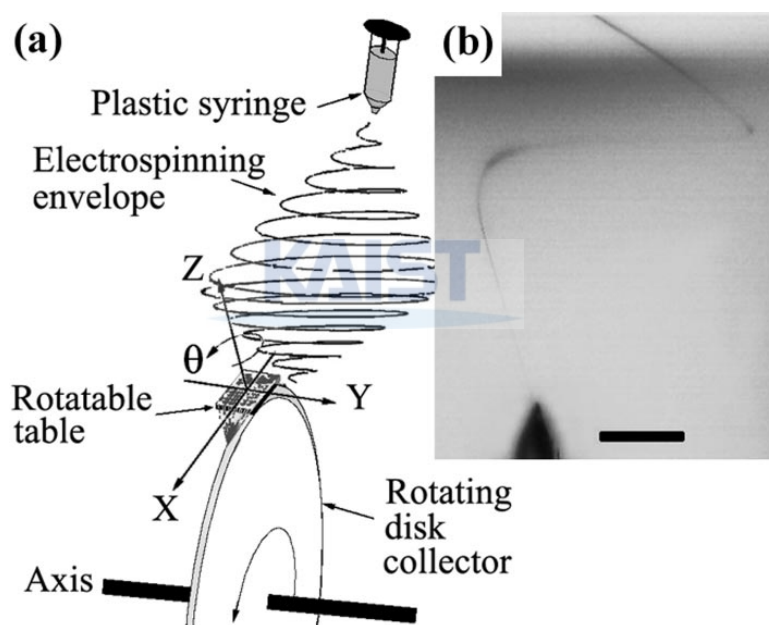


Figure 3-6. (a) Schematic illustration of the electrospinning process using rotating disk collector. Double-cone envelope of the jet is shown. (b) a flash photograph of a nanofiber that is attracted to the edge of the disk [68].

Besides using the rotating objects alone, it is possible to control the path of the electrospun jet by manipulating the electric field generated from auxiliary electrodes [69]. When an auxiliary electrode is placed next to the rotating mandrel along the direction of the jet progress, the fibers

can be deposited on the mandrel as they accelerate toward the electrode. This way allows the fiber alignment even at the lower rotation speed of less than 1000 rpm. Uses of parallel arrays of strips and knife-edged bars were tried as the auxiliary electrode. However, the resulting alignment of this method does not vary much from the other mechanically dynamic methods such as rotating mandrel and disk.

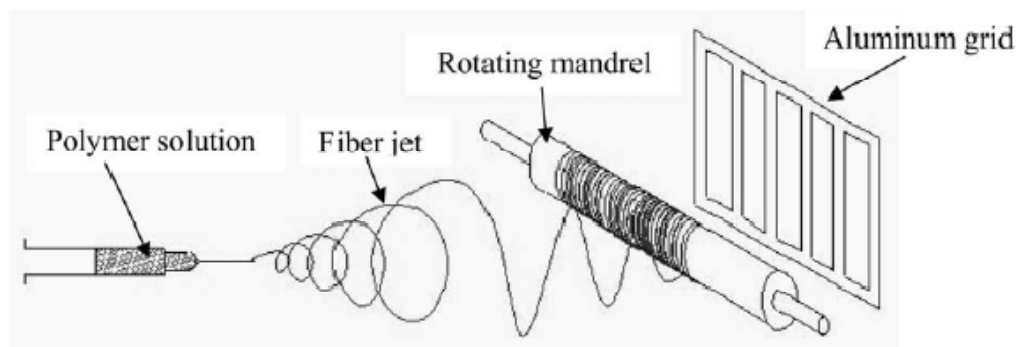


Figure 3-7. Use of parallel strips as auxiliary electrode to assist in the fiber alignment [69].

The above methods usually involve the use of mechanically rotating objects. In the following method, namely 'gap method', the fiber alignment can be achieved without rotating collector. As shown in Figure 3-8, when two conductive electrodes are placed in parallel with each other, the electric field lines were split into two fractions toward both edges of the collectors. Since the electrospun jets tend to move along the distribution of the electrostatic field lines, the jets are attracted towards the collector edge and stretched across the gap. This induces the fiber alignment across the gap between the separate collectors. Mutual repulsion caused by residual charges of the deposited fibers is an additional factor for the fiber alignment. This enhances the parallel alignment of the fibers. However, the repulsion also means that the quantity of the collected fibers is limited. Thus, this method is not suitable to realize the thick layer of the electrospun fiber mat.

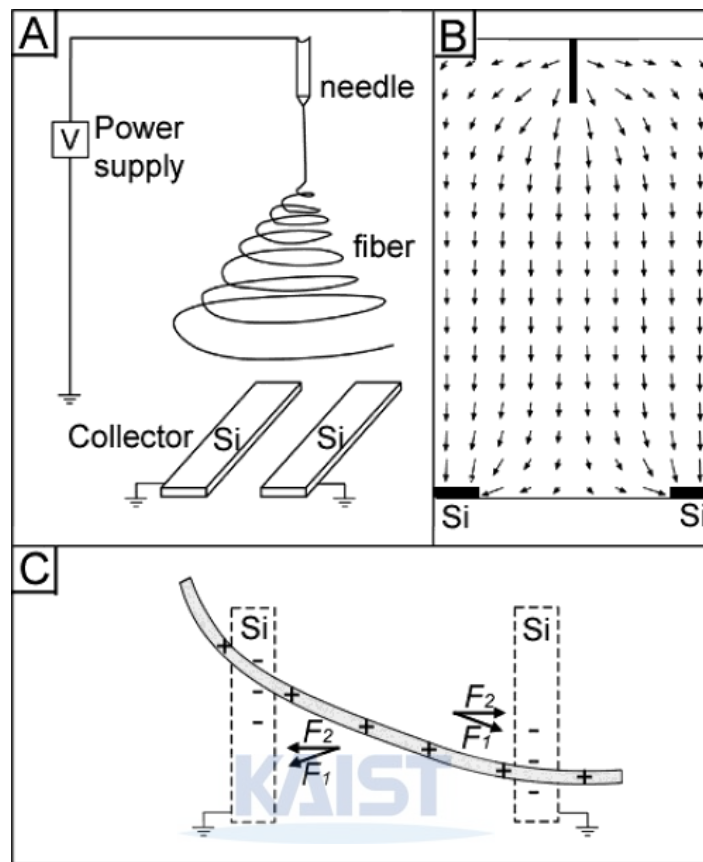


Figure 3-8. (a) Schematic illustration of the electrospinning with two parallel collector. (b) Distribution of electric field strength vectors between the needle and the collectors. (c) Electrostatic force exerted on the charged nanofiber [50].

### 3.4 Inclined gap method

#### 3.4.1 Electrospinning setup and collector design

In electrospinning, the electrically charged jets that erupt from a Taylor cone undergo stretching and travel toward objects with lower electric potential. As the jet moves along the electric field lines, it is accompanied by solvent evaporation, which results in the formation of

nanofibers on the target object. During the process of jet movement and stretching, the charged jets are influenced by the electrostatic field profile spread between the nozzle tip and the collecting target. When two conductive objects are placed at the collecting position in a parallel configuration, the electric field lines divided into two fractions can make the electrospun fibers orient themselves across the gap between the collectors [50].

In this research, a rearrangement of two conductive strips was created by employing an asymmetric configuration that included vertical and horizontal placements of the strips. Figure 3-9(a) shows a schematic of the suggested electrospinning setup. The collector consisted of two thin aluminum strips (0.2 mm thickness). As one was fixed horizontally at the upper position and the other was anchored vertically at the lower position, there was an inclined gap between the two strips. The inclined angle and the gap width were determined to be  $45^\circ$  and 30 mm, respectively.

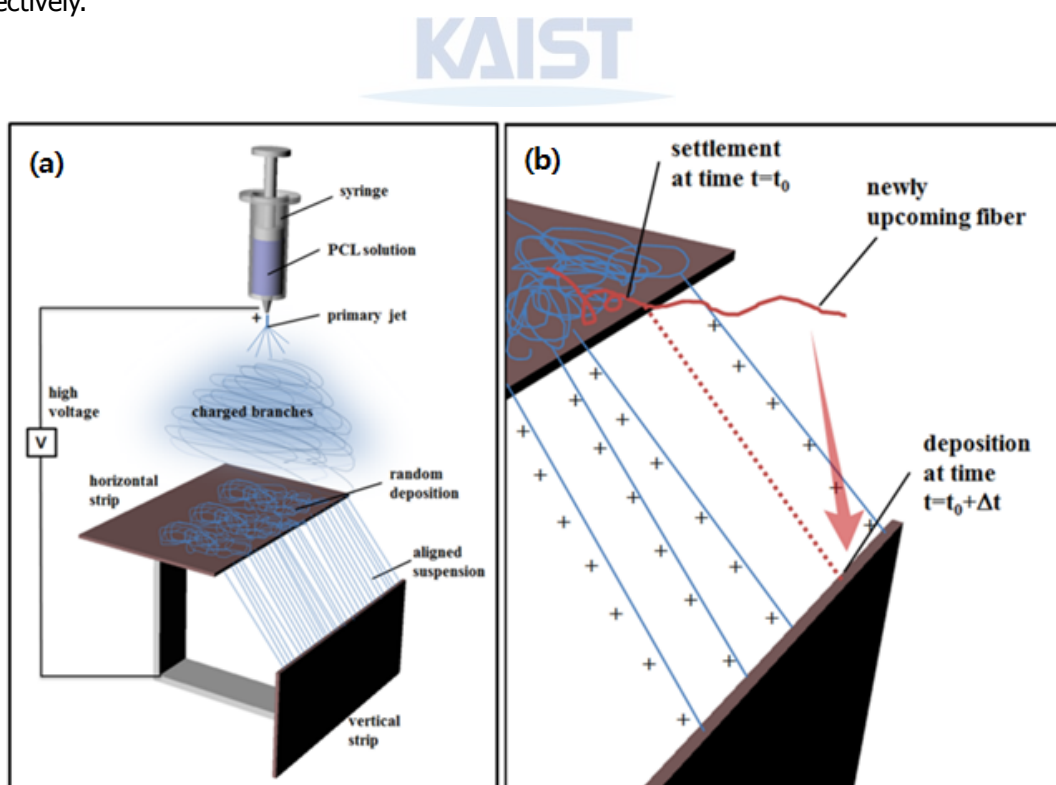


Figure 3-9. Schematic diagram of the used electrospinning setup for the proposed inclined

---

gap method; (a) the setup for electrospinning, and (b) the nanofiber suspended sequentially across the inclined gap.

A flat-tipped needle (0.29 mm inner diameter, stainless steel) was placed upwards at a distance from the horizontal strip (80 and 160 mm) and connected to a power supply in order to apply high voltage from 6 to 20 kV between the needle and the collector. A 10 ml syringe with the needle was equipped on a micro infusion, and the prepared PCL solutions were extruded through the needle at a constant rate of 0.6 ml/h. Uniaxially aligned nanofibers were suspended across both edges of the upper and lower strip and transferred onto a surface of slide glass (76 × 26 mm<sup>2</sup>, 1 mm thickness). This process for collecting and transferring in sequence was repeated several times. As a result, quantitatively controlled densities of the nanofiber array were obtained depending on the number of transfers.

KAIST

#### *3.4.2 Effect of inclined gap on fiber suspension*

It has been known that the influences of the electric field on the spun fiber morphology and collecting construction are extremely important[70-72]. As has been investigated previously[50, 51, 61, 62], separating the conducting collector by void or insulating gap allows for the self-alignment of fibers and stretching of spun jets due to the field line split towards both edges of the collectors. However, what is different here from the previous gap methods is the introduction of an inclined void gap between the two strips, where one is placed horizontally and the other is erected vertically at a lower location than the horizontal one.



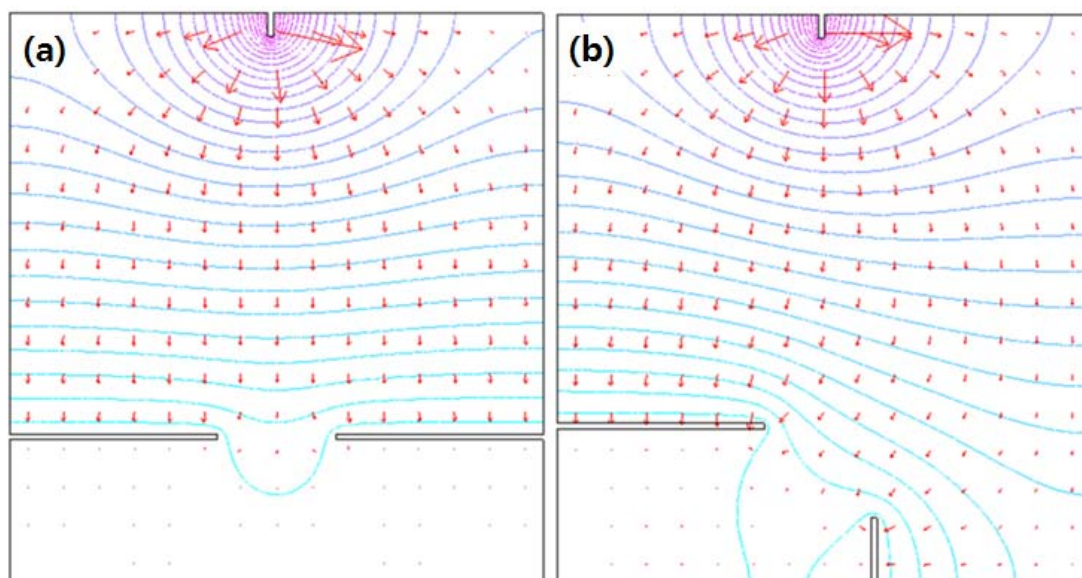


Figure 3-10. Calculated equipotential lines and electric field strength vectors between the needle and the collectors; (a) symmetrical distribution of the electrostatic field in the region around the collectors with planar configuration. (b) asymmetrical distribution of the electrostatic field due to the modified configuration of the collectors.

In order to verify the effect of such an asymmetrical configuration of the strips, the distribution and shape of the electrostatic field among the needle and the collectors were simulated by using the analysis software FEMLAB 3.0. Figure 3-10(a) and Figure 3-10(b) show the calculated results, including the equipotential lines and electric field strength vectors in the region around the needle and the collector. As shown in Figure 3-10(a), when the collectors were disposed in a planar way, the lines and vectors are symmetrically distributed along a center-line from the needle tip to the middle point of the gap. In this case, the charged as-spun fibers affected by the split electrostatic force towards each edge of the collector would settle almost simultaneously at both edges of the collector. While in the planar configuration of the collectors, one of the collectors was positioned endways lower than the other one, as shown in

---

Figure 3-10(b). As we get closer to the vicinity of the collectors in this case, the shape of the equipotential line becomes asymmetric for the center-line. Additionally, the vector arrows around the horizontal collector are formed stronger than those near the vertical one. Once the charged fiber has moved through the distributed vector field, one spot of the fiber will contact and be deposited onto the edge of the horizontal collector. After the prior settlement, the fiber is stretched out towards the edge of the vertically erected collector and a posterior deposition subsequently occurs in order to attain the final suspension across the gap [Figure 3-9(b)]. During the process of the charged fiber suspension, the electrostatic repulsion acting between the fibers can promote parallel alignment. When the configuration of the collectors has a height difference, such as that shown in Figure 3-9(b) and 3-10(b), it can provide the suspension of the aforementioned time difference, where the alignment is expected to be further enhanced due to more time and space needed for the alignment effect by the mutual repulsion between the fibers. Figure 3-11 shows the experimental results on the difference between the planar gap and the inclined gap. Both the straightness of the each fiber and the regularity of the fiber distribution in the case of the inclined gap [Figure 3-11(c) and (d)] appeared to be in better conditions than the planar case [Figure 3-11(a) and (b)].

From these results, it could be considered that the more stretch and repulsion which were caused by the sequential settlement at the edges of the inclined gap exerted a favorable influence upon the fiber alignment and distribution. The electrospinning conditions included the applied voltage of 11 kV, solution concentration of 18 wt%, spinning distance of 160 mm, and spinning time of 40 sec. The enlarged images of the fiber arrays were observed by an optical microscope (i-Camscope, Sometech Vision).

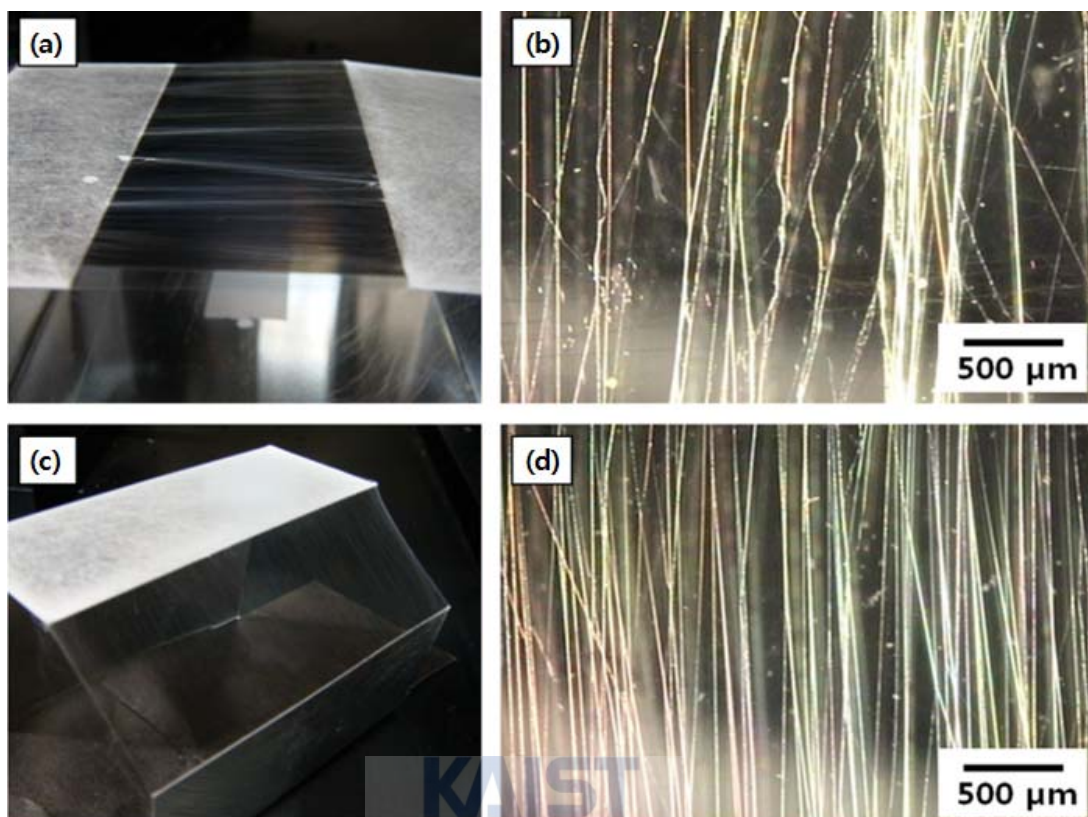


Figure 3-11. Photographs of the collectors with the suspended nanofibers on (a) the planar gap, and (c) the inclined gap. Optical micrographs of parts of the nanofiber arrays on (b) the planar gap, and (d) the inclined gap.

Figure 3-12 compares the accumulated fibers on the surface of the horizontal collector and the suspended fibers across the inclined gap. As shown in Figure 3-12(a), the fibers deposited on the upper (horizontal) collector were randomly oriented like typical electrospun fibers. In contrast, the fibers anchored at both of the edges were well aligned in a direction across the gap [Figure 3-12(b)]. It is notable that the suspended nanofiber had a thinner diameter range (500~700 nm) than that of the directly deposited nanofiber (1~6 μm). Such a drastic difference in the fiber diameter is attributed to the aforementioned stretch effect by the action of the electrostatic forces, which is the main factor for this fiber alignment technique.

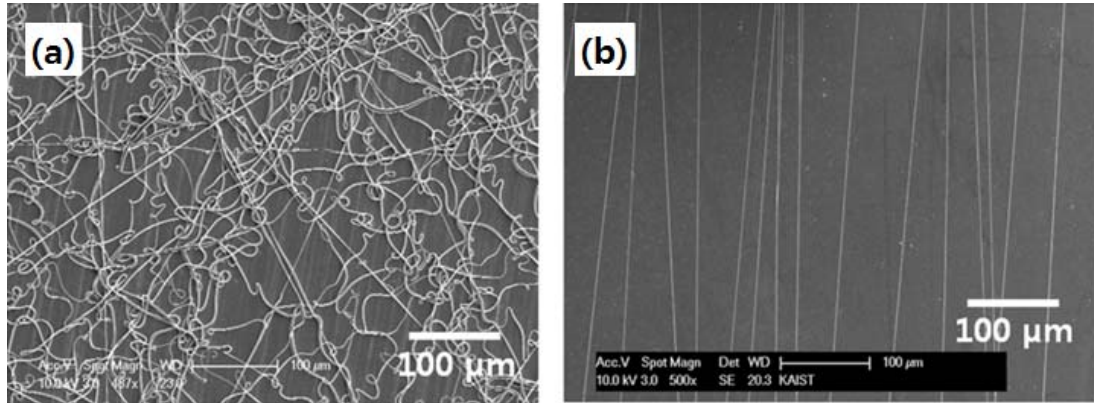


Figure 3-12. SEM images of a) the randomly deposited nanofibers on the upper strip, and b) the uniaxially aligned nanofibers between the upper and lower strip edges.

### 3.5 Requirements for stable collection

Throughout the electrospinning technique to obtain the aligned nanofiber arrays along the inclined gap, one of the crucial requirements was the successful suspension of the fibers onto the collector gap. More specifically, the solidity of the spun jet became important when it reached the collector for the suspension. As the spun jet underwent the stretching process and moved toward the collector, it was accompanied by solvent evaporation so that the liquid jet solidified. Unless the sufficient solidification has progressed, the resultant nanofiber from the jet tends to be collapsed during the suspension process because such liquid-like fiber is not sufficiently strong enough to withstand the electrostatic stretching force between the gap and the weight itself, as well as repulsive interactions with the upcoming and neighboring fibers. Considering the experimental parameters that affect the fiber condition in the typical electrospinning process, two factors for the successful suspension can be pointed out. First, the

initial jet from the Taylor cone should be a relatively high concentration so that the spun fibers can hang onto the collector in a solid-like state. This is apparently related with the concentration of the material solution. The spinning distance, as well as the material parameter, from needle to collector should also be taken into account. In other words, the needle needs to be kept at a specific distance from the collector so that solvent evaporation sufficiently occurs. While a suitable case in Figure 3-13(a), Figure 3-13(b) and (c) show a worse case of less or unstable suspension due to the conditions of the low solution concentration and the short spinning distance, respectively.

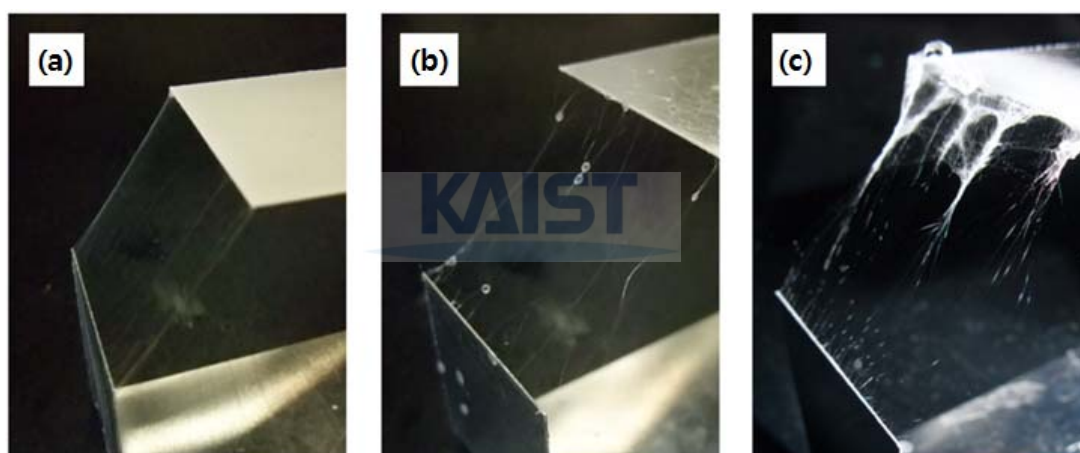


Figure 3-13. Photographs of (a) the successful suspension and the inappropriate suspensions due to (b) the low solution concentration (10 wt%, 160 mm distance) and (c) the short spinning distance (50 mm, 18 wt% concentration).

In order to figure out appropriate parameters for the successful suspension, some spinning experiments were carried out under the several conditions shown in Table 3-4. As shown in Table 3-4, there was no or less suspension in the conditions of 10 wt% solution concentration, regardless of the spinning distance. This was attributed to insufficient solidification at the

moment of suspension onto the collector, as discussed above. On the other hand, too high level of a concentration, such as the case of 22 wt%, makes the Taylor cone unable to form and the spun jets to function, even at a higher voltage. The condition of 18 wt% provided well-suspended and stable nanofibers in all the cases of short (80 mm) and long (160 mm) spinning distances. Furthermore, this condition, especially in the long spinning distance (160 mm), had a relatively wider range of applied voltage where stable formation and suspension of the nanofibers were more likely to occur than the lower concentration. Thus, from these results, subsequent studies used the conditions of 18 wt% concentration and 160 mm spinning distance.

<b>Solution concentration (wt%)</b>	<b>Spinning distance (mm)</b>	<b>Suspension quality</b>	<b>Valid range of voltage (kV)</b>
10	80	△	-
10	160	△	-
14	80	△	-
14	160	○	13 ~ 15
18	80	○	10 ~ 14
18	160	○	8 ~ 18
22	80	×	-
22	160	×	-

△ : less or no suspension    ○ : proper suspension    × : no spinning

Table 3-4. Electrospinning conditions for the successful suspension.





---

## CHAPTER IV

# CHARACTERIZATION OF ELECTROSPUN NANOFIBERS AND EFFECTS OF CELL GUIDANCE

### 4.1 Introductory remarks

The importance of nanostructured topography in view of cell biology has been recognized as one of the key factors in tissue engineering applications. Nano- or micro-architectures that can mimic natural extracellular matrix (ECM) environments have been employed in fabrication of functionalized scaffolds to enhance cellular responses, such as adhesion, migration, proliferation, and locomotion [73-75]. The ECM-like structure, a complex structural network with various fibrillar constituents, has been simulated by a wide variety of fabrication techniques which include MEMs-based lithographic methods, imprinting methods, and electrospinning methods [76, 77].

The electrospinning process, in particular, has advantages for fabricating cyto-compatible scaffolds thanks to its high efficiency and simplicity in producing submicron to nanometer scale fibers from a wide range of biomaterials. When a high electric potential is applied to the pendant drop of a polymer solution, the drop gets deformed into a cone shape, which is known as a Taylor cone. As a charged jet of the polymer solution is launched from the tip of the cone and elongated into thinner fibers, it gradually solidifies forming a nanofibrous mesh on the grounded collector. In typical electrospinning process, the nanofibers from the elongated jet are randomly



deposited on the collector due to jet bending and whipping caused by Columbic interaction between the jets [60]. Although these randomly assembled non-woven nanofiber meshes have a wide range of bio-applications [78-82], the recent interest in the electrospun nanofibers has been focused on ordered forms of the fibers, especially uniaxially aligned fiber arrays in light of tissue engineering applications for anisotropic tissues such as tendons and muscles. Fiber configuration with uniaxial orientation can be dictated by collector geometry, which has been proposed in various ways including using a rotating cylinder, a disk with a sharp edge, a spaced wire drum, and parallel electrodes as aforementioned.

The potential of applying these alignment techniques to scaffold fabrication is significant in that it can provide a defined architecture to guide cellular behavior as well as nanoscaled dimensions for the biomimetic ECM for a wide range of cell lines such as fibroblasts, neuron cells, muscle cells, etc [83-88]. Many studies on the guidance effect have been conducted using lithographic techniques based on the MEMS process to realize precise construction of ridge/groove patterns for cell guidance [86, 88]. However, in terms of utilization of bio-compatible materials for scaffold fabrication and the fabrication itself, the electrospun nanofiber array is far more advantageous than MEMS based processes. Based on the elctrospinning technique, some efforts have been made to apply the fiber alignment technique with a rotating disk collector [84]. Yet, due to the geometrical limitation of the disk edge, the employed technique makes it difficult to collect a wide area of fiber arrays.

As mentioned in the previous chapter, the fabrication process of aligned electrospun nanofibers is realized by the proposed inclined gap method, which provided regular distribution and high order alignment of the nanofibers over a relatively wide area. The intrinsic instability of fiber landing in the electrospinning process was mitigated by employing two separate strips that were configured horizontally and vertically with the inclined gap. In this chapter, aligned nanofibrous scaffolds with different densities were prepared by employing multiple transfers of

---

the previously proposed process. Thanks to the favorable feature of void gap with suspended nanofibers, transfers of these fibers onto the other substrate can be easily accomplished. The repetitively overlapping transfer can provide quantitative control of the nanofiber densities in the scaffold in proportion to the number of transfers. Human dermal fibroblasts were cultured for seven days to observe the cell guidance effect and morphological changes on the scaffolds of different densities. Additionally, a bare PDMS substrate and a randomly deposited nanofiber mesh were tested to compare with the specimens of aligned nanofibers.

## 4.2 Characteristics of fiber array

### *4.2.1 Property of fiber alignment*

The resultant samples that were transferred with electrospun nanofibers were photographed using a scanning electron microscope (SEM; JSM-6300, JEOL) at an accelerated voltage of 10 kV after gold-sputtering onto the samples. Several images were captured by using the SEM side by side transversely for measuring the fiber alignment. Bent, looped, and discrete fibers were excluded and only straight fibers were analyzed. The angle distribution of each nanofiber was measured from the SEM images by using ImageTool 3.0 (University of Texas Health Science Center in San Antonio, USA).

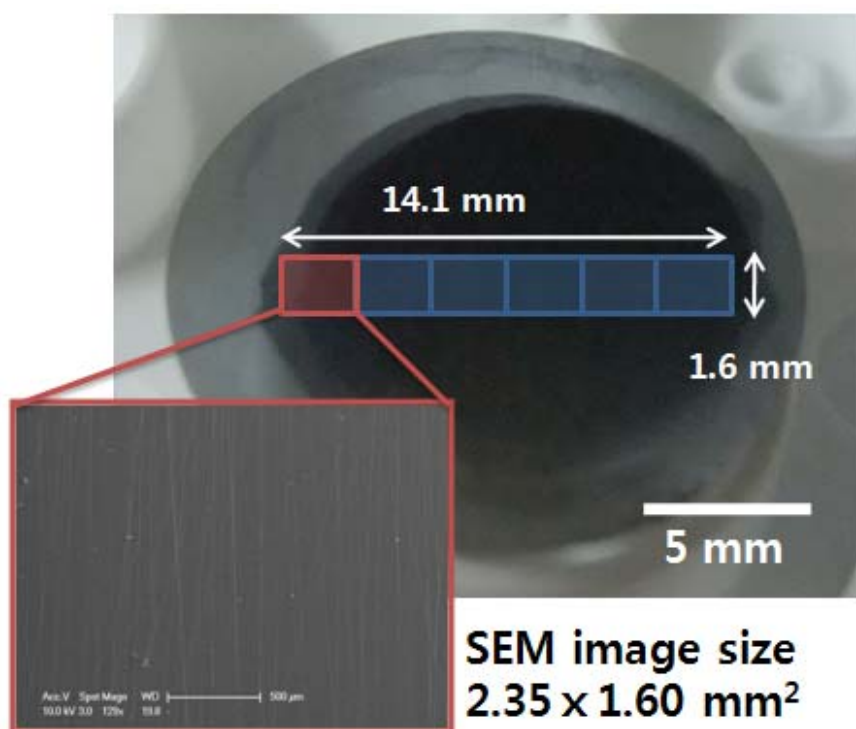


Figure 4-1. SEM image for measurement of nanofiber alignment.

Figure 4-1 gives a SEM image of a sectional region of the specimen on which the suspended fibers were transferred. The employed conditions were as the aforementioned including the solution concentration and the spinning distance. The applied voltage and the spinning time were 11 kV and 30 sec, respectively. Under these conditions, the morphologies of the most suspended fibers were uniformly well-aligned, straight, and continuous, while the broken or bent fibers were scarcely observed. From the serially taken SEM images, we quantified the fiber alignment by employing the angles between the desired direction (perpendicular to the edge lines of two strips) and the longitudinal axes of the fibers. 510 fibers were measured from 6 SEM images over an area of  $14.1 \times 1.60 \text{ mm}^2$ . Figure 4-2 gives the resultant histogram with the angle distribution of the nanofibers. All of the processed fibers were distributed within angles

---

ranging from  $-35^\circ$  to  $25^\circ$ . It was found that more than 85% of the fibers were aligned within  $\pm 10^\circ$  of the preferred direction.

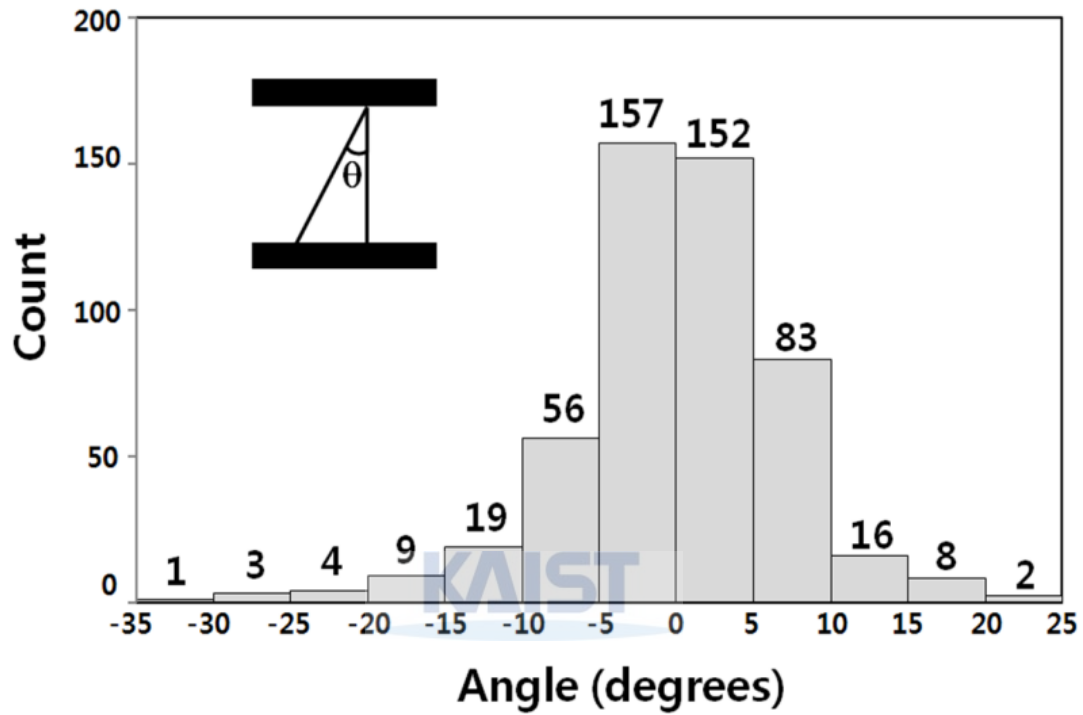


Figure 4-2. Histogram of distribution of the angle between the longitudinal axis of the each fiber and the expected direction.

In order to compare the corresponding results with the previous methods, we employed a parameter used by Liu et al. [62]. In their studies, the parameter which was originally suggested in the research field of fiber composite was adopted to the quantitative analysis of the electrospun nanofibers made by several techniques. According to this description, the fiber orientation parameter was expressed by

$$g_p = \frac{(8\langle \cos^4 \phi \rangle - 3)}{5} \quad (4.1)$$

where

$$\langle \cos^4 \phi \rangle = \int_0^\pi \cos^4 \phi \cdot \Psi(\phi) d\phi \quad (4.2)$$

and the fiber orientation distribution function was defined by the probability of finding a fiber between 0 and  $\pi$ .

$$p(0 \leq \phi < \pi) = \int_0^\pi \Psi(\phi) d\phi = 1 \quad (4.3)$$

where  $\phi$  is an inclined angle of the individual fiber from the desired direction. If all fibers were perfectly oriented uniaxially, the orientation parameter  $g_p$  would be 1. Otherwise, it would be 0 for the random nanofiber distribution. From the way of this description, it was calculated that the  $g_p$  that corresponded to the results of Figure 4-2 was 0.96.

There were two kinds of previous methods for electrospun nanofiber alignment, as stated above. According to an earlier investigation<sup>19</sup>, the orientation parameter  $g_p$  appeared up to about 0.8 in the method for rotating the drum collector. The rotating speed of the collector mainly affected the alignment property as was well known. The examples in the study included the measured parameters along the various linear velocities of the drum surface, such as 0.45 for 4.19 m/s, 0.7 for 8.37 m/s, and 0.8 for 25.12 m/s. Meanwhile, another alignment technique, the gap method, which is a typical case for planar configuration of the electrodes, was mainly affected by the gap size. An increase of gap size improved the alignment quality. Along the description [89], the parameters for experimental results approximately varied from 0.65 to 0.9 in the range of gap size (3 ~ 18 cm).

---

From these alignment techniques, we believe that the produced fiber array by the inclined gap method had a higher value of orientation parameter. This high order orientation (more than 0.95) was similarly found under the other conditions of the applied voltage within the range from 9 kV to 15 kV. Furthermore, defective nanofibers, such as the looped and broken one, were observed much less.

#### *4.2.2 Density of aligned fiber array*

Typically in the electrospinning process, the longer the spinning time, the more increased fibers can be obtained. Therefore, a density of the spun fiber array is mainly dependent on the process time. Figure 4-3 shows several SEM images produced during the different collection times, as well as their corresponding densities and orientation parameters. The density was calculated as the number of nanofibers per horizontal length of 1 mm in the SEM image.

As seen in Figure 4-3, well-aligned fiber formation was found to be present up to 30 sec of spinning time. At a longer collection time of 40 sec and 50 sec, the alignment properties of fiber arrays got worse. The loss in orientation with the denser arrays was possibly due to the reciprocal repulsion between the collected fibers. The presence of charges on the collected fibers tended to keep the spacing between the fibers during the collection on the gap. Compulsory landing onto the prior fiber array within the gap can cause misaligned deposition or direct the spun fibers towards a horizontal collector rather than the gap. In our case, 30 sec of collection time was selected as an optimum condition for the density of the aligned fiber array. After 30 sec, the alignment property was gradually lost, although the amount of fibers was increased. The preferred collection time provided approximately 30 fibers/mm. The value came to roughly 33  $\mu\text{m}$ , which was converted at average spacing between the fibers. Considering the various applications related to the aligned nanofiber mats, this low density could cause limitations if it is

used as a valid structure.

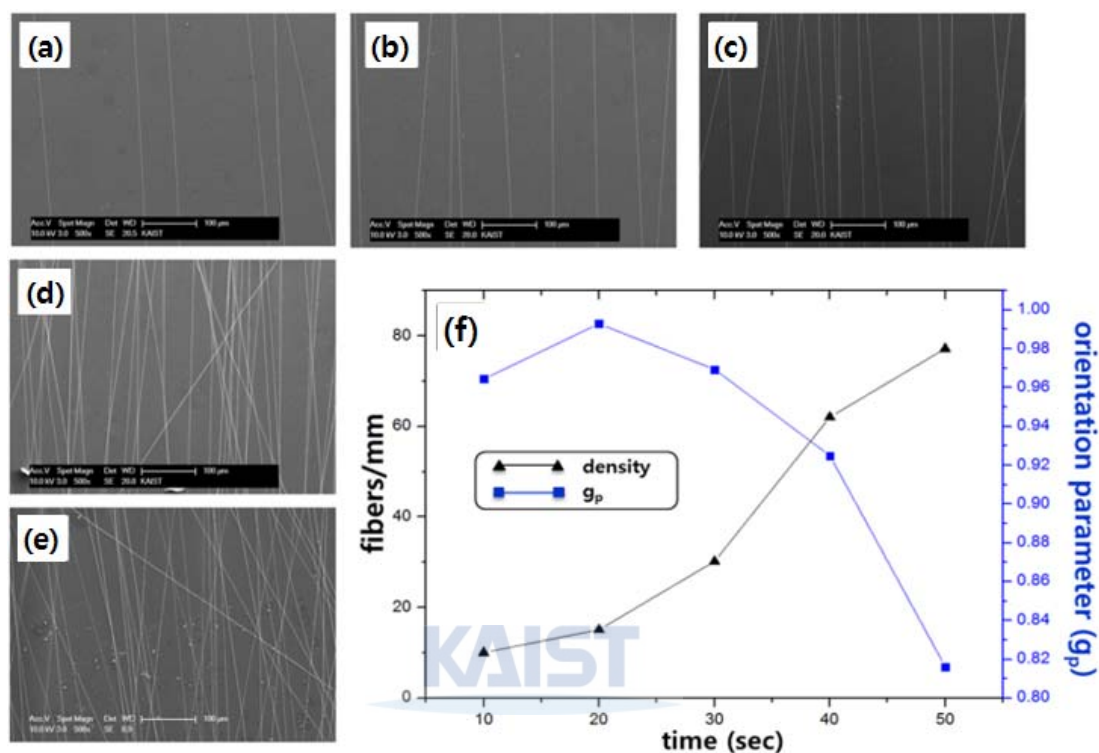


Figure 4-3. (a,b,c,d,e) SEM images of the aligned nanofiber array electrospun during different spinning times: 10, 20, 30, 40, and 50 sec, respectively (the scale bars are all 100 μm). (f) Corresponding orientation parameters and values of densities.

In this research, a higher density of the nanofiber array is accomplished without having the alignment property impaired by employing repetitive transfer. As shown in the previous chapter, the void space within the collector frame facilitated the transfer process. After transferring the firstly collected array of fibers onto a glass substrate, the heap of fibers that remained on the strips was removed. The same procedure producing the aligned electrospun nanofibers on the cleaned collector was repeatedly carried out, and thereafter, they were transferred onto the substrate with the prior fiber array. These repetitive procedures, including collection and transfer,

---

enabled the stacked nanofiber matrix to have a more increased density. The impairment of fiber alignment, as well as destruction between the mutual mats, was not found during the repetitive process (Figure 4-4). As shown in Figure 4-4, the average spacing between the fibers was reduced up to approximately 2  $\mu\text{m}$  when the number of transfers was increased up to 20. From these results shown in Figure 4-4, it can be expected that a quantitative control of the density of the aligned nanofiber matrix is quite practical because the amount of nanofibers for one crop was regularly quantified to some extent and the density of the matrix could be proportional to the multiple transfers.

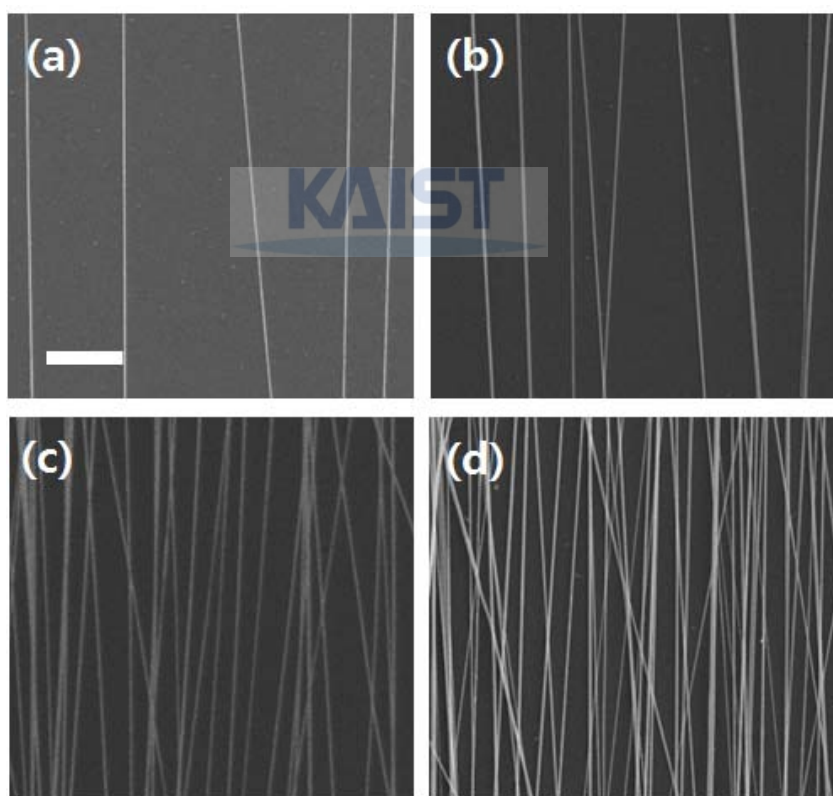


Figure 4-4. SEM images of the nanofiber arrays transferred repetitively; (a) 1 transfer, (b) 3 transfers, (c) 10 transfers, and (d) 20 transfers. The scale bar on (a) is 20  $\mu\text{m}$ , and the other images are at the same magnification.



## 4.3 Effects of controlled nanofiber array on cell guidance

### 4.3.1 Experimental conditions

Cell studies were performed using human dermal fibroblasts (6th and 10th passage) purchased from Lonza (Basel, Switzerland). The cells were cultured in Dulbecco's modified Eagle's medium (DMEM) (Lonza, Basel, Switzerland) containing 10% fetal bovine serum (FBS) supplemented with penicillin–streptomycin (Sigma, St. Louis, MO, USA). Cultures were incubated in a humidified atmosphere of 5% CO<sub>2</sub> in air at 37°C. Prior to the cell seeding, all nanofiber scaffolds were sterilized in ethanol for 24 hours under ultraviolet irradiation, and were coated with fibronectin at 10 µg/ml for 1 hour. Cells were harvested using trypsin/EDTA and resuspended in DMEM. Cells were then seeded onto the scaffolds at its density of 10<sup>4</sup> cells per scaffold, and incubated for 7 days in appropriate growth conditions.

After experiments, cells were washed with the warmed DPBS and fixed for 15 min in 3.7 % formaldehyde. After DPBS washing, cells were permeabilized for 20 min in 2 % Triton X-100 and blocked in 3 % BSA (Invitrogen). Following three washes in PBS, cells were stained for F-actin cytoskeleton with Alexa-568-phalloidin (Molecular Probes) at 1:50 dilution in blocking buffer. After rinsing, the nuclei of the cells were labeled with DAPI (300 nM, D1306, Molecular Probes), and then they were finally mounted in a Vectashield (H-1000, Vector Laboratories) to minimize photobleaching. The cells were imaged using a Zeiss fluorescence microscope (Axiovert-200M, Zeiss) equipped with a CCD camera (Axiocam HSM, Zeiss) and image analysis software (Axiovision, Zeiss).

After 7 days of cell culture, the stained cells were observed under a light microscope (Carl Zeiss Axiovert 200M) with phase contrast. 60 cells from each scaffold were randomly selected and the fluorescent images of actin and nuclei were analyzed using ImageTool 3.0 to measure

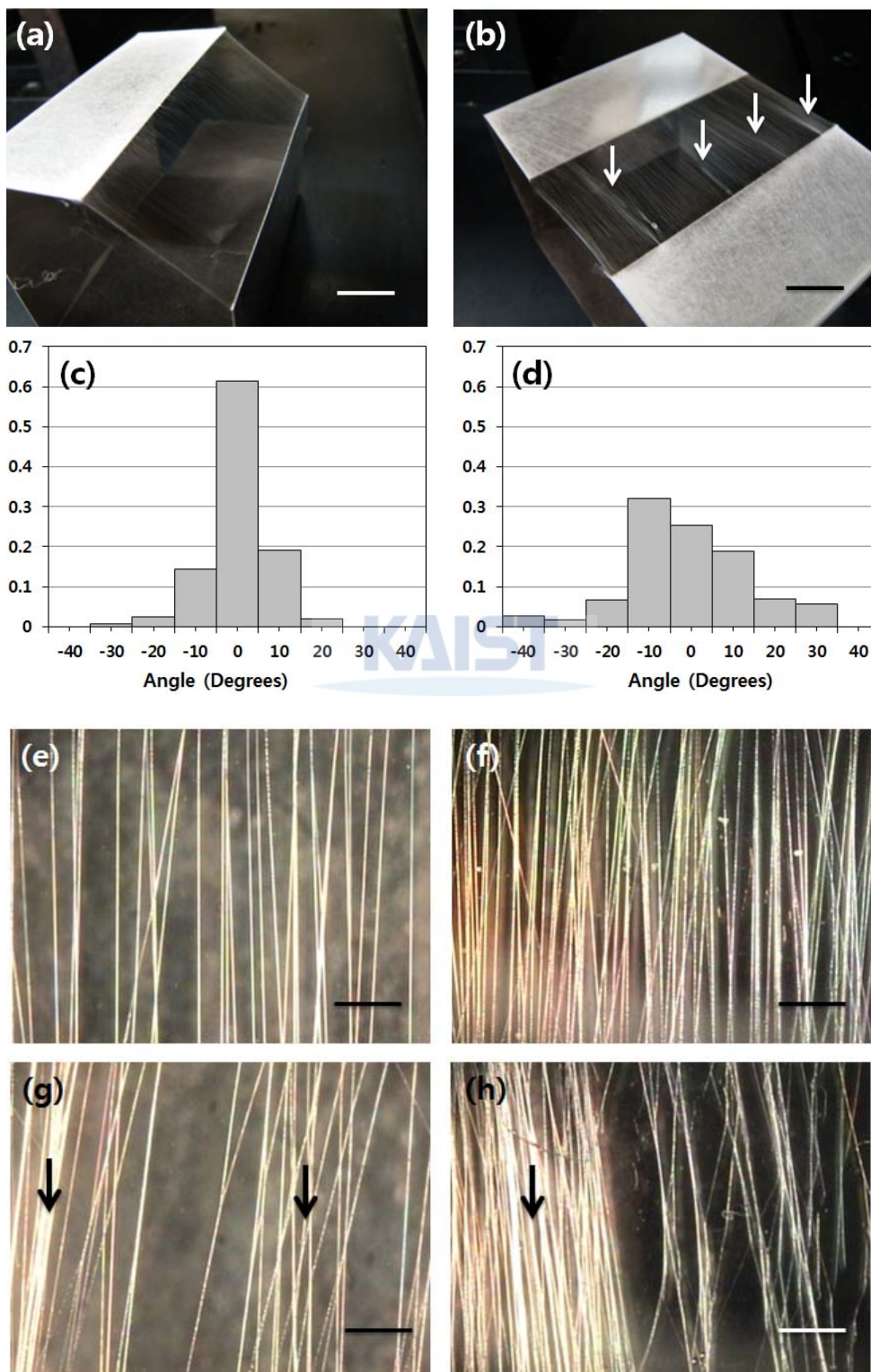
---

the extent of cell alignment. The orientation angle of cell long axis was measured with respect to the reference, which is the desired direction of fiber alignment, i.e. perpendicular axis to the collector edges. In addition, cell elongation factor  $E_f$  was calculated by [29]. The values of the elongation factor were calculated from 30 cells randomly selected from each scaffold. All statically analyses were performed using the Student's t-test. Mean values from different independent experiments were calculated and expressed as the mean  $\pm$  STD.

#### *4.3.2 Fabrication of the controlled nanofiber array*

Polymer solution was prepared by dissolving PCL in the mixture of MC and DMF at the concentration of 20 wt% defined as the proper condition in the previous chapter. The higher concentration than that of the typical electrospinning could allow the successful suspension within the inclined void gap due to the sufficiency of the fiber solidification. The PCL solution was electrospun from a 25-gauge needle connected to a power supply at an applied voltage of 14 kV. The infusion rate of solution through the needle was 0.6 ml/h. The randomly configured nanofiber mesh was obtained by simple electrospinning toward a thin PDMS membrane adhered to slide glass lying on the grounded metal plate. The spinning time was 2 min.

The collector for the formation of uniaxially aligned nanofibers consisted of the two separate aluminum strips (0.2 mm thickness), which were fixed horizontally and vertically at upper and lower position, respectively. This height difference between the strips formed the void space and the electrospun nanofibers were suspended along the void gap. The spinning distance from the needle tip to the upper strip was determined as 160 mm. The suspended nanofibers with uniaxial alignment were transferred onto a surface of the PDMS membrane adhered to the slide glass and both ends of the fiber array were anchored with Permout (Fisher Scientific, Pittsburgh, PA).



---

Figure 4-5. Comparison between results of the inclined and the planar gap collection: Photographs of the fiber arrays suspended on (a) the inclined gap collector and (b) the planar gap collector. Histograms of angle distribution of fiber alignment in the arrays transferred from (c) the inclined gap collector and (d) the planar gap collector. Homogeneous fiber arrays collected from the inclined gap by (e) single transfer and (f) 3 transfers. Inhomogeneous fiber arrays collected from the planar gap by (g) single transfer and (h) 3 transfers. Arrows indicate the inhomogeneous conditions of the fiber distributions. The scale bars are 10 mm (a, b) and 100  $\mu\text{m}$  (e-h), respectively.

As mentioned above, the modification of the configuration from a planar gap to an inclined gap allowed flexibility in time and space for improved alignment effect. As shown in Figure 4-5 (a-d), fiber collection from the inclined gap serves to create better conditions in both the alignment of fiber angle and the homogeneity in fiber distribution whereas irregular distribution of nanofibers was observed in the case of the planar gap (marked by arrows in Figure 4-5(b, g, h)). These irregularities would be accumulative as the number of transfers increased, as shown in Figure 4-5 (g, h). Thus, since multiple transfers were necessary to create a nanofiber array of higher density, the use of inclined gap configuration would be more advantageous in generating more homogenous scaffolds

For the one transferred fiber array, most of the intervals between the fibers appear to be several tens of micrometer which is larger than typical eukaryotic cells; for instance, the size of a fibroblast is about 10  $\mu\text{m}$  in length and 2 – 3  $\mu\text{m}$  in width [90]. Thus, a sub-ten-micrometer scale of fiber distance would be desired to ensure the interaction between the cell and the nanofibers. By employing multiple transfers on an inclined configuration, a reduction of fiber distance can be attained at approximately 2  $\mu\text{m}$  when 20 transfers were carried out [Figure 4-4(d)]. As the quantity of nanofibers collected from single step electrospinning was nearly

invariable for the determined spinning time of 30 sec, the fiber quantity within the array would be proportional to the number of transfers. These results confirm the feasibility of the quantitative control of nanofibers using multi-transfers of nanofibers using the inclined configuration of collector [Figure 3(a, c, e, f)].



Figure 4-6. (a) Photograph of nanofibers collected on the upper strip and within the gap space. SEM images of (b) the microscale fibers deposited directly on the upper strip (The scale bar is 5 μm), and (c) the sub-microscale fiber uniaxially suspended within the gap space (The scale bar is 2 μm).

While conventional electrospinning uses a simple electrically grounded collector without a gap, the collector used in our method comprises of two aluminum sheets separated by a gap. Because this collector configuration with a gap is designed such that as-spun fibers become suspended between both edges of the sheets, relatively rigid jets and fibers are preferred for stable suspension. When the initial concentration of the utilized solution is high, the whole jets and fibers throughout the spinning process exhibit more solid-like behavior. Thus, we increased the solution concentration to 20 wt% from the typical concentration of 10 – 12 wt%.

One concern about increasing the solution concentration for better mechanical stability is its consequence in the increased diameter of the nanofibers [91]. In this process, however, the fiber diameter can be achieved within the sub-micrometer scale despite the relatively high

---

solution concentration. While the fiber deposited directly on the upper strip exhibited a thicker diameter [typically of the order of few micrometers as shown in Figure 4-6(b)], the nanofibers suspended between the edges of the upper and lower strips featured thinner diameters [typically ranging from 400 to 600 nm as shown in Figure 4-6(c)] suitable for tissue engineering applications.

#### *4.3.3 Effects of nanofibrous scaffold on cell guidance*

In order to test how substratum topographies generated from the transferred nanofiber scaffolds influence cell morphology, several specimens of different densities of nanofibers were prepared by varying number of transfers from 1, 5, to 20. Fibroblasts were seeded and cultured for seven days on each scaffold. As shown in Figure 4-7, the degree of cell alignment on the substrate transferred with nanofibers showed positive correlations with the density of fibers. Cells cultured on the scaffolds of 5 and 20 transfers show elongated morphology in the direction parallel to fiber alignment, whereas those on the scaffold of single transfer show little tendency of orientation.

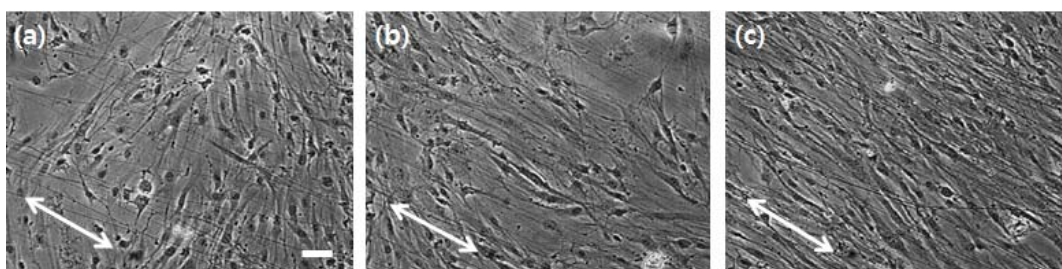


Figure 4-7. Phase contrast micrographs illustrating the cell alignment effect of different fiber arrays for (a) 1, (b) 3, and (c) 10 transfers. The scale bar on (a) is 100  $\mu\text{m}$ ; the other images are at the same magnification. The arrows indicate the direction of the fiber orientation.

To visualize the interaction between the nanofibers and the cultured cells better, cells were fluorescently stained for nuclei and cytoskeletal actin with DAPI and rhodamine phalloidin, respectively. As a control, a bare PDMS substrate without nanofibers [Figure 4-8(a)] and the randomly-electrospun nanofiber scaffolds [Figure 4-8(b)] were used and compared with the aligned nanofiber substrates of different densities [Figure 4-8(c-e)]. All substrates were coated with fibronectin under the identified condition as described in Methods and Materials. The superimposed stack of phase contrast and fluorescent images for nuclei and actin show intimate association of cells with nanofibers [Figure 4-8(b-e)]. The case of randomly oriented fibers shown in Figure 4-8(b) indicates cells' preference for the fibers to the smooth underlying surface. Often, cells stretch along the fiber length and are bounded by neighboring fibers. However, due to its randomness in orientation, neither of the cell alignment distribution nor the elongation morphology was any different from those cultured on the bare PDMS surface.

On the scaffold with a single transfer [Figure 4-8(c)], the cell alignment (55% cells within  $\pm 15^\circ$  of the reference direction) and elongation (the average value of 5.8) were achieved to some extent, but a significant fraction of cells was shown to be unaffected by nanofibers due to large fiber-fiber distance. On the other hand, cells on the scaffolds with 5 and 20 transfers, as shown in Figures 4-8(d) and (e), showed clear alignment and elongation along the fibers. For the scaffolds with 5 transfers, 67% of cells aligned within  $\pm 15^\circ$  of the reference direction and the average elongation factor was 6.8 whereas the scaffolds with 20 transfers showed 95% alignment and the elongation factor of 11.6. Most of the aligned cells span over more than two fibers across its body width. It is noteworthy that the cell guidance appeared to be more effective when the fiber spacing in the scaffold was similar to or smaller than the cell size. In other words, cell contact with the multiple guide topographies may be crucial for contact guidance effect.



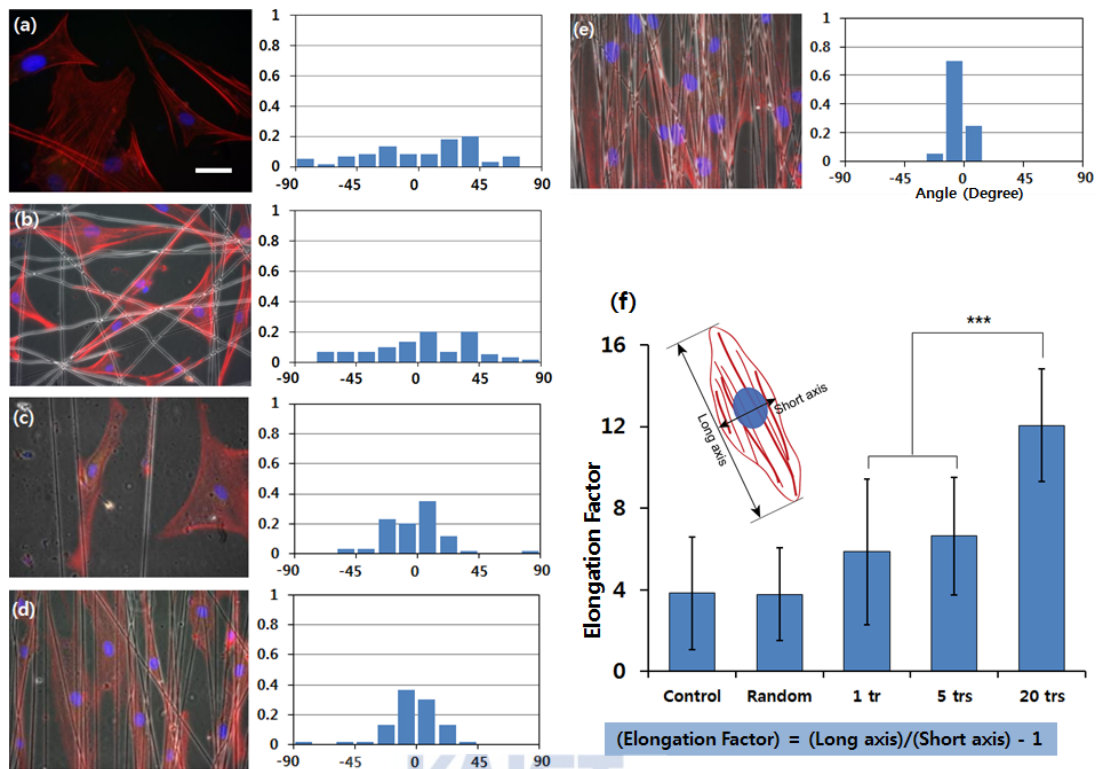


Figure 4-8. Immunofluorescent staining images of cell morphologies and quantitative assessments of cell alignments on (a) bare PDMS substrate without fiber (Control), (b) fiber mesh deposited randomly (Random), (c) singly transferred substrate with aligned nanofibers (1 tr), and multiply transferred substrate with (d) 5 (5 trs) and (e) 20 transfers (20 trs). Red and blue correspond to actin and nucleus, respectively. The scale bar on (a) is 50  $\mu\text{m}$ ; the other images are at the same magnification. (f) Elongation factor ( $E_f$ ) of the each scaffold. Data shown as mean  $\pm$  standard deviation ( $n = 30$  in each scaffold, \*\*\*  $p < 0.001$ ).

Figure 7 shows enhanced formation of parallel actin stress fibers to nano-topologies on scaffolds of high density with 1-3  $\mu\text{m}$  fiber spacing. These results are consistent with those of previous studies [92], where the formation and orientation of actin stress fibers depend on the spacing between micro-topographic features.



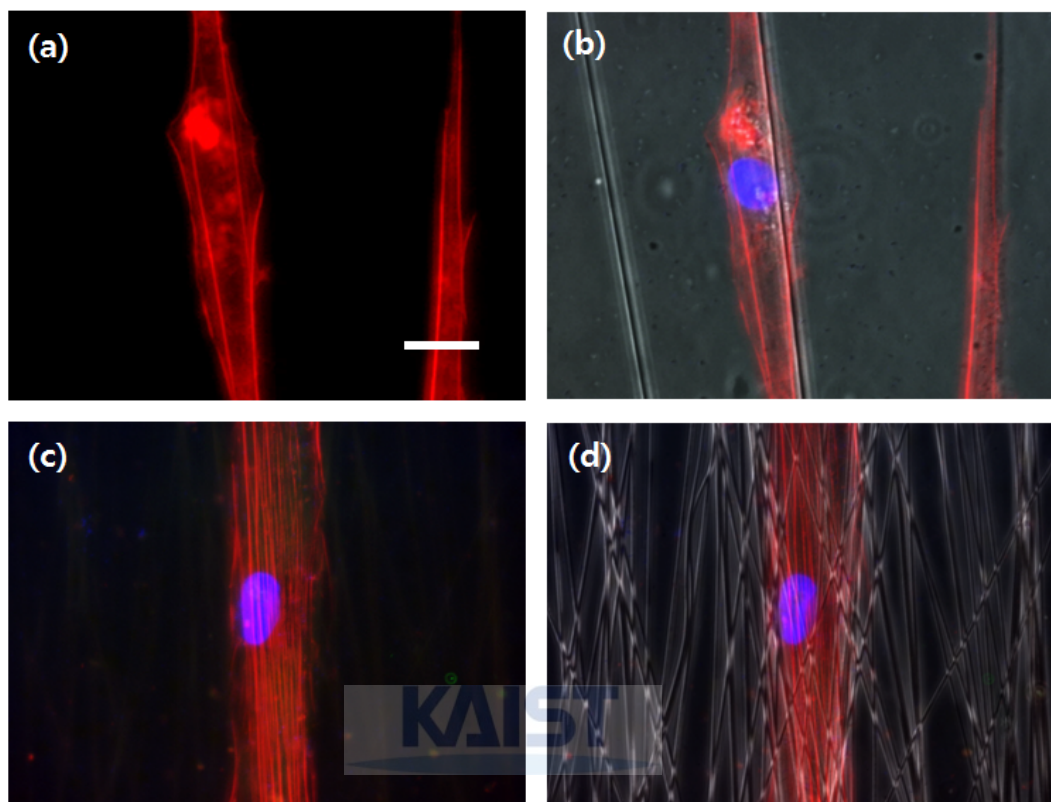


Figure 4-8. Immunofluorescent staining images to visualize the formation of actin stress fiber on the substrate (a, b) with single transfer and (c, d) with 20 transfers. The scale bar on (a) is 30  $\mu\text{m}$ ; the other images are at the same magnification.

This study presents an initial effort to apply uniaxially aligned and uniformly distributed nanofibers to scaffold-based tissue engineering in a quantitatively controlled manner, and implies that a highly dense scaffold with nanofiber alignment would have functional significance. Besides as a dermal fibroblast used for wound healing strategy, the developed nanofiber scaffold could potentially contribute to other tissue engineering applications where tissue anisotropy is a critical factor (e.g., blood vessels, muscles and nerves) and thus other cell types should be tested for efficacy of the scaffolds. In addition, because of the material universality of the electrospinning

---

process, naturally occurring polymers such as collagens can be tested as scaffold materials.





---

## CHAPTER V

# DUAL-SCALE HIERARCHICAL SCAFFOLD FABRICATION BY THERMAL FUSION PROCESS

### 5.1 Introductory remarks

Similarly to the FDM process, the process material undergoes twice through phase transition in the DPMD process. In the first step, the PCL granules being in solid state are heated so that they can be melted and extruded through the nozzle. The second phase transition takes place when the PCL extrudate in microfibrous form touches the substrate and quickly solidifies according to the temperature and the thermal conductivity of the substrate. After the deposition of the first layer, the successively deposited layers for the lamination process are deposited under the same conditions as the first layer deposition. The deposition of the second and subsequent layer is conducted on the top of the previously deposited layer. For the 3D assembly between the layers, the stable bonds between layers are required. Since self-adhesion of thermoplastic behavior is characterized as the fundamental mechanism for the laminated assembly, the thermal process conditions such as thermal boundary and temperature should be carefully determined.

In this research, a hybrid process for fabrication of 3D scaffold, which consisted of a microfibrous structure fabricated using the DPMD and nanofibrous matrices by the electrospinning method, was tried. Insertion of the nanofiber mats between the layers of 3D

structure causes different conditions in the thermally self-bonding procedure from the case using DPMD alone. This chapter focuses on the characterization of the hybrid process so that it is feasible to fabricate the dual-scale hierarchical scaffold using both electrospinning and the DPMD process.

## 5.2 Thermal fusion of microstructure with nanofibers

### *5.2.1 Concept of thermal fusion*

The principle of thermally fused assembly is to deposit the extrudate in the molten state onto the previously deposited layer surface. In other words, self-adhesion of thermoplastic materials, in the presence of phase transition and prolonged exposure to high temperature, is the basic mechanism for the thermal fusion. Figure 5-1 illustrates one example of the combined fabrications using electrospinning and the DPMD process.

In this case, the hybrid process consisted of a two-step sequential process. As a woodpile-like structure was fabricated in a layer-by-layer approach, the nanofiber matrices were inserted between each layer of the microfibrillar structure. The first microfiber layer of the scaffold is built via the DPMD process using the process parameter based on the target design. An electrospun nanofiber matrix was then spread onto the microfiber layer. Subsequent microfiber layers combined with nanofiber matrices were repeatedly laminated onto the previously combined layers so that a 3D hybrid structure could be fabricated. While the DPMD process was carried out, a microfilament in a molten state was extruded onto the prior unit layer. As it solidified for a few seconds, the microfilament adhered to a local region, where it came in contact with the prior unit layer. Every unit layer, therefore, was attached to the adjacent layers to form a complete 3D

---

hybrid structure.

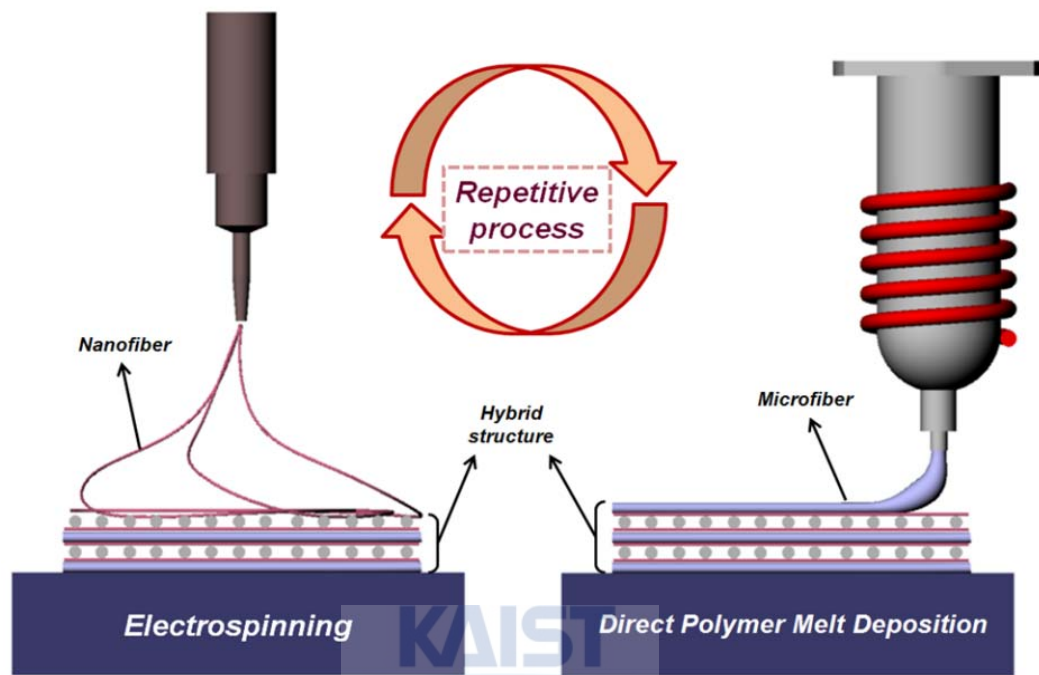


Figure 5-1. The hybrid scaffold containing microfibers and nanofiber matrices built via a combined process of DPMD and electrospinning.

The concept of thermal fusion is illustrated in Figure 5-2. In the first step, the polymer melt extruded through the nozzle is deposited onto the surface of nanofiber mat. As the extrudate in the molten state contacts the nanofiber mat, conduction heat transfer to the nanofiber mat takes place. If the heat transfer in the mat is carried out at the sufficiently high temperature, the thermal fusion between the nanofiber and the micro-extrudate can be accomplished by melting and resolidification, namely self-adhesion process.

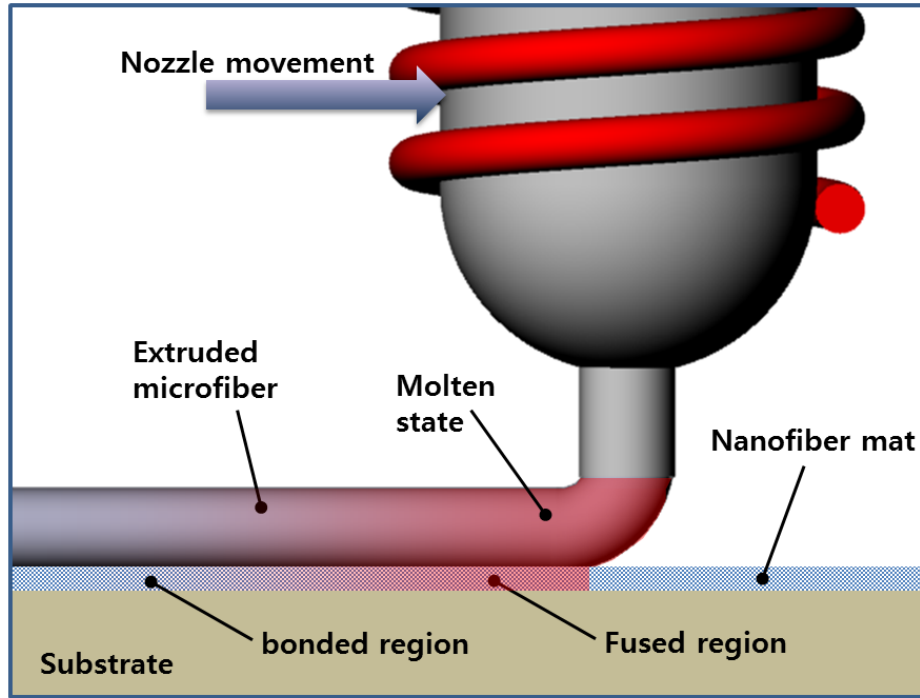


Figure 5-2. Principle of thermally-fused assembly between micro-extrudate and nanofiber mat.

The self-adhesion or thermal interface healing is also important in other thermoplastic processing methods such as thermal extrusion, welding, and injection molding. According to Wool and coworkers [93], the degree of self-adhesion was defined as the ratio of interface mechanical strength to bulk material strength. It was based on the isothermal theory of interface healing and depended on 1/4 power of residence time ( $t$ ) spent above a critical bonding temperature.

$$\alpha = \frac{\sigma_i}{\sigma_b} = K(T_i)t^{1/4} \quad (5.1)$$

The healing function  $K$  has Arrhenius type dependence on the interface temperature  $T_i$  as

---

the following form.

$$K(T_i) = A(T_c) \exp \left[ \left( \frac{E_a}{R} \right) \left( \frac{1}{T_c} - \frac{1}{T_i} \right) \right], \quad T_i > T_c \quad (5.2)$$

$$K(T_i) = 0, \quad T_i \leq T_c \quad (5.3)$$

, where  $A$  and  $E_a$  are material constants indicating the rate of healing at the critical bond temperature and the activation energy for the healing process,  $R$  is the universal gas constant, and  $T_c$  is material-dependent critical bonding temperature.  $T_c$  can be identified as the melting temperature. From the relationship for the self-adhesion process (interface healing), it should be noted that the temperature condition is the most crucial factor in the bonding process.

### *5.2.2 Numerical analysis of the fusion process*

In this section, thermal characteristics of the self-adhesion process between the micro-extrudate and nanofiber mat are investigated by numerical analyses. During plotting molten polymer microfiber onto nanofiber mat, a thermal field through the depth of nanofiber bed is generated continuously in the plotting direction, as shown in Figure 5-3.



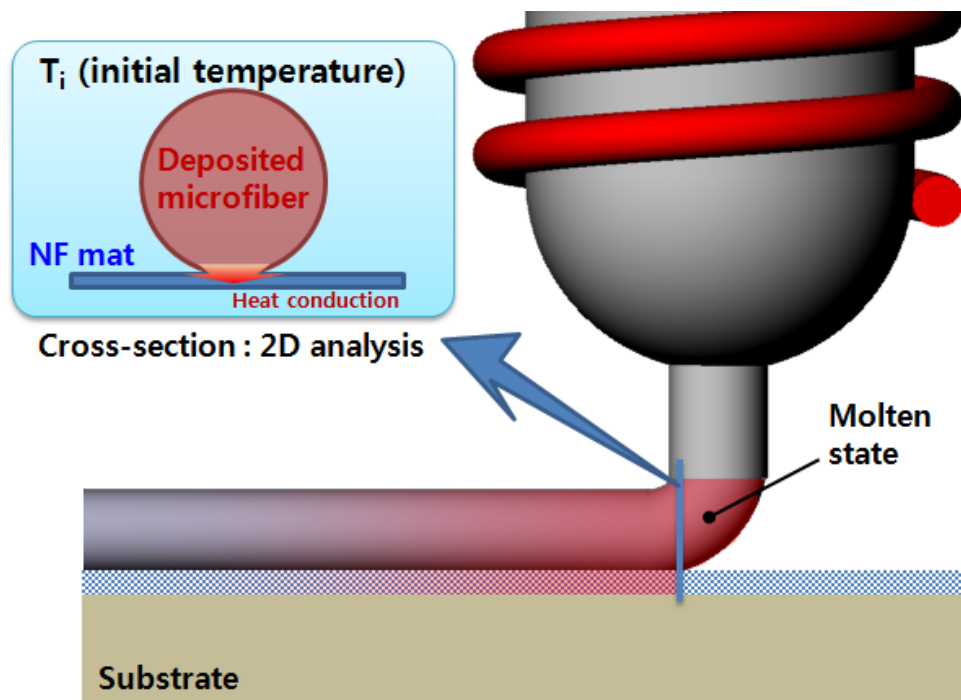


Figure 5-3. Schematics of thermal field during plotting a molten polymer.

The thermal field depends on the initial temperature of the micro-extrudate, the elapsed time after the deposition, the thickness of nanofiber mat, and the material characteristics. The temperature distribution in the thermal field is directly related with the fusion between the microfiber and nanofiber array. The phenomenon of thermal field for the fusion is simulated using commercial software Flow 3D 9.0.

The following assumptions were made in the finite element modeling:

1. The deposited microfiber is initially in the molten state at the pre-determined temperature according to the nozzle temperature, and contacts the nanofiber mat in a single point at the initial step.
2. The deposited materials do not flow in the direction of deposition or nozzle movement

---

so that the phenomenon can be simplified as the field of 2D cross-section.

3. The nanofiber bed is a porous structure at the temperature of 293 K initially. The porosity is determined as approximately 30 % measured by pre-experiments.

The physical properties of the PCL for thermal analysis are thermal conductivity, density, specific heat, latent heat, and melt viscosity. The material data are shown in Table 5-1.

---

<b>Viscosity</b>	<b>10000 Pa·sec</b>
<b>Liquid density</b>	<b>1.11</b>
<b>Solid density</b>	<b>1.22</b>
<b>Thermal expansion</b>	<b><math>7.2 \times 10^{-4} \text{ K}^{-1}</math></b>
<b>Specific heat</b>	<b><math>1.91 \text{ J} \cdot \text{g}^{-1} \cdot \text{K}^{-1}</math></b>
<b>Thermal conductivity</b>	<b><math>0.4 \text{ W} \cdot \text{m}^{-1} \cdot \text{K}^{-1}</math></b>
<b>Latent heat of fusion</b>	<b><math>82 \text{ J} \cdot \text{g}^{-1}</math></b>
<b>Solidus temperature</b>	<b>58 °C</b>
<b>Liquidus temperature</b>	<b>60 °C</b>

---

Table 5-1. Material properties of PCL for thermal analysis.

In order to determine the analysis geometry of the thickness of the nanofiber bed, the cross-section of the nanofiber mat transferred repeatedly was observed as shown in Figure 5-4. When the number of transfers was 40, the thickness was approximately 11  $\mu\text{m}$ .

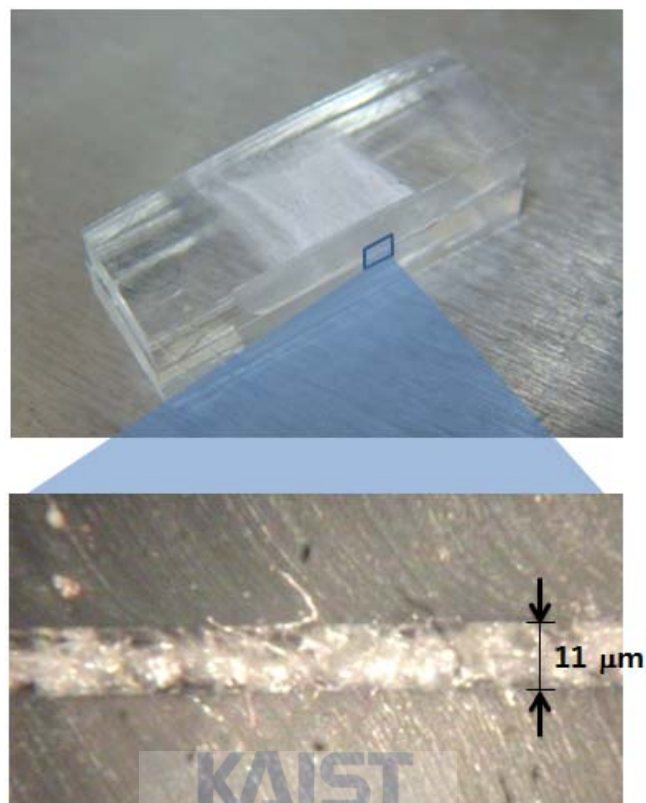


Figure 5-4. Cross-section of the nanofiber mat transferred repeatedly up to 40 transfers.

The transient heat transfer analysis is carried out to estimate the temperature distribution in the nanofiber mat. According to the previous observations, the diameter of the microfiber deposited in the molten state and the thickness of the nanofiber mat are 400  $\mu\text{m}$  and 10  $\mu\text{m}$ , respectively. The thermal fusion procedures can be divided into three steps as shown in Figure 5-5.

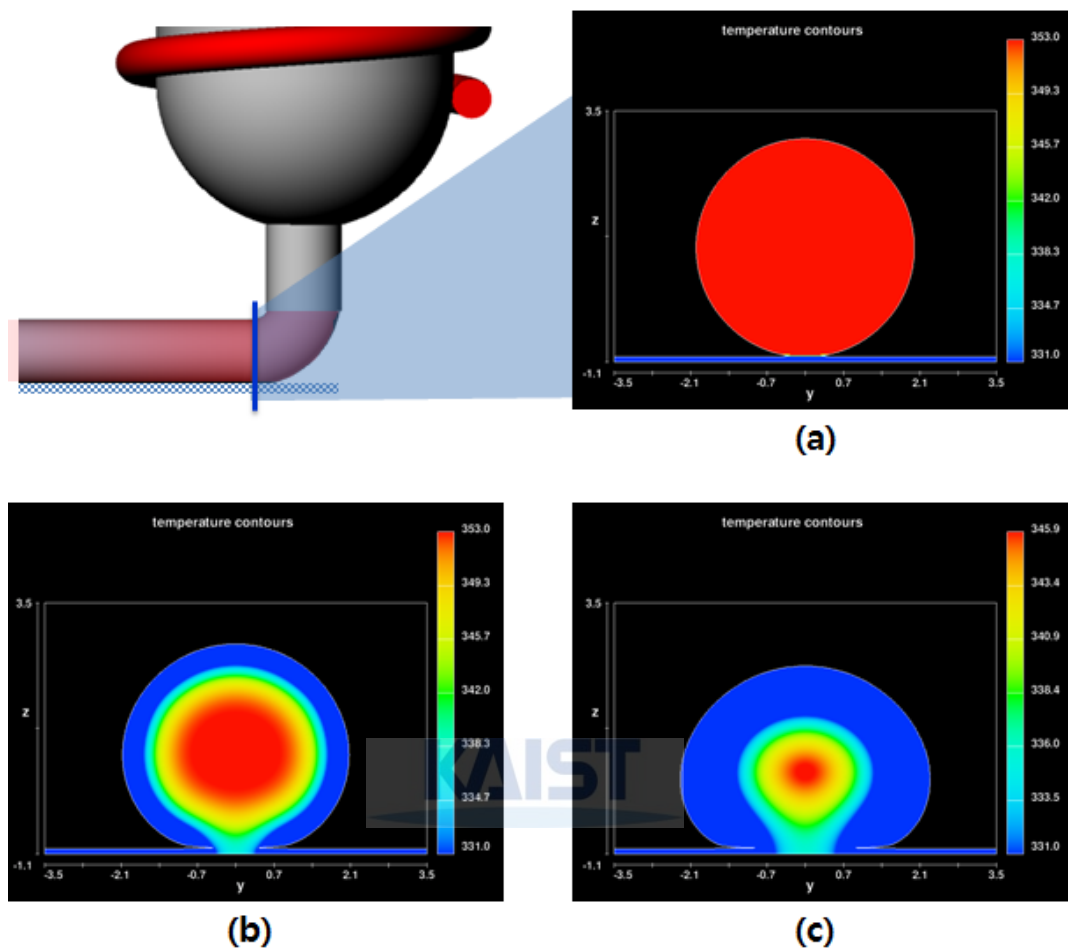


Figure 5-5. Three steps of the thermal fusion procedures; (a) Microfiber in a molten state is laid on the nanofiber mat having initially the room temperature. (b) Fused region is generated and penetrated into the nanofiber mat. (c) Fused assembly including microfiber and nanofiber mat is solidified as process time elapses.

The thermal analyses are performed in different conditions of process temperatures by changing initial microfiber temperatures (60, 70, 80, and 100°C). Figure 5-6 shows temperature distribution at the time point where the region of thermal fusion in the nanofiber mat is maximized. According to the results, when the initial temperature of the microfiber is over 80°C,

the penetration can progress down to the bottom of the nanofiber mat. In the cases of the temperature lower than this level (such as 60 and 70°C), the penetration of fusion region does not reach out to the nanofiber mat. Thus, the fused assembly would not be expected in these cases of lower temperature.

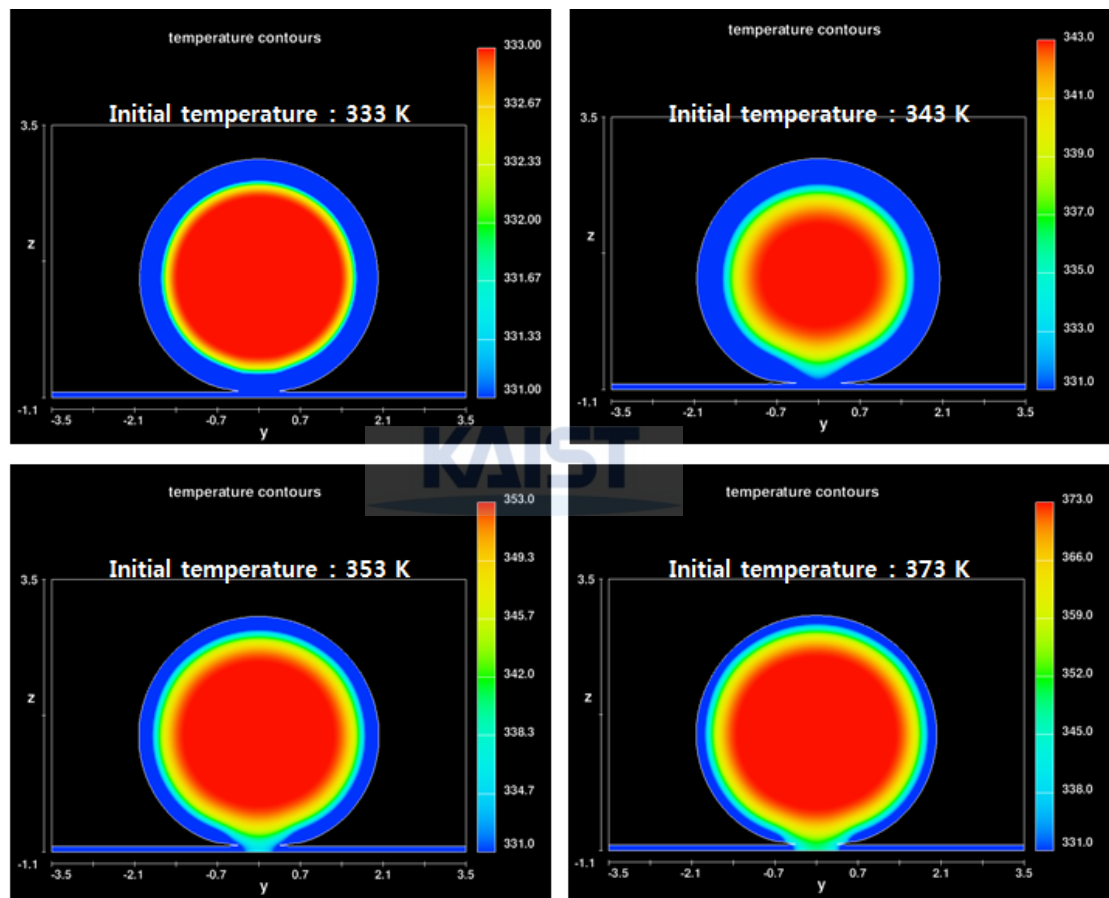


Figure 5-6. Penetration of thermal fusion region in different process temperatures.

---

## 5.3 3D integration by thermal fusion process

### 5.3.1 Experimental results of thermal fusion

In order to evaluate the practical fused region, the surface of the opposite side to the deposited microfiber was observed. As shown in Figure 5-7, it can be found that the fused region is broadened as the process temperature increases. In the case of 60°C, the fused region is hardly seen. This is in accordance with the results of thermal analysis in that the process temperature of 60°C is so low that the penetration of fusion region can not reach the bottom of the nanofiber mat. When the fusion is not completed throughout the thickness like the case of Figure 5-7 (a), the delamination such as Figure 5-8(a) can happen. For the stable fused assembly, the fused region should be distributed down to the bottom of the mat.

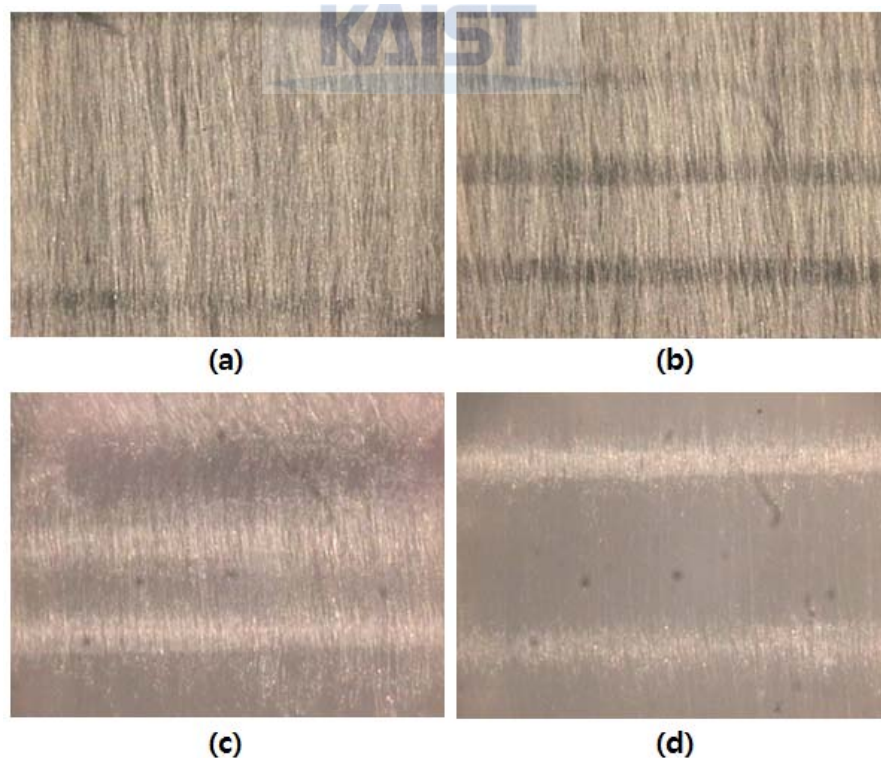


Figure 5-7. Thermally fused region at the bottom of nanofiber mats in the different process

temperatures including (a) 60°C, (b) 70°C, (c) 80°C, and (d) 100°C.

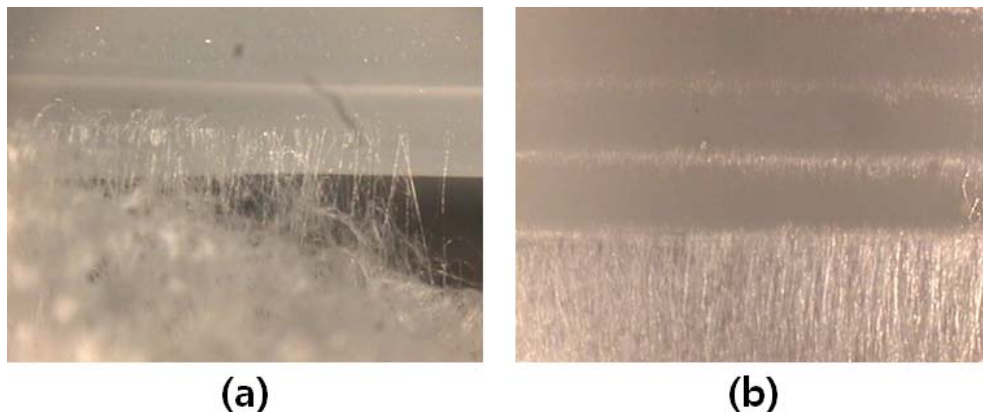


Figure 5-8. (a) Delamination caused by the low process temperature of 60°C, (b) stable fusion at the process temperature of 100°C.

### 5.3.2 3D integration with random and aligned nanofibers

According to the proper process temperature of 100°C, the repetitive process including microfiber deposition and nanofiber transfer was performed. As the two step processes are carried out alternately, the resultant structure has both features of 3D geometry and inner nanotopography, which provides favorable conditions for cell culture. Formation of the inserted nanofiber mats can be varied by the ways of transfer as illustrated in Figure 5-9. When the fundamental electrospinning is performed on the top of the ongoing structure [Figure 5-9 (a)], the electrospun fibers induced to the direction of the grounded bottom plate are formed on the surface of the structure with random configuration. As shown in Figure 5-9 (b), the suspended fibers with aligned configuration can be easily transferred onto the surface of the structure by the lift-up of the processing substrate with the structure. From two ways above, 3D integrated scaffolds were successfully fabricated with insertion of random and aligned nanofiber mat as shown in Figure 5-10.



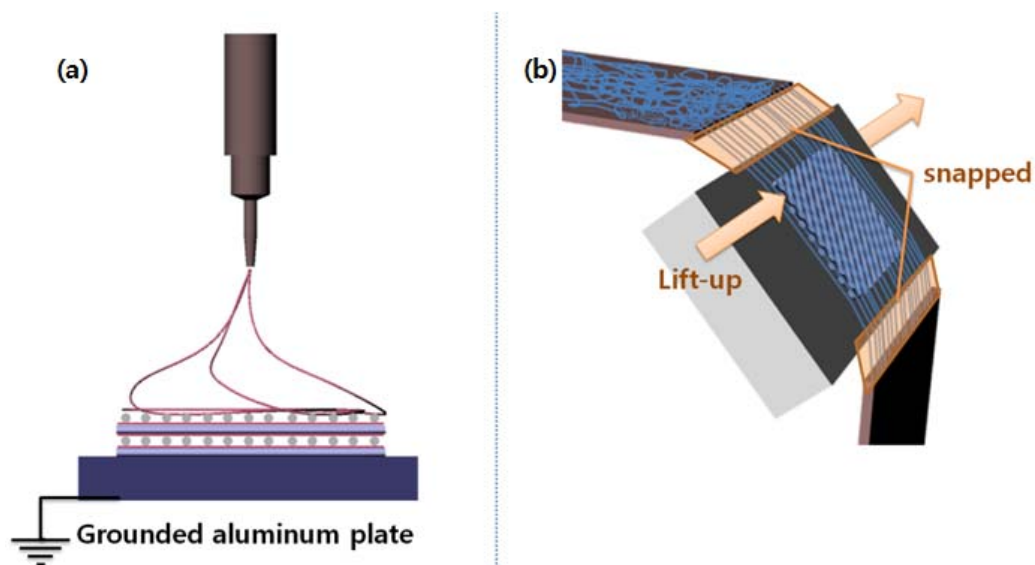


Figure 5-9. Transfer methods of electrospun nanofibers with (a) random and (b) aligned configurations.

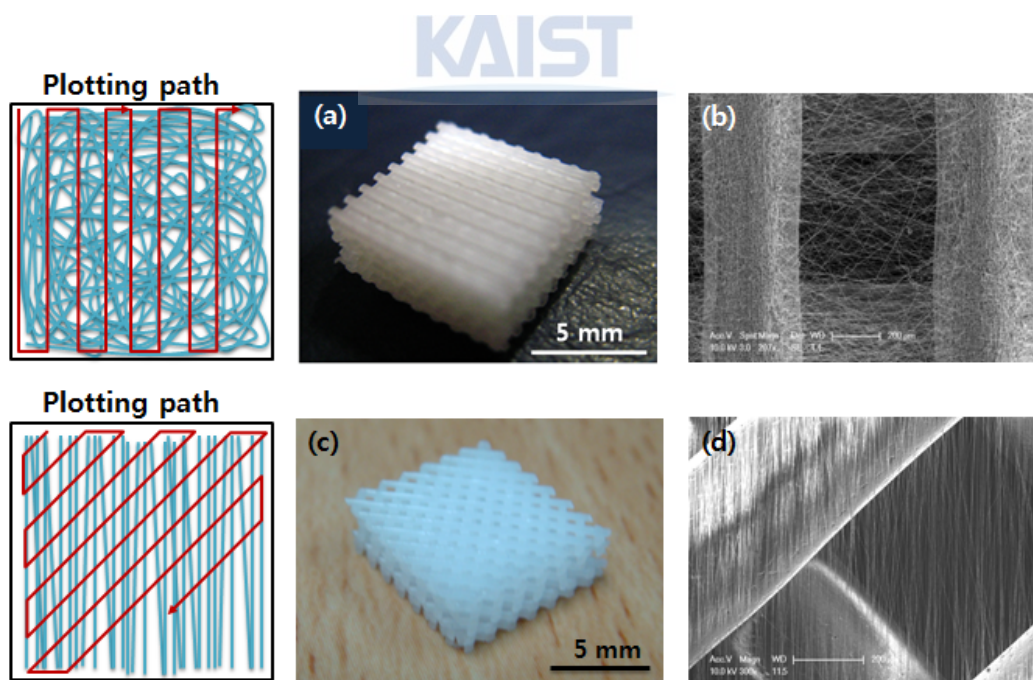


Figure 5-10. 3D integrated scaffolds with insertion of electrospun nanofibers; (a, b) random nanofiber mat, (c, d) aligned nanofiber array.



### 5.3.3 Individualization of nanofiber scaffolds

Additionally, as the plotting paths of DPMD process are arranged at the circumference of the nanofiber mats, an individualized nanofibrous scaffold can be obtained. The individual framed scaffolds with the nanofiber mats are successfully produced as shown in Figure 5-11. These scaffolds have a meaningful feature in that cell seeding and growth on each scaffold can be performed in the parallel way and thereafter 3D tissue formation can be achieved by assembly of the cell/fiber scaffolds. The detailed procedures and cell culture experiments are treated in the following chapter.

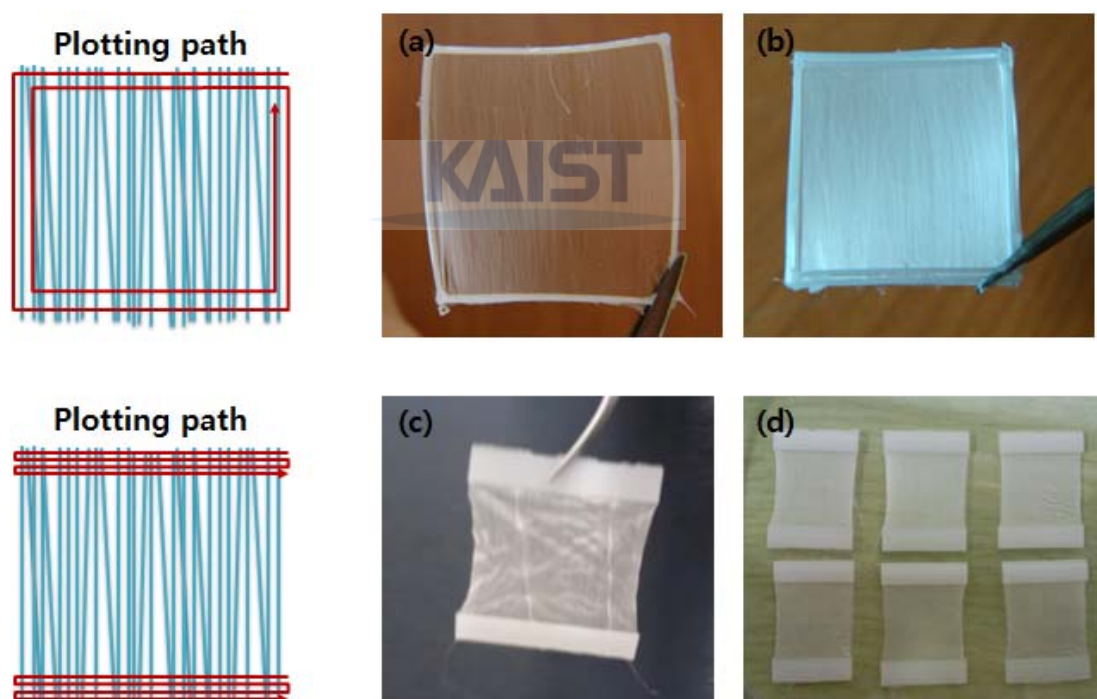


Figure 5-11. Individual framed nanofiber scaffolds with aligned nanofiber array. (a,b) Closed type, (c,d) open type.

---

## CHAPTER VI

### APPLICATIONS FOR 3D TISSUE FORMATION

#### 6.1 Introductory remarks

A unique three-dimensional hybrid structures for tissue engineered scaffolds are produced by combining the direct polymer melt deposition (DPMD) and the various types of electrospinning technique with the random and aligned configurations. The hybrid scaffolds consist of three-dimensionally (3D) integrated microfibrillar structures and nanofibrous matrices between the layers of the integrated structures. To verify the validity of the developed scaffolds from the viewpoint of tissue engineering application, the cell viability, morphology, distribution, and proliferation in the scaffolds were determined as a function of time. Our results imply that this hybrid scaffold provides more preferable 3D biomimetic structure and many potential applications using various cell lines, such as chondrocyte, mesenchymal stem cell, and myoblast.

#### 6.2 3D scaffolds containing random fiber mesh

##### *6.2.1 Materials and process parameters*

Polycaprolactone (PCL, average Mn ca 80,000) and 1,1,1,3,3,3-hexafluoro-2-propanol (HFIP, 99+%) were supplied by Aldrich (Milwaukee, WI). Collagen type I (from calf skin) was

purchased from Sigma (St. Louis, MO). Dulbecco's modified Eagle's medium (DMEM) and phosphate-buffered saline (PBS) were from Gibco BRL (Gaithersburg, MD). The cell counting kit-8 (CCK-8) was obtained from Dojindo Laboratories (Kumamoto, Japan). All other chemicals and reagents were of analytical grade.

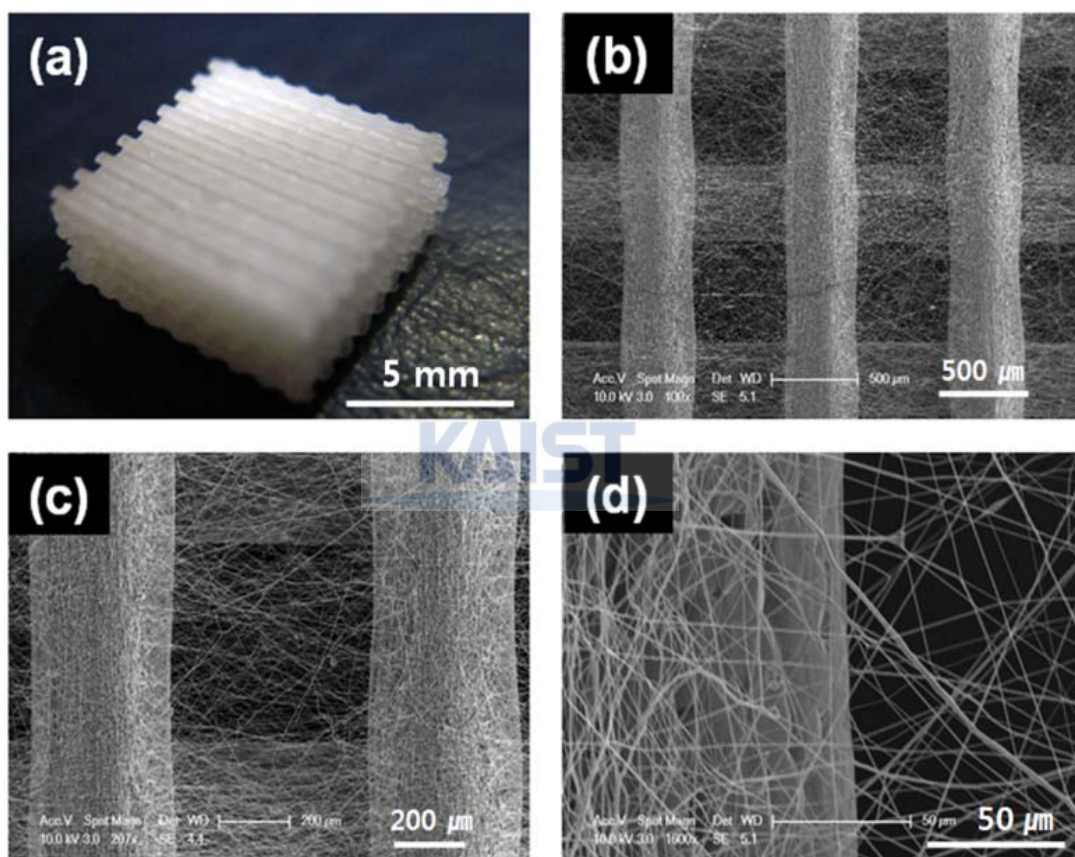


Figure 6-1. (a) Photograph of the overall 3D woodpile structure with dimensions of 9 mm x 9 mm x 3.5 mm, (b) the hybrid basic unit layer composed of microfibers and the electrospun nanofibers matrix, (c, d) magnified images of (b).

The inner diameter of the micro-nozzle connected to the syringe was 400 μm. It is possible to exchange it with another nozzle with a different inner diameter, allowing the fabrication of

---

various micro-scaled fibrous structures. The coiled heater that surrounds the syringe increases the temperature of the material in the syringe uniformly above the melting point. PCL, with a melting point of 57°C, was utilized in this material [33]. In order to extrude relatively low viscous polymer melts, the workable range of the processing temperature was determined to be  $150 \pm 5^\circ\text{C}$ , which is higher than the melting temperature of PCL. The viscosity of PCL is in the range of from 2000 to 3000 Pa·s at the temperature around 150°C and the low shear rate of 0 to 10 sec<sup>-1</sup> [34]. The applied air pressure for the dispensing process was determined to be  $0.55 \pm 0.05$  MPa. Nozzle velocity of the 3D micropositioning system was 1.4 mm/sec. The system fabricated three-dimensional woodpile-like micro structures composed of PCL microfibers as the base architecture of the hybrid scaffolds.

For the electrospinning process, Two different polymer solutions were prepared by dissolving PCL and a PCL/collagen (6/4 weight ratio) blend in HFIP at a concentration of 10 wt% [35]. For the electrospinning process, these two types of solutions were electrospun from a 22-gauge needle on a syringe pump at an infusion speed of 10 µm/min for three minutes. The applied voltage was 18 kV and the grounded collector was placed 10 cm from the needle tip.

Using the aforementioned parameters of the DPMD and electrospinning processes in the earlier chapters, 3D woodpile-shaped hybrid scaffolds could be fabricated. The scaffolds were designed with different compositions of the nanofiber matrix in order to evaluate the extent of the cell adhesion and proliferation. Figure 6-2 shows the three types of scaffolds used in these experiments.

Type I was fabricated by only the DPMD process; this type utilized no nanofiber matrix but just the micro-scaled structure in the form of a cube. Type II scaffolds contained one nanofiber matrix in the middle of the microfiber layers and Type III scaffolds included three nanofiber matrices between each microfiber layer. For the inserted nanofiber matrices, the aforementioned

PCL/collagen mixed solution was used.

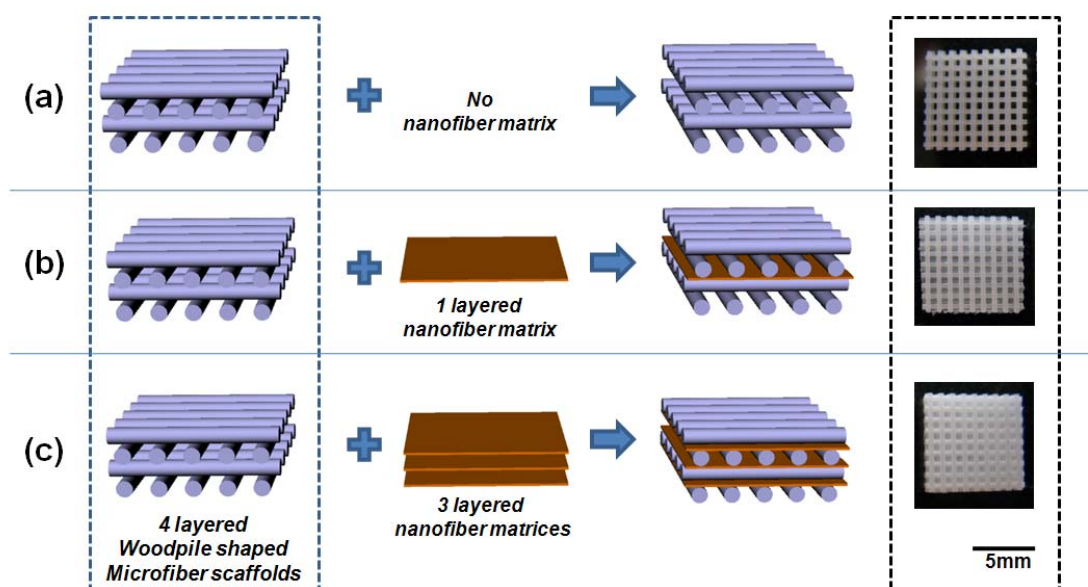


Figure 6-2. Schematic diagrams and photographs of three types of the hybrid scaffolds used in the cell culture experiments: (a) Type I has no nanofiber matrix and only a PCL scaffold as a control specimen. PCL scaffolds combined with (b) a one layer PCL/collagen nanofiber matrix (Type II) and (c) a three-layer PCL/collagen nanofiber matrices (Type III).

Cartilage was acquired from ankle and knee of 6-week-old cow under sterile conditions and chondrocytes were isolated by enzymatic digestion. The bovine chondrocytes were maintained in 175-cm<sup>2</sup> tissue culture flasks (BD Science, USA) at 37°C in a humidified 5% CO<sub>2</sub> environmental incubator. Culture medium consisted of Dulbecco's modified Eagle's medium (DMEM, Grand Island, NY) supplemented with 10% (v/v) FBS, 100 units/ml penicillin, and 100 units/ml streptomycin. To prepare cell suspensions, the cultured cells were harvested using trypsin/EDTA, centrifuged at 1000 rpm for 5 min, and resuspended in DMEM. All specimens were sterilized by

---

UV irradiation for 2 h and in 70% ethanol for 12 h. Ethanol then was exchanged with an excess amount of deionized water and PBS. For homogeneous seeding distribution of the cells, the specimens were placed into a siliconized cylindrical tube, and 5 ml of cell suspensions were inoculated onto 10 specimens at a cell concentration of  $1 \times 10^4$  cells/ml. This was followed by incubation with intermittent agitation for 3 min every half hour for a total of 4 h. Subsequently, the cell/scaffold constructs were washed with DMEM and transferred to siliconized 24-well culture plates containing culture medium for further incubation. At fixed time intervals, each specimen was harvested, washed with PBS three times, and added into 1 ml of fresh culture medium including the cell-counting kit-8 (CCK-8) solution, which generated an orange formazan product by cellular dehydrogenase. After incubation for 2 h, 100  $\mu$ l of each sample was transferred to a 96-well plate to measure the absorbance at 450 nm using a microplate reader (Bio-Rad, Model 550). The number of cells was calculated from a calibration curve obtained from the wells that contained known numbers of viable cells.

### *6.2.2 Effect of nanofibrous surface modification*

Contrary to the woodpile-shaped scaffold consisting of only PCL microfibers, there are two additional types of cell attachable surfaces in the inside of the hybrid scaffold. One is the surface composed of only nanofibers, and the other is the one composed of microfiber partially coated with nanofibers. Regarding the former type of surface, its advanced properties on cell activity have been reported in earlier researches [32, 35]. Before experiment with the 3D hybrid scaffolds, the pre-testing experiments were conducted with three groups of cylinder-shaped microfibers (Figure 6-3) to evaluate both effects of nanofiber coating on the microfiber and the use of PCL/collagen mixed solution as the electrospinning material.



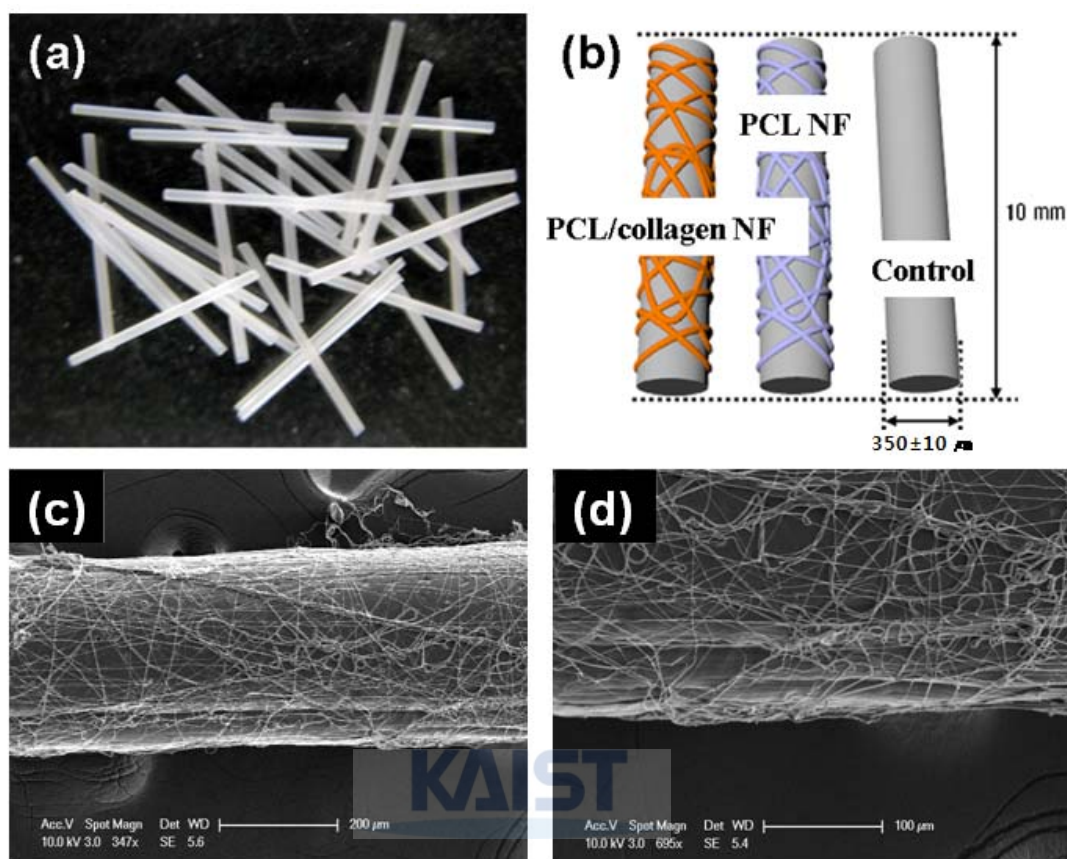


Figure 6-3. Microfiber prepared for the pre-testing experiment: (a) a photograph of microfibers with lengths of ca. 10 mm and diameters of ca. 0.4 mm, (b) a schematic diagram of three different types of microfibers, only microfiber-only, surface-modified microfibers with PCL nanofibers and the PCL/collagen blend nanofibers, (c) SEM image of a microfiber coated with the PCL/collagen nanofibers, (d) magnified image of the PCL/collagen nanofibers deposited on the surface of a microfiber.

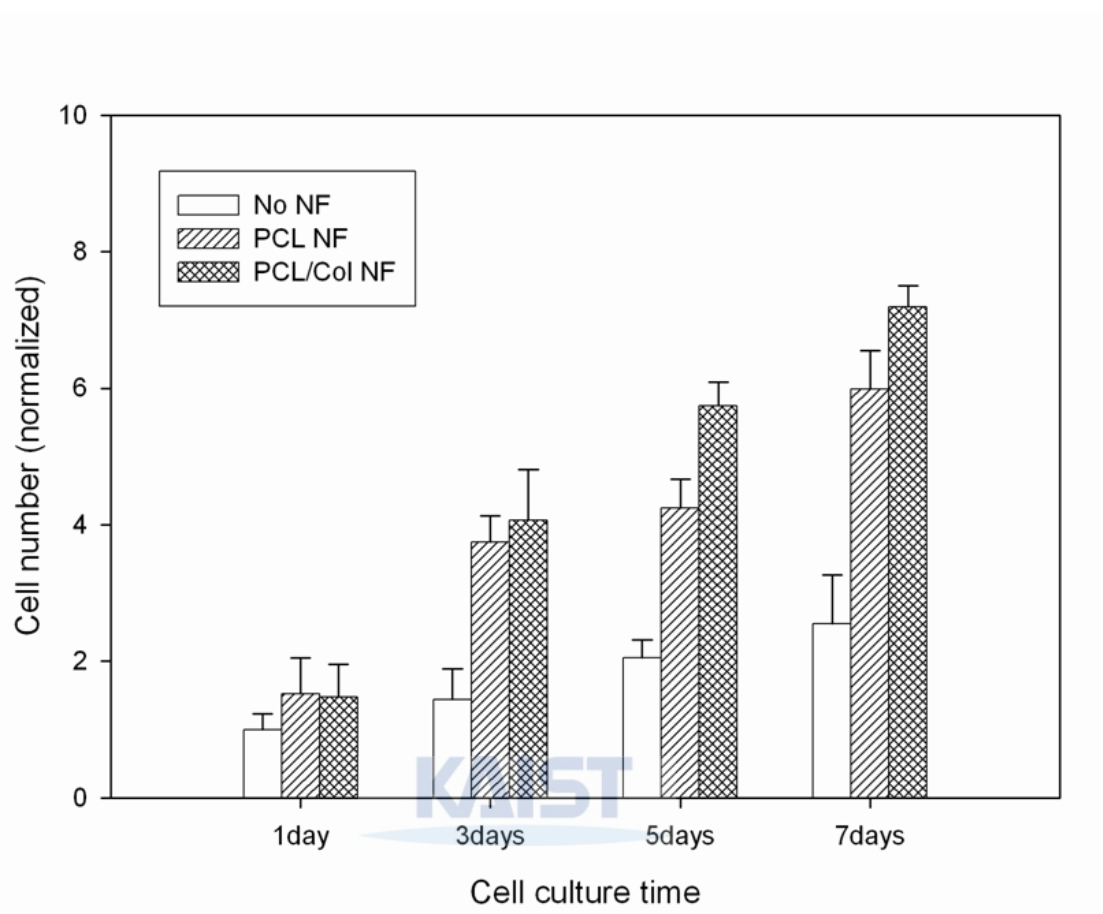


Figure 6-4. Cell proliferation pretest of bovine chondrocytes on different microfibers: microfiber-only, surface-modified microfibers with PCL nanofibers and the PCL/collagen blend nanofibers.

The PCL microfibers were fabricated by the DPMD process, with a length of  $10 \pm 0.5$  mm and a diameter of  $350 \pm 10$   $\mu$ m. The first group of microfiber specimens was not treated and used as control specimens. The second and third groups were placed on aluminum plates where the PCL and PCL/collagen mix solutions were electrospun onto the microfibers. As a result, PCL microfibers were overspread with two types of nanofibers. Collagen is the most abundant extracellular protein in the human body and has been widely used for biomedical applications to



increase the incidence of cell-substratum interaction. Collagen is also an ampholyte polymer; it can increase the charge density of the spinning solution during the electrospinning process [36]. The diameters of the PCL and PCL/collagen (6/4) nanofibers were  $431 \pm 148$  nm and  $325 \pm 128$  nm, respectively. The overall structure of the electrospun fibers can be strongly influenced by the rheological and electrical properties of the polymer solutions. It was found that when blending collagen with PCL (up to 40 wt%), the diameter of the electrospun nanofiber decreases, which is possibly due to reduction in viscosity and increase in charge density of the spinning solution, as reported earlier [23]. When blending over 40 wt%, beads or bead-on-string structures were easily observed, indicating insufficient entanglement of polymer chains due to immiscibility and phase separation between the two polymers.

Micro- or nano-topographical features on the surface of biomaterials can control cellular behaviors such as adhesion, spreading, migration, proliferation, and differentiation to a large extent [37,38]. As shown in Figure 6-4, chondrocyte attachment and subsequent proliferation are enhanced on the surface-modified microfibers with electrospun nanofibers with respect to microfibers having a smooth surface. The number of cells on the surface-modified microfibers with the PCL nanofibers after 24 h was 48% higher compared to the cell number on the smooth microfibers. The cell number continued to increase 2.7 times the original number after 7 days in the culture. There are two possible explanations for this. First, cells can directly react to the nanofibrous topography. Manifold physical topographies including groove, ridge, pore, step, and node topographies were reported to have a significant effect on the type of cellular behavior according to the dimension of the topographies [24]. In other words, the nanofiber surface topography could be sensed by the seeded cells, inducing different cellular reactions with respect to the smooth surface. Second, the nanofibrous structure can enhance serum protein adsorption on the surface of the structures. As the initial cell-substrate interaction is induced by serum protein absorption to the substrate surface, an increase in the level of absorbed protein

---

can cause improvement of cell adhesion [39]. In addition, the chondrocyte number on the surface-modified microfibers with the PCL/collagen nanofibers was further increased, which was 17% higher than those with the PCL nanofibers after seven days of culture. This indicates that collagen was exposed to the surface in contact with the cells which provided a more favorable environment for cell growth. As these experimental results suggest, there were significant improvements in terms of cell adhesion and proliferation when the PCL/collagen blend nanofibers were applied onto the microfiber surface.

### *6.2.3 Cell proliferation in 3D scaffolds*

Figure 6-1 shows the appearance of the final 3D woodpile structure of the hybrid scaffold with its unit layers containing the nanofiber matrix. This figure also shows the horizontal front view of a basic unit layer, which is composed of a PCL microfibrillar layer and a PCL/collagen nanofiber matrix. The overall 3D structure had these unit layers stacked up repeatedly. As observed in Figure 6-1 and 6-2, side channels could be generated by a repeated stacking process. In the later cell seeding experiment, penetration of the cell suspension and cell migration within the hybrid scaffold can occur through these side channels.

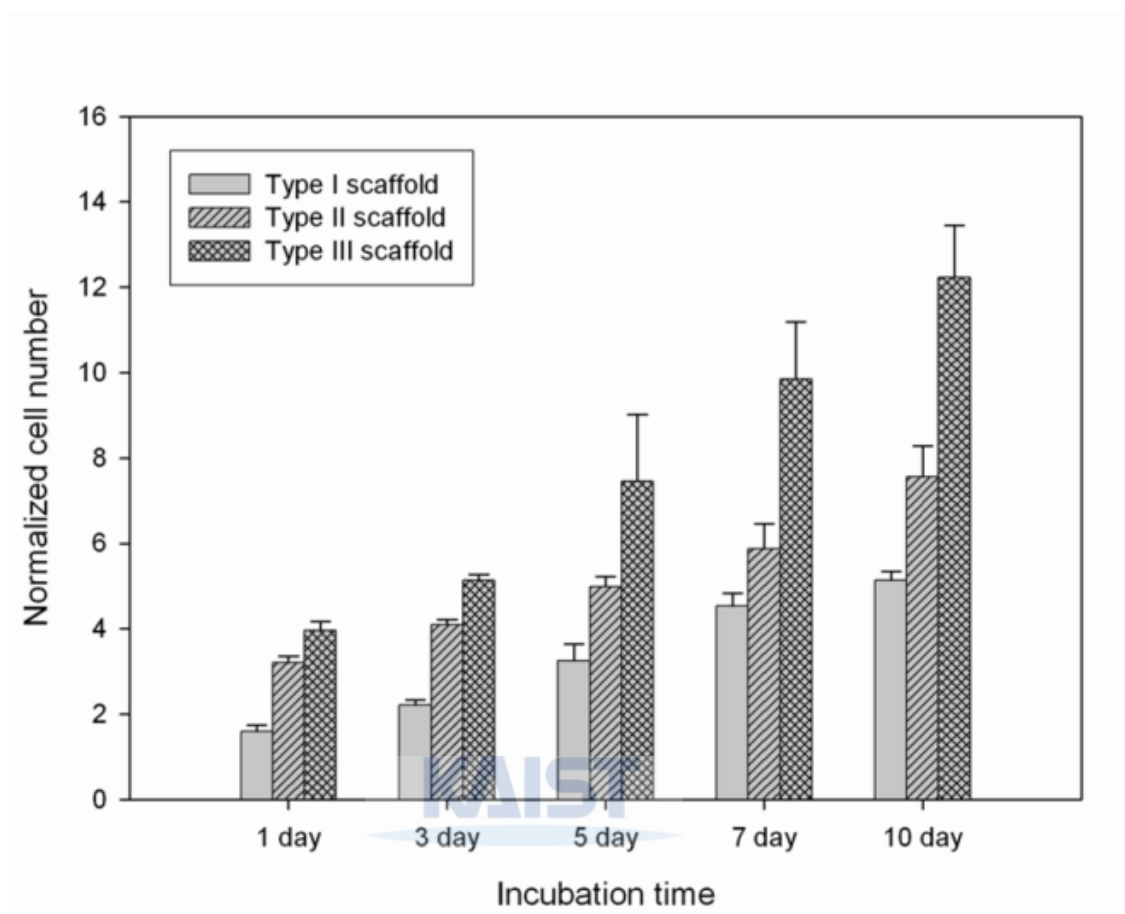


Figure 6-5. Cell proliferation assessment for a 10-day culture period on three types of final scaffolds.

In the proliferation assessment (Figure 6-5), Type III scaffolds showed a 2.2-fold higher cell attachment rate after one day of culture and a 2.5-fold increase in the number of cells at the end of the proliferation period compared to Type I scaffolds. It was also observed that Type III scaffolds showed increased cell numbers that were 1.5 times higher compared to Type II scaffolds after 10 days of culture, resulting in greater hosting ability for the cell population. This result could be explained by the synergistic effect of several factors. Because of the inserted nanofibrous matrices, a quantitative increase of the cell-attachable surface area and the inner

topographical features influence contained quantity of viable cells in the 3D scaffold. Moreover, the use of PCL/collagen biocomposite as electrospun nanofibers improves cell-scaffold interaction, because the electrospun PCL/collagen nanofibers can have amide groups and hydrophilicity for the seeded cells to adhere and proliferate [35]. For these reasons, Type III scaffold that has nanofibrous mats in every unit layer could outperform the other types of scaffolds. These imply that it is possible to modulate the cell population in the scaffold by varying the number of nanofibrous mats so as to meet the requirements for regeneration of different types of tissues. After three days of culture, cell morphology for comparison of the Type I and Type III scaffolds using SEM was examined.

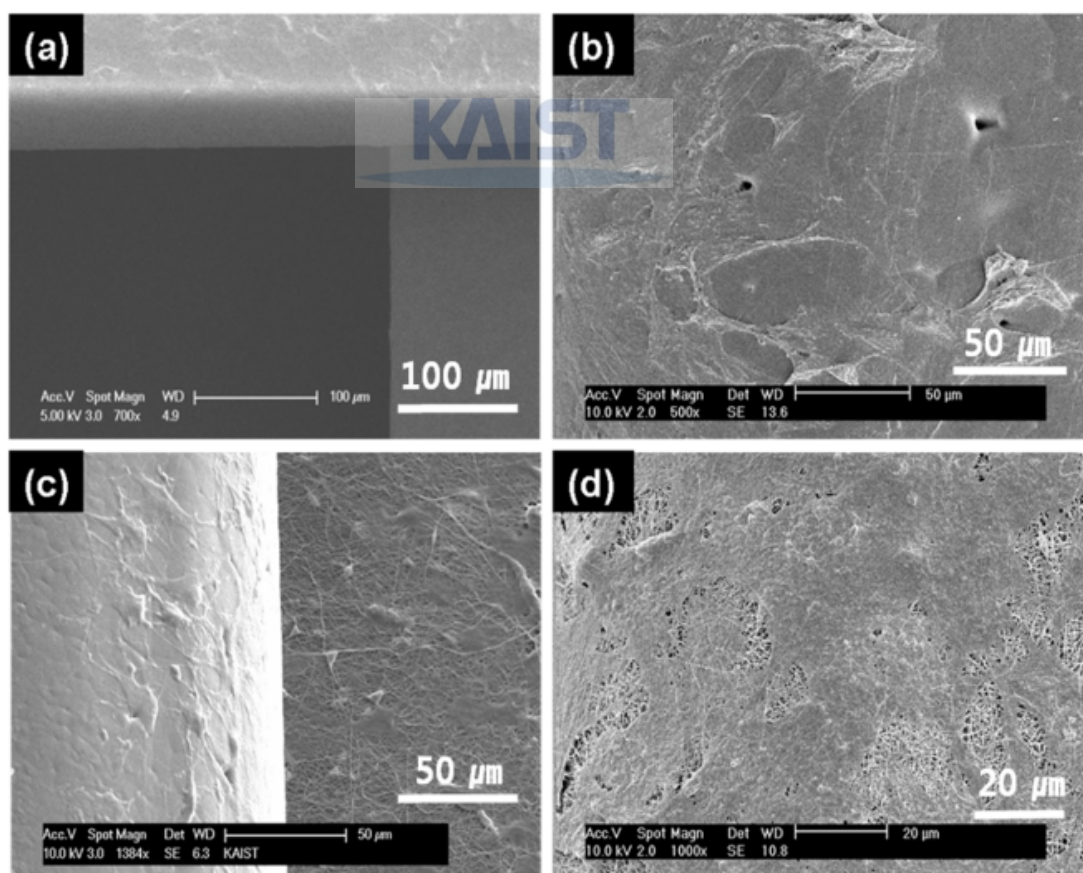


Figure 6-6. SEM images of chondrocytes and scaffold interaction after three days in the

culture: (a) at the junction of two microfibers (arrows indicate attached chondrocytes) and (b) spread cell on the surface in a Type I scaffold, (c) the border of a microfiber (left) and a nanofiber matrix (right), and (d) chondrocytes layered on the nanofiber matrix in a Type III scaffold.

As shown in Fig. 6-6, it was observed that attachment and proliferation of the chondrocytes occurred in the nano-textured hybrid scaffolds with the PCL/collagen electrospun nanofibers. Fewer cells attached to the Type I scaffold, whereas the Type II or Type III hybrid scaffolds resulted in a greater number of cells with extensive spreading in their shapes.

## 6.3 3D scaffolds containing aligned fiber array

### 6.3.1 Materials and scaffold fabrications

In the previous sections, uniaxially aligned nanofiber array for a specific area can be fabricated in a transferrable manner. Figure 6-7 illustrates the transfer process of the collected fibers. The fiber array density for the single transfer is not sufficient to seize the seeded cell (mesenchymal stem cell) on the aligned nanofiber mats considering the cell size is 10 to 20  $\mu\text{m}$ . Thus, for the necessity of higher density, we tried to multiply the transfer of the aligned nanofibers. As the resultant fibers could be transferred repetitively, we could increase the density of the mats and reduce the spacing between the fibers. During the repetitive transfer, the formerly transferred fibers were not damaged and the resultant degree of fiber alignment was not disturbed. Using the DPMD process, a woodpile-like microfibrinous structure was prepared for integration with the aligned nanofiber mats. The resulting diameters of the microfibers in the

---

structure are approximately 450  $\mu\text{m}$ .

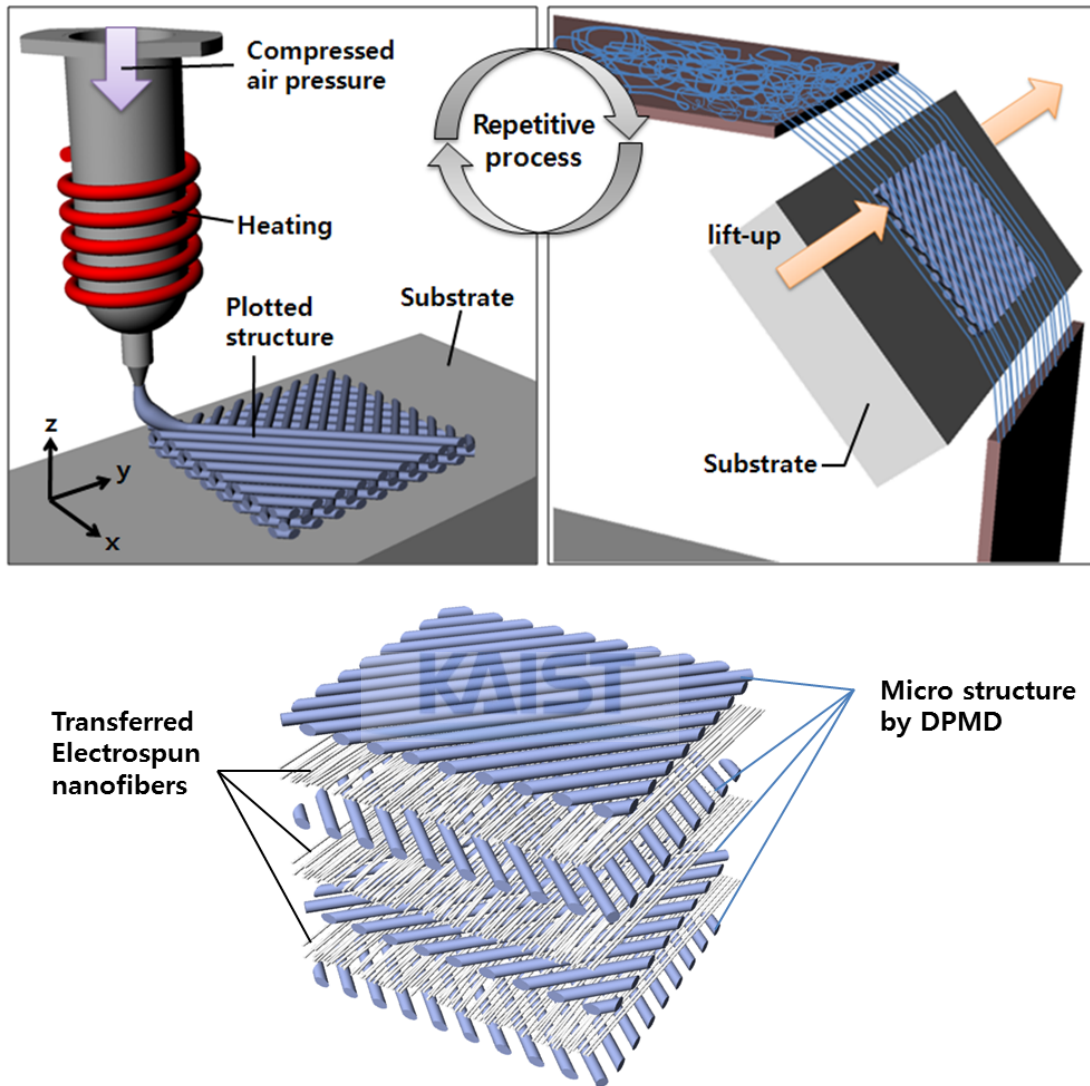


Figure 6-7. Repetitive process of DPMD and transfer of aligned nanofiber arrays and configuration of 3D scaffolds containing aligned nanofiber mats.

As can be seen in Figure 6-7, the aligned nanofiber mats are inserted between each layer of the microfibrinous structure by transfer of the mat before laminating subsequent microfiber layer.

When transferred onto the microfiber array, the nanofibers are periodically anchored to top of the microfiber array. The direction of the microfibrinous array was the alternative of  $45^\circ$  or  $-45^\circ$  to the direction of the aligned nanofibers.

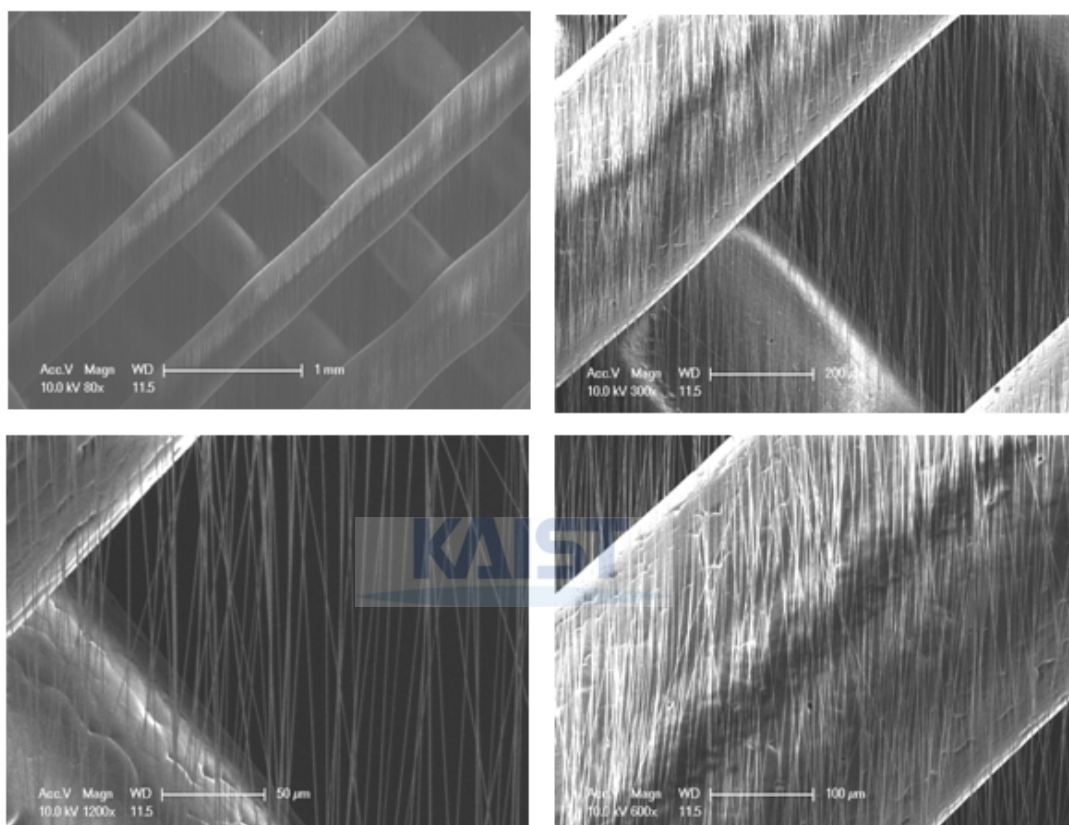


Figure 6-8. SEM image of 3D scaffold containing aligned nanofibers.

This configuration allows the mats to be transferred onto all microfibrinous layers stably and be anchored in the same way as all layers. Being similar to transfer onto the flat glass substrate, the transferred nanofibers sustained their alignment and continuity without significant disturbance (Figure 6-8). These hybrid structures containing aligned nanofibers were laminated successively in a layer-by-layer approach. While deposited by the DPMD process, the extruded



---

microfiber was in a semi-molten state and solidified for a few seconds. This brought about an adhesion of lower and upper structure which had an effect on successful lamination into a 3D structure as mentioned in previous section. Furthermore, it provided more robust in-situ fixation of the aligned nanofibers between microfiber layers due to the successive deposition.

### *6.3.2 Effect of aligned nanofiber scaffold*

The property of cell adhesion and proliferation in each type of scaffold was evaluated by cell culture experiment. The specimens were prepared as illustrated in Figure 6-9. For a cell culture study, human mesenchymal stem cells (hMSCs, Lonza) were expanded in MSC basal medium (MSCBM, Lonza) supplemented with MSCGM Singlequots (Lonza). hMSCs were split at subconfluence and maintained in 75 cm<sup>2</sup> tissue culture flasks (BD Science, USA) at 37 °C in a humidified 5% CO<sub>2</sub> environmental incubator. All specimens were pre-incubated in human fibronectin (Sigma) dissolved in PBS (20 µg/ml) to facilitate cellular adhesion. To prepare cell suspensions, the monolayer-cultured cells were harvested using trypsin/EDTA, centrifuged at 1000 rpm for 3 min and resuspended in MSCGM. Three hundred microliter aliquots of the cell suspensions ( $2 \times 10^4$  cells/ml) were inoculated to various types of the specimens sterilized by ultraviolet irradiation for 2 h and in 70% ethanol for 12 h. This was followed by static culture for pre-determined time points. In order to evaluate the adhered and proliferated cells within the scaffolds, cell counting kit-8 (CCK-8) was used along the protocol as mentioned in the previous section.



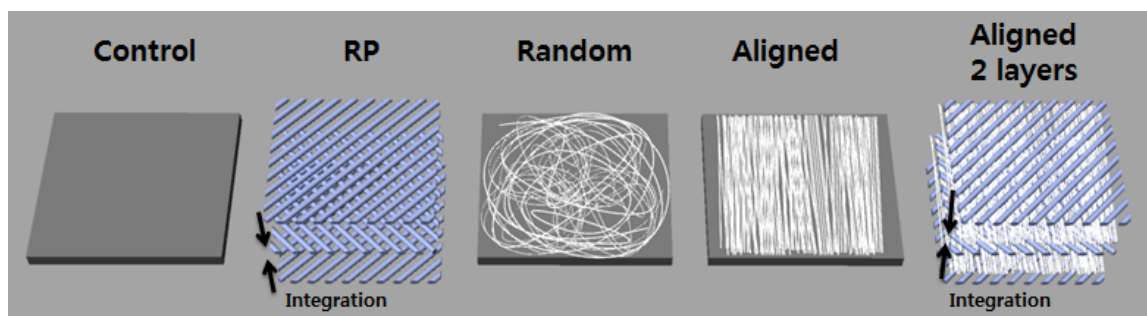


Figure 6-9. Preparation of various scaffolds in order to evaluate the 3D integration with aligned nanofibers.

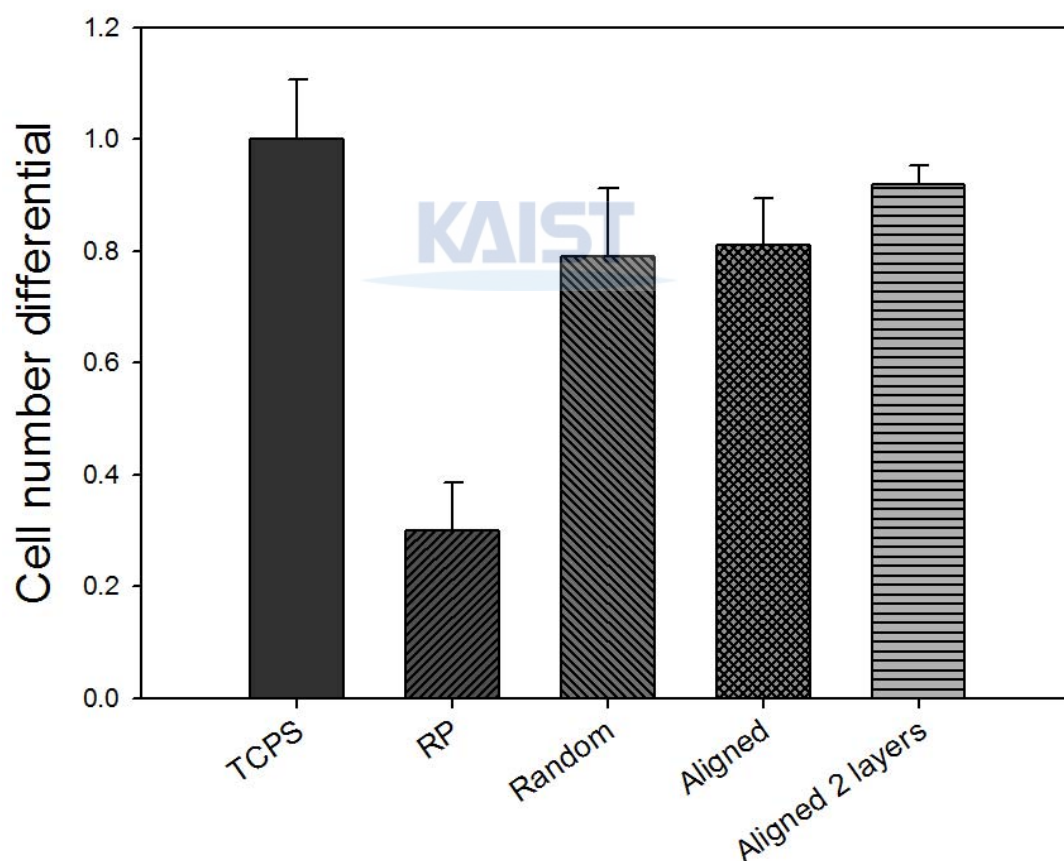


Figure 6-10. Adhesion property of Human mesenchymal stem cell into the various scaffolds.

[Cell number differential = (cell number at initial seeding – cell number after 4 hr incubation) /

---

cell number at initial seeding]

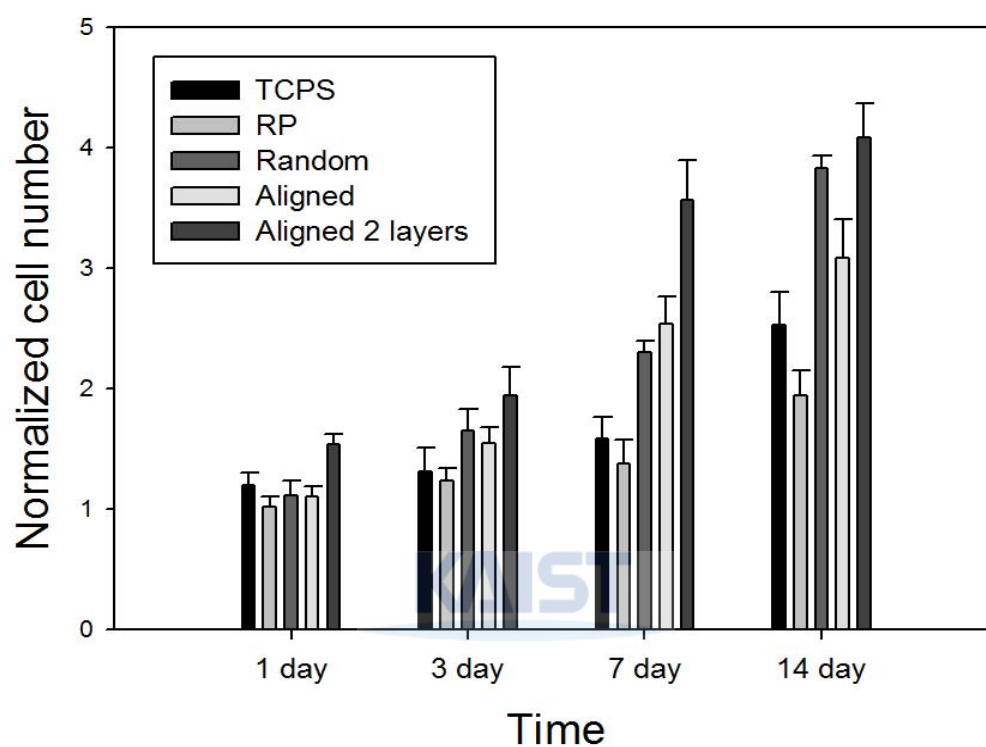


Figure 6-11. Proliferation property of Human mesenchymal stem cell into the various scaffolds.

Through the cell adhesion and proliferation tests, the hMSCs readily adhered and proliferated for up to 7 days in culture. As evaluated in the previous sections, it was confirmed that the nanofiber meshes (Random or Aligned) were more conducive to cell adhesion and proliferation than the scaffolds of the bare type (TCPS or RP). The cell adhesion and proliferation did not show significant differences between the aligned array and the random mesh. In the case of 3D scaffold integrated with the aligned nanofiber array of 2 layers, enhanced results of

cell proliferation are shown for all culture time points. Like the random nanofiber meshes embedded within 3D scaffold, the inserted nanofiber arrays provided additional areas for cell adhesion in 3D environment. This can be confirmed by comparing between the bare RP scaffold and the nanofiber-embedded scaffold. In the proliferation assessment at 14 day, the nanofiber-embedded scaffold shows 2.1-fold higher cell proliferation rate compared to the bare scaffold without nanofiber.

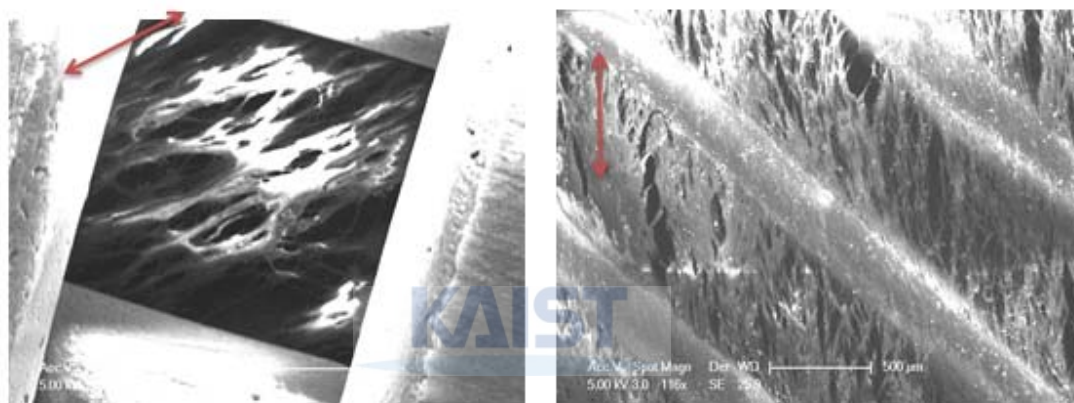


Figure 6-11. Proliferation results of 3D scaffolds containing aligned nanofiber mats (7 days after cell seeding).

SEM images taken at 7 days in the growth medium showed the presence of hMSCs on the aligned nanofiber array embedded within the 3D scaffold (Figure 6-11). The cells were aligned on the uniaxially oriented nanofibers. It is confirmed that the cell alignment along the direction of fiber orientation can be accomplished even in the 3D environment. In the previous works for application of aligned nanofiber array, the supporting substrate was necessary because of fluttering behavior of the thin nanofiber. But in this case, all embedded nanofibers are fused and fixed with microfiber structures at the junctions between every layer. The transferability of the electrospun nanofibers in this process allows that. As well as SEM images, immune-fluorescent

---

staining results show the cell alignment on the inserted nanofiber into the 3D scaffold as shown in Figure 6-12.

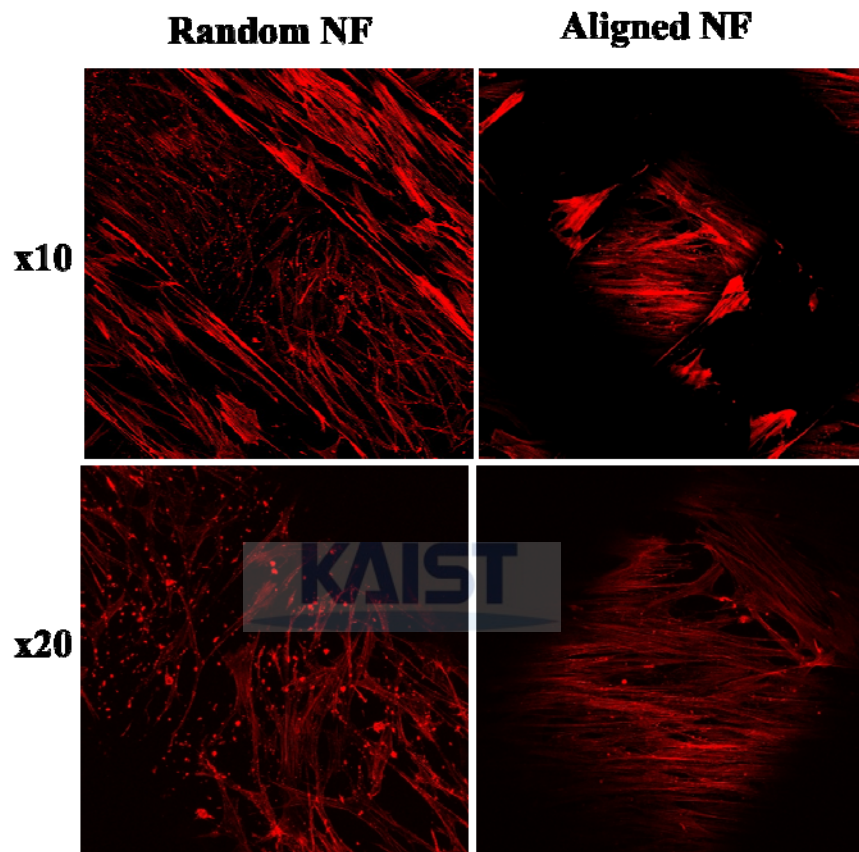


Figure 6-12. Immunostaining results of hMSC actin fibers.

## 6.4 Multilayer assembly of cell/fiber structures

### 6.4.1 Layer-by-layer approach for 3D tissue formation

As previously mentioned, the electrospun nanofiber structure has many advantages in

promoting cell growth, maintaining proper cell phenotype, and manipulating cell behavior along nanofiber orientation. However, some challenges in application of nanofiber to scaffold-based tissue engineering are recognized. The first one is a difficulty to create 3D structure, and the other one is too small pore to infiltrate cells into the nanofibrous meshes. In order to overcome these limitations, on-site layer-by-layer (L-b-L) approach has received attention for 3D tissue generation procedure with the assistance of electrospun nanofibers [94]. The procedure using electrospinning is illustrated in Figure 6-13.

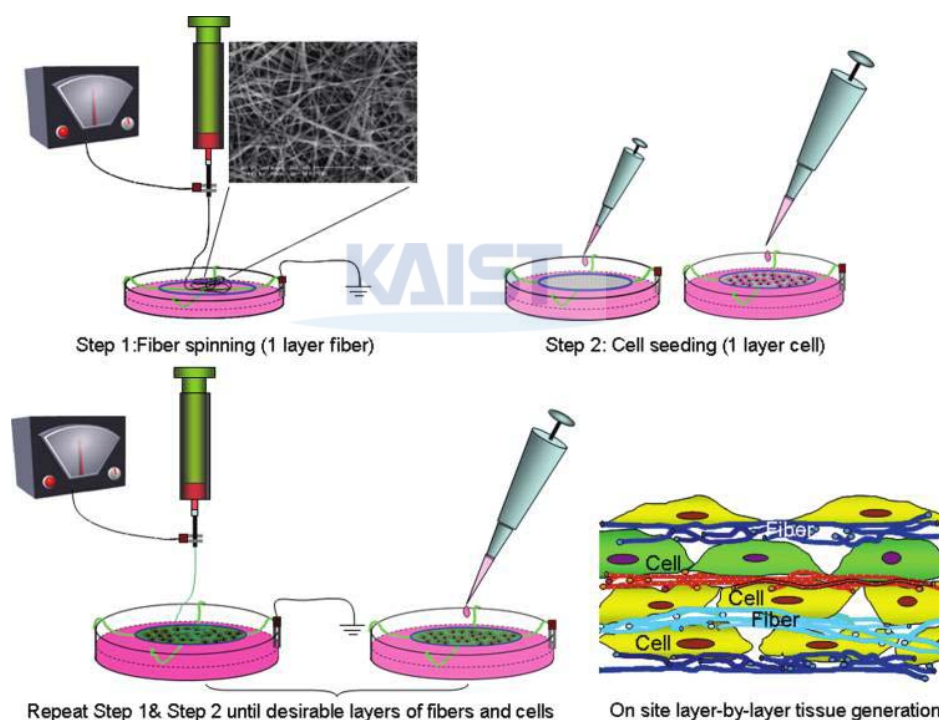


Figure 6-13. A schematic illustration of the L-b-L cell assembly while electrospinning [94].

The electrospun nanofibers were firstly deposited and then followed by cell seeding on top of the fibers. By repeating these steps, 3D cell/fiber integration was accomplished. Although this method solved the infiltration problem of electrospun nanofiber scaffold, some limitations still

---

remain. Since the cell seeding and nanofiber deposition are almost simultaneously performed in the same wet environment with culture medium, the residual solvent in the deposited fibers can cause cytotoxicity under variable process conditions. Furthermore, the versatile geometry or configuration such as fiber alignment cannot be expected due to the limited process condition.

In this research, a parallel L-b-L approach for 3D cell/fiber integration is introduced to enlarge the application of electrospun nanofiber structure.

#### *6.4.2 Fabrication of single-layer scaffold*

The main ideas in this approach are preparation of individual cell/fiber structures, and assembly of them in layer-by-layer manner. In the first step, the individual fibrous scaffolds were fabricated as shown in Figure 6-14. The aligned nanofiber arrays are transferred onto PDMS substrate repeatedly up to 40 transfers. Thereafter, the microfiber depositions by DPMD process are performed in order to pack the nanofiber mat into the individual scaffold. The deposited structures also provide the bonding surface instead of nanofiber mats in the following process for assembly between the scaffolds. The package using DPMD process allows to individualize the nanofibrous scaffolds. Because the nanofiber has an extremely thin thickness and high aspect ratio, it is difficult to handle the scaffold composed of only nanofibers. The presence of packaging frameworks at both ends of the nanofiber mat give easy handling. Furthermore, since the whole procedure of cell culture is carried out in wet environment of culture medium liquid, the aligned nanofiber scaffold wouldn't sustain its configuration if applied alone. Thus the frameworks are said to be necessary for the practical application of the electrospun nanofibrous tissue scaffold.



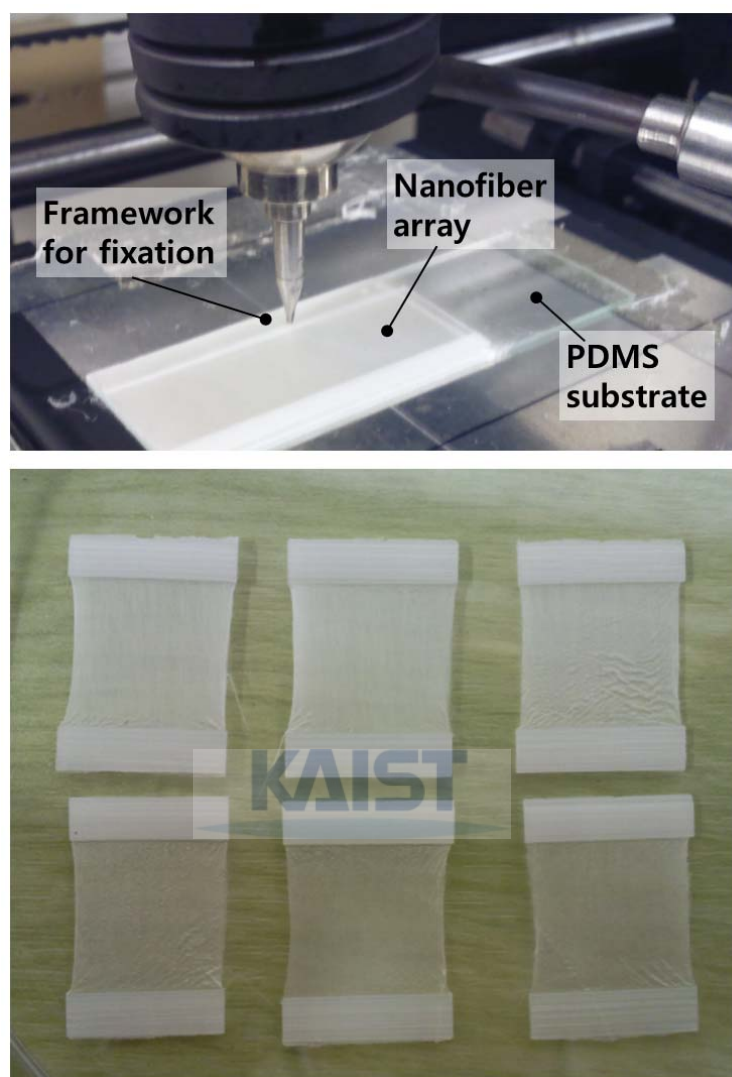


Figure 6-14. Package of the transferred nanofiber mats using DPMD process, and the resultant individual nanofiber scaffolds.

### *6.4.3 Cell seeding and layer-by-layer assembly*

For the cell seeding, C2C12 murine myoblasts were cultured in DMEM supplemented with 10% fetal bovine serum and 1% penicillin/streptomycin, grown in a humidified incubator at 37 °C, with 5% CO<sub>2</sub>. For differentiation induction, the growth medium was replaced with differentiation

---

media that consisted of DMEM, 5% horse serum and 1% penicillin/streptomycin after the grown cells are confluent.

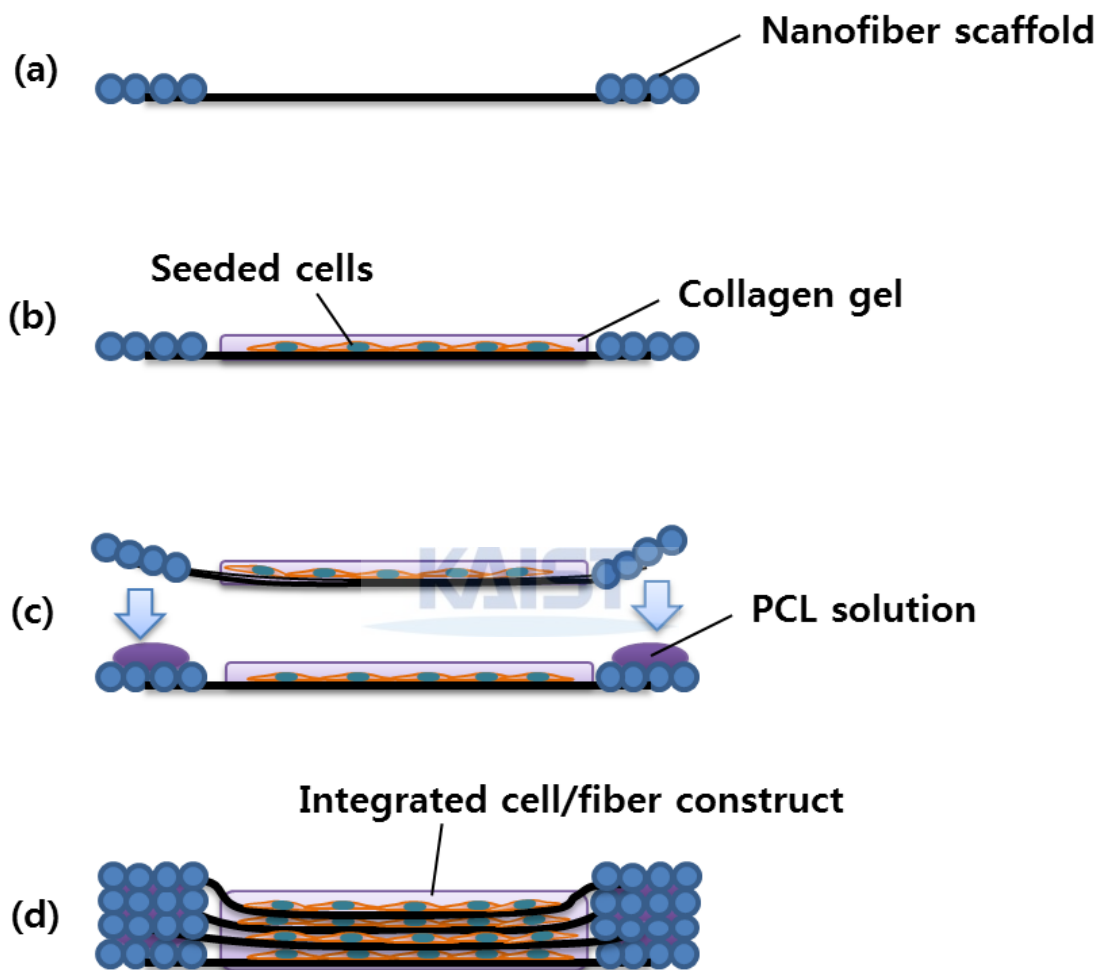


Figure 6-15. Schematics of cell seeding onto single-layer scaffold and layer-by-layer integration using collagen gel and polymer solution. (a) Preparation of unit scaffolds. (b) Cell seeding. (c) Assembly of cell/fiber construct using polymer solution and collagen gel. (d) Multi-layer integration.

The overall procedures for the layer-by-layer integration of cell/fiber structures are



illustrated in Figure 6-15. In the first step, the surface of the prepared nanofiber scaffold was coated with fibronectin for favorable cell adhesion, and the cells are seeded at 8000 cells/cm<sup>2</sup> onto each nanofiber scaffold. In five hours after the cell seeding, the cells adhere to the surface of the nanofiber scaffold as shown in Figure 6-16. The cells start to be elongated along the direction of fiber alignment. At this time, assembly between the cell-seeded scaffold is performed. As the scaffold is composed of the frameworks and the aligned nanofiber mat, the bonding processes for the assembly should be considered in different ways. One is use of polymer solution. Since the used solvent (methylene chloride) is highly volatile, the adhesion between polymer structures can be completed in a few minutes. Additionally, when the identical material is used as polymer in the solution (PCL in this case), high bonding strength between the structures is realized. In this experiment, the same PCL (MW 80,000) is dissolved in the methylene chloride at the concentration of 20 wt% for the bonding solution.

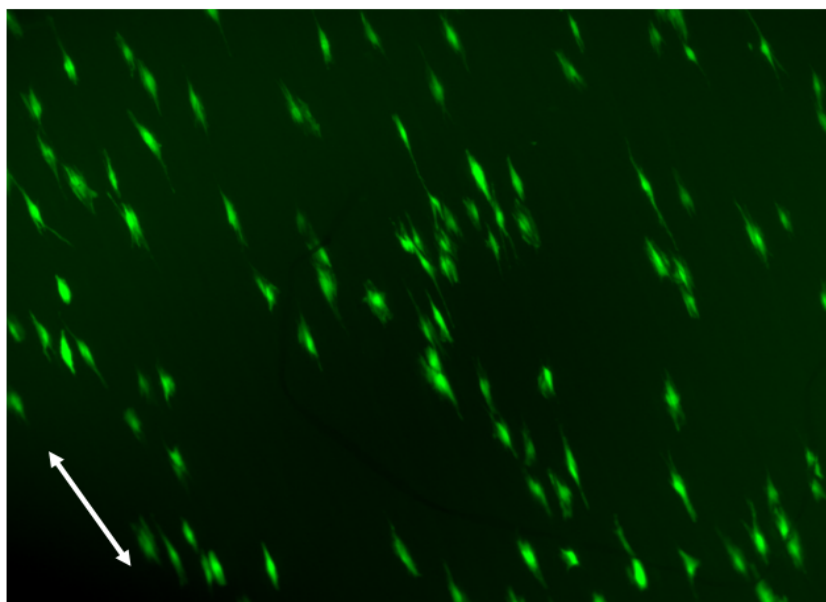


Figure 6-16. Cells adhered on surface of aligned nanofiber scaffold in five hours after cell seeding.

---

Unlike the macro-scale frameworks, the bonding solution should not be applied to nanofiber part of the scaffold because the nanofiber structure containing the cells is very subtle and easily damaged. Use of hydrogel material can be regarded as an alternative way for the bonding method. The fibronectin-coated surface of the nanofiber part of the scaffold is feasible for the application of hydrogel assembly. Although the assembly with the hydrogel is not much strong, the bonding between frameworks is strong and stable enough to support the overall integrated cell/fiber structures. In this research, collagen gel solution (3D Collagen Culture Kit, Millipore) of 100  $\mu$ l is dropped over the surface of nanofiber mat. The hydrophilic surface of nanofiber mat due to fibronectin coating allows well-spreading through the mat. the collagen solution on the scaffold is crosslinked in 37°C incubator with humidified environment. Figure 6-17 shows the application of collagen gel to the cell/fiber scaffolds.

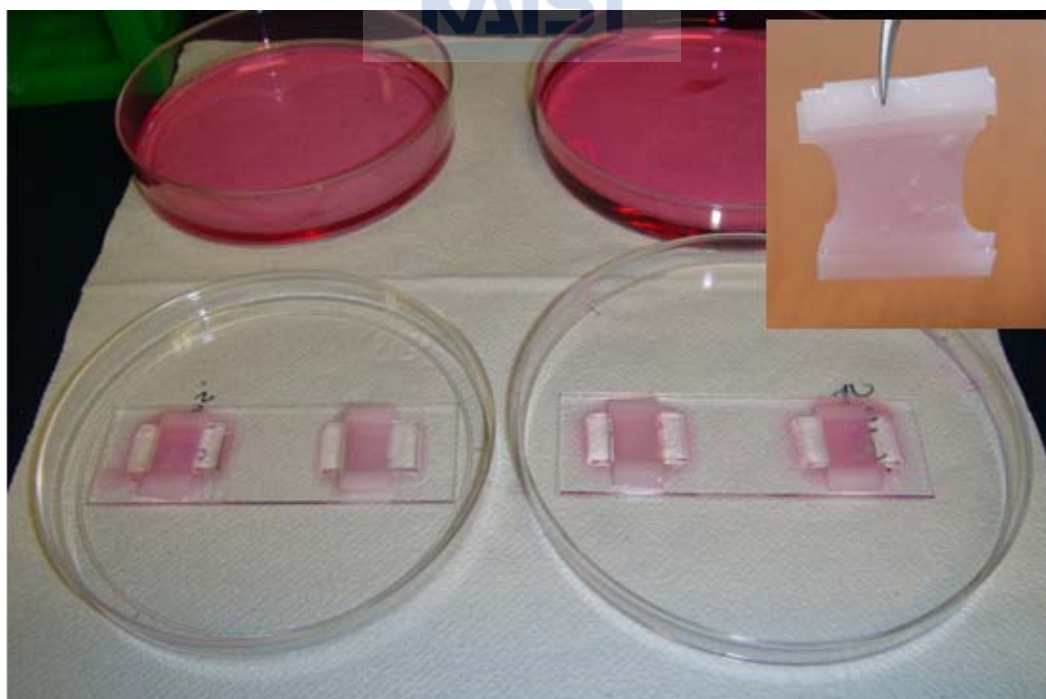


Figure 6-17. Application of collagen gel to the cell/fiber scaffolds.

#### 6.4.4 Multilayer tissue formation

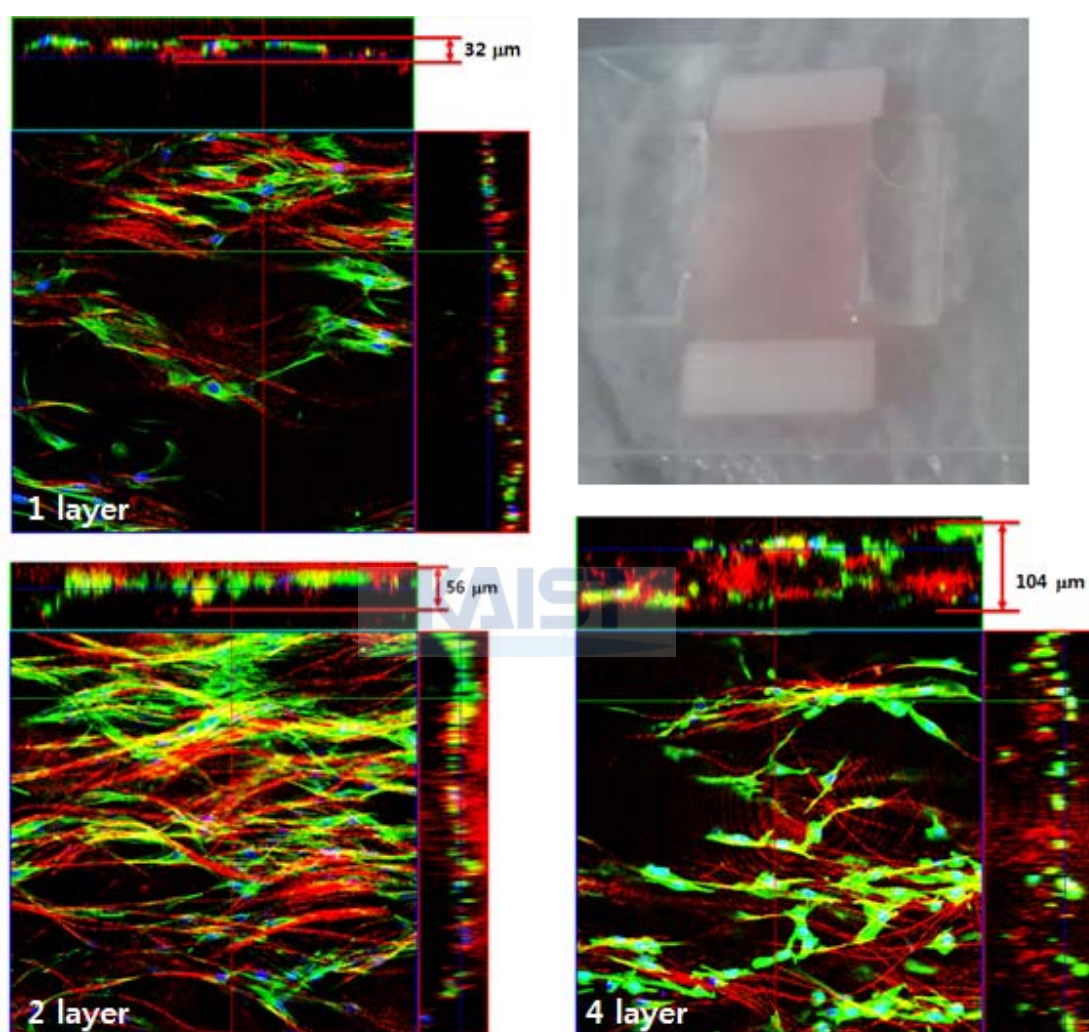


Figure 6-18. Confocal microscopic images of multilayer cell/fiber constructs of 1, 2, and 4 layer integration. Red, green, and blue are electrospun nanofiber, actin, and nucleus, respectively.

To form multilayer tissue construct with cells, a number of cell/fiber scaffolds with covered with collagen gel are prepared as mentioned above. After the collagen gelation and scaffold

---

assembly, two further 3 day incubation is carried out with 1, 2, and 4 layer constructs. The cell-cultured constructs were stained with DAPI (for staining of nuclei) and FITC (for staining of actin) and examined under confocal microscope. To visualize the electrospun nanofibers in the construct, rhodamine (Sigma Aldrich) was added and mixed with the electrospinning solution at the weight ratio of 100:1 (PCL:rhodamine). It was found that the thickness of cell/fiber construct tends to be proportional to the number of integrated layers as shown in Figure 6-18. And the cultured cells are often found within the scaffolds. It implies that the product by the suggested method doesn't have cell infiltration problem considered in the conventional electrospun scaffolds.

To visualize the cross-section and thickness dimension of the integrated cell/fiber construct, histological analyses were carried out. Two types of samples (Figure 6-19) were prepared in order to evaluate the effect of parallel cell culture and assembly on the cell distribution through the depth of the constructs. One is the 4 layer-integrated cell/fiber construct, which is assembled after the cell seeding on the individual scaffold (40 transfers). The other is 1 layer cell/fiber construct, which includes the same quantity (total 160 transfers) of the nanofibers as the former one. Although the two types of specimens have an almost identical quantity of the nanofibers, the average thickness of the 4 layer-integrated cell/fiber construct [Figure 6-19(a)] is larger than the 1 layer construct [Figure 6-19(b)]. Additionally, the integrated cell/fiber construct such as Figure 6-19(a) would solve the intrinsic problems caused by too small dimension of nanofibrous mat, including cell infiltration, nutrient perfusion, and oxygen supply.

The myoblasts grown on the nanofiber scaffolds are further cultured in differentiation media for up to 7 days. To examine the differentiation into myotube, fluorescence staining of myosin heavy chain (MHC) and F-actin were performed. As shown in Figure 6-20, the myoblasts formed multinucleated myofibers in the unidirection of nanofiber alignment.

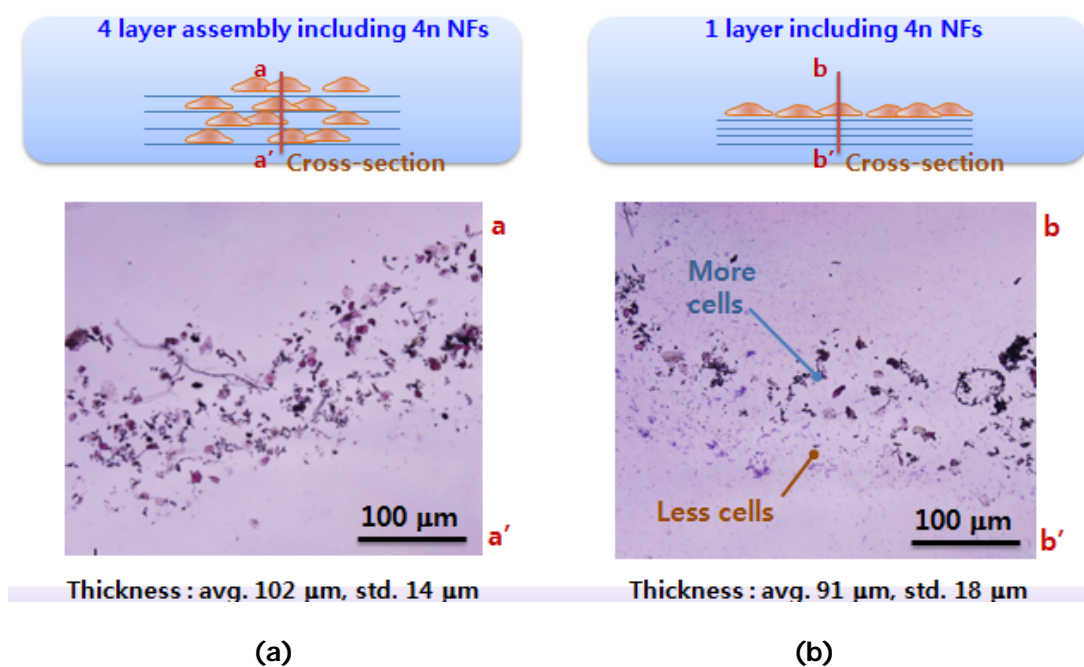


Figure 6-19. Light microscopic images of cross sections of multilayered cell/fiber constructs. (a) 4 layer integration of cell/fiber constructs and (b) single layer cell/fiber construct which have the same number of nanofibers as the case of (a).

In addition, Figure 6-19 shows the assembly of striated sarcomeres in myotube, which is the principal characteristic of contractile and functional myotubes. After all the observations, this method can realize not only the regulation of cell alignment and myotube assembly along the controlled features of the electrospun nanofiber scaffold but also generate 3D culture platforms for possible application of the engineering skeletal muscle at the tissue level.

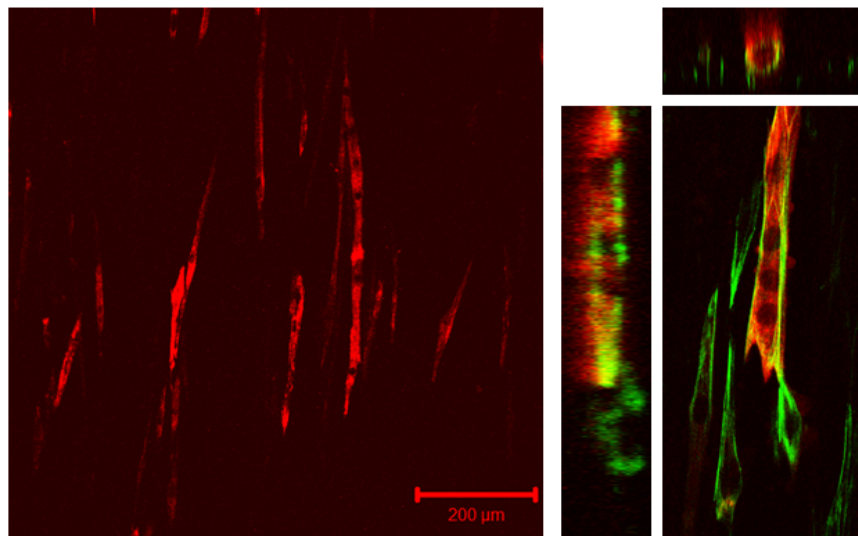


Figure 6-20. Myotube assembly on the aligned PCL nanofiber scaffold. Immunofluorescence staining of skeletal MHC was performed to show the myotubes at 7 days after the application of differentiation media.

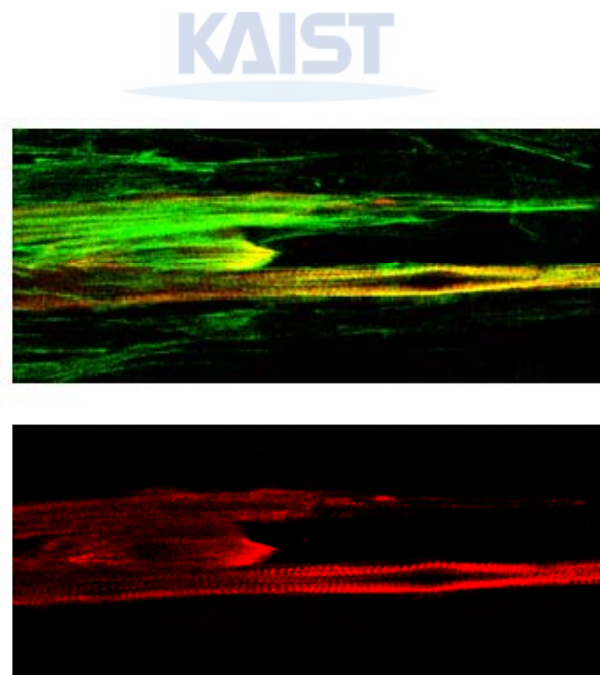


Figure 6-21. Immunofluorescence staining of anti-MHC showing a striated myotube on aligned nanofiber scaffold.





---

## CHAPTER VII

### CONCLUSIONS

In fabricating tissue engineered scaffold, both electrospinning and rapid prototyping (RP) methods have many advantages as effective technologies for each purposive approach. The electrospinning process provides a desirable characteristic in designing the scaffold mimicking the dimension and topology of natural extra-cellular matrix (ECM) fibers. With RP methods, the ECM mimicking structures are hardly realized due to their processing features of a relatively huge scale to a cell size. Compared to RP products, the electrospun fiber mesh has a particular small dimension of nano/micro scale generally in the similar range of ECM fibrils. On the other hand, the RP method has been regarded as the most promising technology to satisfy many of the general scaffold requirements. They can process a wide range of bio-applicable materials in a custom-made shape. The controllable features of inter- and intra- network of the 3D scaffold, such as pore size, shape, interconnectivity, and porosity, allows a favorable cell migration and nutrient perfusion compared to the scaffolds fabricated by the conventional methods.

However, both fabrication methods have some limitations when considered alone. Though electrospinning has demonstrated its ability to fabricate nanofiber scaffolds that closely mimic the native ECM structure, the fabrication and practical use of 3D macroscale scaffolds remain a challenge due to the small diameter of the electrospun nanofibers. Furthermore, the relatively small pores of the nanofibrous scaffolds may cause poor conditions of cell infiltration, waste removal, and nutrient perfusion.



As mentioned above, a biologically desirable characteristic that should be considered in designing and fabricating the engineered scaffolds is mimicking the ECM fiber structure. However, this still remains a challenge for rapid prototyping fabrication methods. It is required to satisfy both of the three-dimensional bulk property in overall geometry of the scaffold and the surface micro- and nano-porosity (or roughness) for the creation of ECM-like environment where cell activation can be enhanced. Currently, each of electrospinning and RP method deals with its own specific range of dimension. In other words, the electrospun fibers can hardly exceed micro- or macro- scale to form a 3D scaffold, and the current RP process has a difficulty to reach its product scale down to nano-scale to simulate ECM structure.

One possible solution to this problem from the scale difference is given by applying both processes of electrospinning and RP for scaffold fabrication. Basically, since the RP process employs a concept of layer-by-layer integration, electrospinning can be conducted between laminating procedures. As a result, a 3D dual-scale hierarchical construct containing nanofibers can be realized. In order to implement this new conceptive scaffold, the RP-based process, electrospinning for controlled configuration, and their combinatorial integration are developed and studied through this research. Some conclusions are derived as follows.

A 3D moving polymer melt extrusion system, namely Direct Polymer Melt Deposition (DPMD) process, has been proposed to fabricate 3D regular porous structure for application as tissue engineering scaffolds. There are some distinct features superior to those of conventional methods for scaffold fabrication, such as fabrication of three-dimensional microstructures, highly accurate fabrication, control of geometry and porosity, wide range of available materials. As well as use of the structure itself, the developed scaffold can be used in combination with other material processing techniques for various biomedical applications. The applicability of the process and the resultant scaffold was shown in the several aforementioned cases such as the

---

3D framework incorporated with nanofilament/hMSC spheroids, the 3D scaffold coated with hydroxyapatite/collagen nanocomposite, and the membrane filled with hydrogel. Additionally, when a viscous polymer solution is used as the process material instead of polymer melt, the smaller thickness of the deposited structure down to several ten micrometers can be realized. The resultant sheet-like structure can be applied to the post-surgical anti-adhesion membrane.

While the electrospun nanofibers with random configuration can be achieved under appropriate combination of the relevant process parameters, the fiber alignment technique allows more considerations. In this research, a high-performance of uniaxial alignment of electrospun nanofibers was realized by introducing an inclined gap into dual collectors that consisted of two conductive strips. Since the two strips that were configured horizontally and vertically had a height difference from the inclined gap, the electrospun nanofibers were sequentially suspended across the edges of strips in a well-aligned and regularly-distributed form. Some parameters, such as concentration of solution, applied voltage, and spinning distance were considered for the successful suspension and formation of the aligned electrospun fibers. The method could improve the properties of nanofiber alignment and allow easy transfer onto other solid substrates or devices. The alignment technique employed Polycaprolactone (PCL), which resulted in continuous and well-aligned nanofibers with diameters ranging from 500-700 nm. Furthermore, the repetitive transfer is suggested in order to achieve a higher density of aligned nanofiber arrays.

As mentioned above, the uniaxially electrospun nanofiber arrays were constructed with quantitatively controlled density. As a single transfer of the nanofibers collected from the inclined gap provided a well-aligned and regularly-distributed form, the developed nanofiber array could be applied to tissue scaffold by employing multiple transfers. The fiber density within a scaffold

could be controlled in proportion to the number of transfers. Diameters of the nanofibers in the scaffold were in a sub-micrometer range, which means that the fibers were appropriate to utilize as nano-topographic features. In regard to the contact guidance along the aligned direction of the nanofibers, favorable interactions between the fibroblasts and the developed scaffold, especially in a highly dense scaffold with the fiber spacing reduced down to less than the cell size, were revealed in observation of cell morphologies.

A nano- and micro- hybrid process incorporating direct polymer melt deposition (DPMD) and an electrospinning process was developed. It can be successfully applied to produce highly functionalized three-dimensional scaffolds with an open porous network, a controllable shape, and a biocompatible nanofibrous inner architecture. The main advantage of this hybrid scaffold over the other scaffolds is its three-dimensional characteristics simulated as a 3D fibrous extracellular environment. These technical results were achieved by inserting PCL/collagen biocomposite nanofiber matrices into the microfibrillar structures. Specifically, the RP method was used in conjunction with the functional electrospinning process in an effort to realize a 3D fashioned ECM-like structure. It was also clearly demonstrated that the presence of the inserted nanofiber matrices served to improve the properties of cell adhesion and proliferation. As well as the use of the typical random fiber mesh, the uniaxially aligned nanofiber array could be applied to the hybrid scaffold due to the transferability of the suggested collecting method. The developed integration skill using the dual process also facilitates the layer-by-layer approach for 3D tissue formation. As the individual nanofiber scaffolds are prepared by package using the DPMD process, multilayer assembly of cell/fiber scaffolds can be realized employing a polymer solution and a collagen gel as the bonding agents. This technique presented an enlarged application to 3D muscle tissue engineering.

---

In the future work, in order to further improve the dual-scale hierarchical scaffold, it is recommended that three major items are investigated. The first one is related to the customized scaffold design and realization for practical implantation according to CAD/CAM based anatomical data such as CT or MRI images. The second one is to test of other natural or synthetic biomaterials or combinations of these functional materials. As mentioned above, since the developed hybrid process can possibly utilize a wide range of materials, it can be expected that other novel scaffolds satisfying diverse purposes in the tissue engineering field can be produced using other functional biomaterials. And finally, further studies with other cell types utilizing more quantitative biochemical assays would be required to evaluate the feasibility of the developed scaffolds to tissue engineering applications.





---

## 要 約 文

### 전기방사 나노섬유를 포함한 3차원 인공지지체 개발 및 조직 재생으로의 적용

조직공학용 지지체 (Tissue engineering scaffold)는 그 표면 또는 내부에 세포가 파종되어 일정 시간 후 복합화된 상태에서 생체에 손상된 조직이나 장기에 적용하고 이를 복원, 재생, 또는 대체하기 위한 수단으로서 사용되는 구조물을 지칭한다. 조직공학용 지지체는 기본적으로 다공성 구조물로 구성되어 있고 각각의 공극이 서로 연결됨에 따라 영양분의 공급, 세포 사이에서의 대사물질 및 산소, 체액 등의 전달, 혈관신생 등이 원활히 이루어져야 한다. 또한 구성 고분자 재료의 생분해성으로 인하여 세포와 복합체를 이루어 체내에 이식된 후에 세포의 증식과 함께 분해되어 없어지게 된다. 최근 이러한 생분해성 고분자 지지체를 제작하는 방법으로 형상제어의 수단을 동반하여 CAD/CAM 기반의 쾌속조형 (Rapid Prototyping) 기술이 적용되고 있다.

본 연구에서는 압축공기의 적용을 통해 생체 고분자를 직접 용융 분사하여 3차원 구조물을 제작하는 쾌속조형 기반의 3차원 조형 공정을 개발하였다. 본 공정을 통하여 제작된 3차원 지지체는 기능성 생체 활성물질의 표면 개질을 통하여 기능성 향상을 확인하였고, 적층시 공극사이에 앞서 개발된 구형 세포 집합체를 적용함으로써 조직재생의 응용을 시도하였다. 또한 본 공정에서의 재료를 용융 고분자가 아닌 휘발성 용매에 녹인 고분자 용액으로 대체함으로써 얇은 막형태의 구조를 제작하였다. 이는 하이드로젤 개질을 통하여 수술후 유착방지막의 활용을 검증 하였다.

---

또한 개발된 공정이 적층 방식인 점을 활용하여 적층면 사이에 전기방사 나노섬유를 형성함으로써 3차원 조직공학용 지지체로서의 기능성을 극대화하였다. 일반적으로 쾌속조형을 통한 다공성 지지체가 갖는 매끄러운 표면과 세포 크기에 비해 상대적으로 큰 스케일의 한계점을 이러한 나노섬유 적용을 통해 보완하였다. 다른 측면으로 나노/마이크로 토포그래피에 의해 그 기능성이 여러 방향으로 검증된 나노섬유를 3차원 구조화하였다는 점에서 중요한 의미를 갖는다.

3차원 구조에 내재하는 전기방사 나노섬유 메쉬의 경우 기본적인 형태로서 랜덤하게 쌓이는 구조를 쾌속조형 공정과 교대로 적층하여 구성해볼 수 있으며 이를 연골세포 배양을 통하여 기능성을 검증하였다. 한편 체내의 조직 중에는 골격근, 인대, 건과 같이 조직내 세포의 형태가 일정한 방향으로 배향되어 있는 조직들이 있다. 이러한 조직에 적용되기 위한 지지체 역시 세포의 가이드 역할이 될 수 있도록 형태가 일정한 방향으로 배향되어 있는 것이 바람직하다.

본 연구에서는 넓은 면적에 활용 될 수 있는 전사 가능한 전기방사 나노섬유 배향 방법을 개발하여 적용하였다. 개발된 방법을 통한 나노섬유 매트와 경우 나노섬유의 양, 즉 밀도가 정량적으로 제어 가능하며 다른 구조 표면에 적용할 수 있는 장점이 있다. 정량적으로 밀도를 다르게 구성하여 섬유아세포의 배향효과를 통해 개발된 정렬방법의 이점을 검증하였다. 이를 앞서 설명된 바와 같이 마이크로 구조와 교대적층을 통해 3차원 구조화 하여 간엽줄기세포 배양을 통해 응용성을 검토하였다. 한편 마이크로 구조를 나노섬유의 틀로서 형성하여 패키징화 함으로써 세포와 나노섬유 혼합 구조를 구현하였다. 개별화 되어있는 나노섬유 지지체에 근아세포를 파종하고 이를 일정시간 배양 후 콜라겐 젤 및 고분자 용액으로 적층함으로써 효율적인 조직 재생방법을 제안하였다.

---

## REFERENCES

1. Brittberg, M., et al., *Treatment of Deep Cartilage Defects in the Knee with Autologous Chondrocyte Transplantation*. New England Journal of Medicine, 1994. **331**(14): p. 889-895.
2. Peterson, L., et al., *Two- to 9-year outcome after autologous chondrocyte transplantation of the knee*. Clinical Orthopaedics and Related Research, 2000(374): p. 212-234.
3. F. Ungaro, M.B., L. Indolfi, G. De Rosa, M.I. La Rotonda, F. Quaglia, P. Netti, *Bioactivated polymer scaffolds for tissue engineering*. Topics in Tissue Engineering, 2005. **Volume 2**(Chapter 5 biomaterials): p. 1-38.
4. Pachence, J.M., *Collagen-based devices for soft tissue repair*. Journal of Biomedical Materials Research, 1996. **33**(1): p. 35-40.
5. Leong, K.F., C.M. Cheah, and C.K. Chua, *Solid freeform fabrication of three-dimensional scaffolds for engineering replacement tissues and organs*. Biomaterials, 2003. **24**(13): p. 2363-2378.
6. Mikos, A.G., et al., *Preparation of Poly(Glycolic Acid) Bonded Fiber Structures for Cell Attachment and Transplantation*. Journal of Biomedical Materials Research, 1993. **27**(2): p. 183-189.
7. Mooney, D.T., et al., *Stabilized polyglycolic acid fibre based tubes for tissue engineering*. Biomaterials, 1996. **17**(2): p. 115-124.
8. Mikos, A.G., et al., *Preparation and Characterization of Poly(L-Lactic Acid) Foams*. Polymer, 1994. **35**(5): p. 1068-1077.
9. Mooney, D.J., et al., *Novel approach to fabricate porous sponges of poly(D,L-lactic-co-glycolic acid) without the use of organic solvents*. Biomaterials, 1996. **17**(14): p. 1417-1422.
10. Whang, K., et al., *A Novel Method to Fabricate Bioabsorbable Scaffolds*. Polymer,



## REFERENCES

---

1995. **36**(4): p. 837-842.
11. van Tienen, T.G., et al., *Tissue ingrowth polymers and degradation of two biodegradable porous with different porosities and pore sizes*. *Biomaterials*, 2002. **23**(8): p. 1731-1738.
  12. Zeltinger, J., et al., *Effect of pore size and void fraction on cellular adhesion, proliferation, and matrix deposition*. *Tissue Engineering*, 2001. **7**(5): p. 557-572.
  13. Hollister, S.J., *Porous scaffold design for tissue engineering*. *Nature Materials*, 2005. **4**(7): p. 518-524.
  14. Hollister, S.J., et al., *An image-based approach for designing and manufacturing craniofacial scaffolds*. *International Journal of Oral and Maxillofacial Surgery*, 2000. **29**(1): p. 67-71.
  15. Wettergreen, M.A., et al., *Computer-aided tissue engineering of a human vertebral body*. *Annals of Biomedical Engineering*, 2005. **33**(10): p. 1333-1343.
  16. Harris, R.A., et al., *Part shrinkage anomalies from stereolithography injection mould tooling*. *International Journal of Machine Tools & Manufacture*, 2003. **43**(9): p. 879-887.
  17. Cooke, M.N., et al., *Use of stereolithography to manufacture critical-sized 3D biodegradable scaffolds for bone ingrowth*. *Journal of Biomedical Materials Research Part B-Applied Biomaterials*, 2003. **64B**(2): p. 65-69.
  18. Lee, K.W., et al., *Poly(propylene fumarate) bone tissue engineering scaffold fabrication using stereolithography: Effects of resin formulations and laser parameters*. *Biomacromolecules*, 2007. **8**(4): p. 1077-1084.
  19. Arcaute, K., B.K. Mann, and R.B. Wicker, *Stereolithography of three-dimensional bioactive poly(ethylene glycol) constructs with encapsulated cells*. *Annals of Biomedical Engineering*, 2006. **34**(9): p. 1429-1441.
  20. Dhariwala, B., E. Hunt, and T. Boland, *Rapid prototyping of tissue-engineering constructs, using photopolymerizable hydrogels and stereolithography*. *Tissue Engineering*, 2004. **10**(9-10): p. 1316-1322.
  21. Maruo, S. and K. Ikuta, *Submicron stereolithography for the production of freely*

- 
- movable mechanisms by using single-photon polymerization. Sensors and Actuators a-Physical*, 2002. **100**(1): p. 70-76.
22. Sun, C. and X. Zhang, *The influences of the material properties on ceramic micro-stereolithography. Sensors and Actuators a-Physical*, 2002. **101**(3): p. 364-370.
  23. Hoque, M.E., et al., *Fabrication using a rapid prototyping system and in vitro characterization of PEG-PCL-PLA scaffolds for tissue engineering. Journal of Biomaterials Science-Polymer Edition*, 2005. **16**(12): p. 1595-1610.
  24. Hutmacher, D.W., et al., *Mechanical properties and cell cultural response of polycaprolactone scaffolds designed and fabricated via fused deposition modeling. Journal of Biomedical Materials Research*, 2001. **55**(2): p. 203-216.
  25. Sun, J.J., et al., *Fabrication of hydroxyapatite-poly(epsilon-caprolactone) scaffolds by a combination of the extrusion and bi-axial lamination processes. Journal of Materials Science-Materials in Medicine*, 2007. **18**(6): p. 1017-1023.
  26. Pfister, A., et al., *Biofunctional rapid prototyping for tissue-engineering applications: 3D bioplotting versus 3D printing. Journal of Polymer Science Part a-Polymer Chemistry*, 2004. **42**(3): p. 624-638.
  27. Giordano, R.A., et al., *Mechanical properties of dense polylactic acid structures fabricated by three dimensional printing. Journal of Biomaterials Science-Polymer Edition*, 1996. **8**(1): p. 63-75.
  28. Roy, T.D., et al., *Performance of hydroxyapatite bone repair scaffolds created via three-dimensional fabrication techniques. Journal of Biomedical Materials Research Part A*, 2003. **67A**(4): p. 1228-1237.
  29. Tan, K.H., et al., *Selective laser sintering of biocompatible polymers for applications in tissue engineering. Bio-Medical Materials and Engineering*, 2005. **15**(1-2): p. 113-124.
  30. Williams, J.M., et al., *Bone tissue engineering using polycaprolactone scaffolds fabricated via selective laser sintering. Biomaterials*, 2005. **26**(23): p. 4817-4827.
  31. Wiria, F.E., et al., *Poly-epsilon-caprolactone/hydroxyapatite for tissue engineering scaffold fabrication via selective laser sintering. Acta Biomaterialia*, 2007. **3**(1): p. 1-

## REFERENCES

---

- 12.
32. <http://endometriosis-bible.com/?hop=amyhart>.
33. Huang, L., et al., *Generation of synthetic elastin-mimetic small diameter fibers and fiber networks*. Macromolecules, 2000. **33**(8): p. 2989-2997.
34. Bissell, M.J., H.G. Hall, and G. Parry, *How Does the Extracellular-Matrix Direct Gene-Expression*. Journal of Theoretical Biology, 1982. **99**(1): p. 31-68.
35. Zhang, Y.Z., et al., *Characterization of the surface biocompatibility of the electrospun PCL-collagen nanofibers using fibroblasts*. Biomacromolecules, 2005. **6**(5): p. 2583-2589.
36. Ashammakhi, N., et al., *Tissue engineering: A new take-off using nanofiber-based scaffolds*. Journal of Craniofacial Surgery, 2007. **18**(1): p. 3-17.
37. Shields, K.J., et al., *Mechanical properties and cellular proliferation of electrospun collagen type II*. Tissue Engineering, 2004. **10**(9-10): p. 1510-1517.
38. Min, B.M., et al., *Electrospinning of silk fibroin nanofibers and its effect on the adhesion and spreading of normal human keratinocytes and fibroblasts in vitro*. Biomaterials, 2004. **25**(7-8): p. 1289-1297.
39. Riboldi, S.A., et al., *Electrospun degradable polyesterurethane membranes: potential scaffolds for skeletal muscle tissue engineering*. Biomaterials, 2005. **26**(22): p. 4606-4615.
40. Venugopal, J., et al., *In vitro study of smooth muscle cells on polycaprolactone and collagen nanofibrous matrices*. Cell Biology International, 2005. **29**(10): p. 861-867.
41. Kim, K., et al., *Control of degradation rate and hydrophilicity in electrospun non-woven poly(D,L-lactide) nanofiber scaffolds for biomedical applications*. Biomaterials, 2003. **24**(27): p. 4977-4985.
42. Choi, J.S., et al., *The influence of electrospun aligned poly(epsilon-caprolactone)/collagen nanofiber meshes on the formation of self-aligned skeletal muscle myotubes*. Biomaterials, 2008. **29**(19): p. 2899-2906.
43. Xu, C.Y., et al., *Aligned biodegradable nanotibrous structure: a potential scaffold for blood vessel engineering*. Biomaterials, 2004. **25**(5): p. 877-886.

- 
44. Yang, F., et al., *Electrospinning of nano/micro scale poly(L-lactic acid) aligned fibers and their potential in neural tissue engineering*. Biomaterials, 2005. **26**(15): p. 2603-2610.
  45. Lee, C.H., et al., *Nanofiber alignment and direction of mechanical strain affect the ECM production of human ACL fibroblast*. Biomaterials, 2005. **26**(11): p. 1261-1270.
  46. Boland, E.D., et al., *Electrospinning of tissue engineering scaffolds*. Abstracts of Papers of the American Chemical Society, 2001. **222**: p. U344-U344.
  47. Matthews, J.A., et al., *Electrospinning of collagen nanofibers*. Biomacromolecules, 2002. **3**(2): p. 232-238.
  48. Katta, P., et al., *Continuous electrospinning of aligned polymer nanofibers onto a wire drum collector*. Nano Letters, 2004. **4**(11): p. 2215-2218.
  49. Theron, A., E. Zussman, and A.L. Yarin, *Electrostatic field-assisted alignment of electrospun nanofibres*. Nanotechnology, 2001. **12**(3): p. 384-390.
  50. Li, D., Y.L. Wang, and Y.N. Xia, *Electrospinning of polymeric and ceramic nanofibers as uniaxially aligned arrays*. Nano Letters, 2003. **3**(8): p. 1167-1171.
  51. Li, D., Y.L. Wang, and Y.N. Xia, *Electrospinning nanofibers as uniaxially aligned arrays and layer-by-layer stacked films*. Advanced Materials, 2004. **16**(4): p. 361-366.
  52. Kessick, R., J. Fenn, and G. Tepper, *The use of AC potentials in electrospraying and electrospinning processes*. Polymer, 2004. **45**(9): p. 2981-2984.
  53. Thomson, R.C., et al., *Biodegradable polymer scaffolds to regenerate organs*. Biopolymers, 1995. **122**: p. 245-274.
  54. Suggs, L. J., M.A.G., ed. *Synthetic biodegradable polymers for medical applications*. Physical properties of polymers handbook. 1996, American Institute of Physics. 615-624.
  55. Vozzi, G., et al., *Microsyringe-based deposition of two-dimensional and three-dimensional polymer scaffolds with a well-defined geometry for application to tissue engineering*. Tissue Engineering, 2002. **8**(6): p. 1089-1098.
  56. Kim, T.G., et al., *Hierarchically Assembled Mesenchymal Stem Cell Spheroids Using Biomimicking Nanofilaments and Microstructured Scaffolds for Vascularized Adipose*

## REFERENCES

---

- Tissue Engineering*. Advanced Functional Materials, 2010. **20**(14): p. 2303-2309.
57. Seifer, D.B., M.P. Diamond, and A.H. Decherney, *An Appraisal of Barrier Agents in the Reduction of Adhesion Formation Following Surgery*. Journal of Gynecologic Surgery, 1990. **6**(1): p. 3-10.
58. Reneker, D.H. and I. Chun, *Nanometre diameter fibres of polymer, produced by electrospinning*. Nanotechnology, 1996. **7**(3): p. 216-223.
59. Reneker, D.H., et al., *Bending instability of electrically charged liquid jets of polymer solutions in electrospinning*. Journal of Applied Physics, 2000. **87**(9): p. 4531-4547.
60. Yarin, A.L., S. Koombhongse, and D.H. Reneker, *Bending instability in electrospinning of nanofibers*. Journal of Applied Physics, 2001. **89**(5): p. 3018-3026.
61. Li, D., et al., *Collecting electrospun nanofibers with patterned electrodes*. Nano Letters, 2005. **5**(5): p. 913-916.
62. Liu, L.H. and Y.A. Dzenis, *Analysis of the effects of the residual charge and gap size on electrospun nanofiber alignment in a gap method*. Nanotechnology, 2008. **19**: 355307.
63. Ramakrishna S, F.K., Teo WE, Lim TC, Ma Z, *An Introduction to Electrospinning and Nanofibers*. Danvers, MA: World Scientific, 2005.
64. Lee, K.H., et al., *Characterization of nano-structured poly(epsilon-caprolactone) nonwoven mats via electrospinning*. Polymer, 2003. **44**(4): p. 1287-1294.
65. Taylor, S.G., *Disintegration of Water Drops in an Electric Field*. Proceedings of the Royal Society of London. Series A, Mathematical and Physical Sciences, 1964. **280**(1382): p. 383-397.
66. Venugopal, J., Y.Z. Zhang, and S. Ramakrishna, *Fabrication of modified and functionalized polycaprolactone nanofibre scaffolds for vascular tissue engineering*. Nanotechnology, 2005. **16**(10): p. 2138-2142.
67. Murugan, R. and S. Ramakrishna, *Nano-featured scaffolds for tissue engineering: A review of spinning methodologies*. Tissue Engineering, 2006. **12**(3): p. 435-447.
68. Zussman, E., A. Theron, and A.L. Yarin, *Formation of nanofiber crossbars in electrospinning*. Applied Physics Letters, 2003. **82**(6): p. 973-975.

- 
69. Teo, W.E., et al., *Porous tubular structures with controlled fibre orientation using a modified electrospinning method*. Nanotechnology, 2005. **16**(6): p. 918-924.
70. Yang, D.Y., et al., *Fabrication of aligned fibrous arrays by magnetic electrospinning*. Advanced Materials, 2007. **19**(21): p. 3702-+.
71. Pan, H., et al., *Continuous aligned polymer fibers produced by a modified electrospinning method*. Polymer, 2006. **47**(14): p. 4901-4904.
72. Deitzel, J.M., et al., *Controlled deposition of electrospun poly(ethylene oxide) fibers*. Polymer, 2001. **42**(19): p. 8163-8170.
73. Chen, C.S., et al., *Geometric control of cell life and death*. Science, 1997. **276**(5317): p. 1425-1428.
74. Flemming, R.G., et al., *Effects of synthetic micro- and nano-structured surfaces on cell behavior*. Biomaterials, 1999. **20**(6): p. 573-588.
75. Lim, J.Y. and H.J. Donahue, *Cell sensing and response to micro- and nanostructured surfaces produced by chemical and topographic patterning*. Tissue Engineering, 2007. **13**(8): p. 1879-1891.
76. Lu, Y. and S.C. Chen, *Micro and nano-fabrication of biodegradable polymers for drug delivery*. Advanced Drug Delivery Reviews, 2004. **56**(11): p. 1621-1633.
77. Mironov, V., V. Kasyanov, and R.R. Markwald, *Nanotechnology in vascular tissue engineering: from nanoscaffolding towards rapid vessel biofabrication*. Trends in Biotechnology, 2008. **26**(6): p. 338-344.
78. Chew, S.Y., et al., *The role of electrospinning in the emerging field of nanomedicine*. Current Pharmaceutical Design, 2006. **12**(36): p. 4751-4770.
79. Kumbar, S.G., et al., *Electrospun nanofiber scaffolds: engineering soft tissues*. Biomedical Materials, 2008. **3**(3): p. -.
80. Li, W.J., et al., *Electrospun nanofibrous structure: A novel scaffold for tissue engineering*. Journal of Biomedical Materials Research, 2002. **60**(4): p. 613-621.
81. Nair, L.S., S. Bhattacharyya, and C.T. Laurencin, *Development of novel tissue engineering scaffolds via electrospinning*. Expert Opinion on Biological Therapy, 2004. **4**(5): p. 659-668.

## REFERENCES

---

82. Xu, C.Y., et al., *Electrospun nanofiber fabrication as synthetic extracellular matrix and its potential for vascular tissue engineering*. Tissue Engineering, 2004. **10**(7-8): p. 1160-1168.
83. Clark, P., P. Connolly, and G.R. Moores, *Cell Guidance by Micropatterned Adhesiveness In vitro*. Journal of Cell Science, 1992. **103**: p. 287-292.
84. Corey, J.M., et al., *The design of electrospun PLLA nanofiber scaffolds compatible with serum-free growth of primary motor and sensory neurons*. Acta Biomaterialia, 2008. **4**(4): p. 863-875.
85. Dunn, G.A. and A.F. Brown, *Alignment of Fibroblasts on Grooved Surfaces Described by a Simple Geometric Transformation*. Journal of Cell Science, 1986. **83**: p. 313-340.
86. Mills, C.A., et al., *Micro- and nanostructuring of poly(ethylene-2,6-naphthalate) surfaces, for biomedical applications, using polymer replication techniques*. Nanotechnology, 2005. **16**(4): p. 369-375.
87. Sutherland, J., M. Denyer, and S. Britland, *Contact guidance in human dermal fibroblasts is modulated by population pressure*. Journal of Anatomy, 2005. **206**(6): p. 581-587.
88. Teixeira, A.I., et al., *Epithelial contact guidance on well-defined micro- and nanostructured substrates*. Journal of Cell Science, 2003. **116**(10): p. 1881-1892.
89. Liu, L., *Studies on deposition and alignment of electrospun nanofiber assemblies*. University of Nebraska-Lincoln, 2006. Dissertation for degree of doctor of philosophy.
90. Khang, G., et al., *Interaction of fibroblast cells onto fibers with different diameter*. Korea Polymer Journal, 1999. **7**(2): p. 102-107.
91. Bashur, C.A., L.A. Dahlgren, and A.S. Goldstein, *Effect of fiber diameter and orientation on fibroblast morphology and proliferation on electrospun poly(D,L-lactic-co-glycolic acid) meshes*. Biomaterials, 2006. **27**(33): p. 5681-5688.
92. den Braber, E.T., et al., *Scanning electron microscopic, transmission electron microscopic, and confocal laser scanning microscopic observation of fibroblasts cultured on microgrooved surfaces of bulk titanium substrata*. Journal of Biomedical Materials Research, 1998. **40**(3): p. 425-433.

- 
93. Wool, R.P., B.L. Yuan, and O.J. McGarel, *Welding of Polymer Interfaces*. Polymer Engineering and Science, 1989. **29**(19): p. 1340-1367.
94. Yang, X.C., J.D. Shah, and H.J. Wang, *Nanofiber Enabled Layer-by-Layer Approach Toward Three-Dimensional Tissue Formation*. Tissue Engineering Part A, 2009. **15**(4): p. 945-956.

